ABSTRACT

(Physics — Particle)

SEARCH FOR NEW PARTICLES DECAYING TO DIJETS IN $P\bar{P}$ COLLISIONS AT $\sqrt{S} = 1.8$ TEV

by

Chao Wei

Department of Physics
Duke University

Date: 1/1/96

Approved:

Lloyd R. Fortney, Supervisor

Alfred T. Goshaw

Alfred M. Lee

Roxanne P. Springer

Daniel J. Gauthier

An abstract of a dissertation submitted in partial fulfillment of the requirements for the degree of Doctor of Philosophy in the Department of Physics in the Graduate School of Duke University

1996

Abstract

We have used 106 pb^{-1} of data collected in $p\bar{p}$ collision at $\sqrt{s} = 1.8$ TeV by the Collider Detector at Fermilab (CDF) to measure dijet invariant mass distribution and jet angular distributions using four single jet triggers. The dijet invariant mass spectrum extends from 180 to 1035 GeV/c^2. The mass distribution is significantly above a QCD and CDF detector simulation at high mass. We present limits on the hypothesis that the effect is new physics with an isotropic angular distribution. Fitting the data to a smooth background function plus a mass resonance we obtain a 95% confidence level upper limit on the cross section for new particles as a function of mass. We compare this upper limit to the cross section for axigluons, excited quarks, technirhos, new gauge bosons (W' and Z') and E_6 diquarks. This search excludes at 95% confidence level a model of axigluons for $200 < M_A < 1060$ GeV/c^2, a model of excited quarks for $200 < M^* < 560$ and $620 < M^* < 760$ GeV/c^2, a model of technirhos for $260 < M_{\rho_T} < 490$ GeV/c^2, a model of new gauge boson W' for $300 < M_{W'} < 430$ GeV/c^2, and a model of E_6 diquarks for $280 < M_{E6} < 420$ GeV/c^2. The jet angular distributions agree with next to leading order QCD predictions in all dijet invariant mass regions. The data excluded at 95% confidence level a model of quark substructure in which all quarks are composite and the excluded regions are $\Lambda_+ \leq 1.8TeV$ and $\Lambda_- \leq 1.6TeV$.

Acknowledgements

First of all, I would like to thank my advisor Prof. Lloyd R. Fortney for his guidance and support over the past four years. I must also acknowledge his careful reading and correcting the manuscripts of this thesis.

I wish to thank all my colleagues at CDF. This thesis is only possible because of their great work. In particular, I would like to thank Robert Harris for initializing this analysis, and giving helpful suggestions and advice whenever needed.

I would also like to thank all my colleagues in the high energy physics group at Duke. Thanks goes to Prof. Al Goshaw, who is always willing to hear the current state of my analysis, to Bill Robertson and Prof. Al Lee for giving me a lot help, and to Pat Hoyt for taking care of lots of things. It has been fun to be around my fellow graduate students. My gratitude goes to Susi Hauger, Jay Dittmann, Dan Cronin-Hennessy and Steve Lautenschlager for their help and friendship.

Most of all, I want to thank my wife, Yuping for her love and support. In many ways, this accomplishment is as much hers as it is mine. I would also like to thank my daughter, YiYi for being a wonderful kid.

Finally, I would like to thank my parents for their love and encouragement.

Contents

Abstract iv

Acknowledgements vi

List of Figures xi

List of Tables xiv

1 Theory 1

1.1 Introduction to Standard Model 1

1.2 Quantum Chromodynamics and Jet Production 4

1.3 Beyond the Standard Model 11

1.3.1 Axigluons 12

1.3.2 Excited Quarks 15

1.3.3 Technirhos 17

1.3.4 New Gauge Bosons 20

1.3.5 E_6 Diquarks 22

2 Experimental Apparatus 25

2.1 The Tevatron Collider 25

2.2 The Collider Detector at Fermilab (CDF) 27

2.2.1 The Tracking system 30

2.2.2 The Calorimetry 34

2.3 Beam-Beam Counters (BBC) 39

3 Jets Measurement at CDF **41**

3.1 CDF Jet triggers 43

3.2 Jet Clustering 47

3.3 Jet energy correction 49

3.3.1 Calorimetery response determination 50

3.3.2 Underlying Event correction 54

3.3.3 Out of cone correction 55

4 Measurement **57**

4.1 Data Set 57

4.2 Dijet Event Selection 57

4.3 Trigger Efficiency 60

4.3.1 Trig Efficiency vs. χ 62

4.4 Luminosity 62

5 Search for New Particles Decaying into Dijets **65**

5.1 The Measured Dijet Mass Distribution and Background Fit . . 66

5.2 QCD background simulations 68

5.2.1 Event Generation 68

5.2.2 QFL Detector Simulation 68

5.2.3 Comparison of Data and QCD Simulation 69

5.3 Dijet Mass resonance line shape from New Particle Production 71

5.4 Search for New Particles 72

5.4.1 Significance of Observed fluctuations 73

5.4.2 Search unusual features 73

5.5 Determination of the New Particle Production Limits 77

5.6 Fit to background + new particle signal 80

5.7 Systematic Uncertainties 81

5.7.1 Procedure for Including Systematics 81

5.7.2 Estimates of Systematic Uncertainties 82

5.8 Limits on New Particle Production 87

5.8.1 Limits on New Particle Productions without Systematics 87

5.8.2 Effect of Systematic Uncertainties on the Limit 90

6 Dijet Angular Distribution Analysis 94

6.1 Angular Variables 95

6.2 Dijet Angular Distribution Measurement 96

6.3 Acceptance and Systematics 98

6.3.1 Fast CDF Jet Simulation 98

6.3.2 Jet Energy Resolution 100

6.3.3 Comparison of Data and Fast Jet Simulation 104

6.3.4 Acceptance 109

6.3.5 Systematic Uncertainty on Acceptance 115

6.4 Corrected Angular Distribution and QCD 116

6.4.1 Cross Check using Central Only 122

6.5 Dijet Angular Distribution for Compositeness 123

6.5.1 Quark Compositeness 123

6.5.2 Comparison of Dijet angular ratio between data and Quark Compositeness 127

6.5.3 Limits on the Energy Scale of Quark Compositeness . . . 127

7 Conclusions **131**

A The CDF Author List **133**

Bibliography **138**

Biography **143**

List of Figures

1.1 High energy hadron-hadron collision in the parton model 6

1.2 Lowest Order Feynman graph for $2 \rightarrow 2$ processes 8

1.3 Quark-antiquark annihilation through axigluon exchange 14

1.4 Feynman graphs for technirho (ρ_T) production and decay into dijet channel 18

2.1 Schematic of the Fermilab accelerator complex 26

2.2 A side view cross section of the CDF detector 28

2.3 Isometric view of the SVX 31

2.4 Schematic view of one SVX ladder 32

2.5 Endplate of the Central Tracking Chamber 33

2.6 View of one wedge of the central calorimeter 35

2.7 A schematic diagram of a CES chamber 37

3.1 A typical dijet event 42

3.2 Missing E_T projection function MPF vs. η_D 52

3.3 The dielectron mass distribution for Run 0, Run 1A and Run 1B 55

4.1 Jet Trigger Efficiency vs. Mass 61

4.2 Trigger Efficiency vs. χ 63

5.1 Dijet Mass and Background Fit on a Log Scale 66

5.2 Dijet Mass and Background Fit: Fractional Difference and Residual 67

5.3 Dijet Mass Distribution and QCD Simulation Fit 70

5.4 Excited Quark Simulation 72

5.5 Jet Multiplicity, EM Fraction, Detector η and ϕ 74

5.6 Missing E_T, Charge Fraction, Track Multiplicity and Jet Mass . 75

5.7 Mass Distribution, Fit, and Limit for 200 and 550 GeV particles 80

5.8 Systematic Uncertainty in the Cross Section Limit 86

5.9 Upper Limit on Cross Section for New Particles without systematics 88

5.10 Upper Limit on Cross Section for New Particles 89

5.11 Limit on Excited Quarks in Mass vs. Coupling 91

6.1 Dijet Angular Distribution Before Acceptance Correction 97

6.2 Dijet Balance in the Data and Gaussian Fit for $2\bar{P}_t > 241$ GeV 102

6.3 Data and MC mean of P_t balance vs. $\bar{P}_t$ 105

6.4 Data and MC σ of P_t balance vs. $\bar{P}_t$ 106

6.5 Dijet Balance in the Data and Tuned MC for $2\bar{P}_t > 241$ 107

6.6 Acceptance for Tuned MC 110

6.7 Acceptance for Standard MC 111

6.8 Systematic Uncertainty on Acceptance for $M > 625$ GeV 112

6.9 Systematic Uncertainty on $R_\chi$vs. Mass 113

6.10 Total Systematic Uncertainty on R_χ vs. Mass 114

6.11 Dijet Angular Distribution compared to LO QCD 117

6.12 Dijet Angular Distribution compared to NLO QCD 118

6.13 Dijet Angular Distribution compared to QCD 119

6.14 Dijet Angular Ratio compared to QCD 120

6.15 Central Only Cross Check of Dijet Angular Distribution 124

6.16 Central Only Cross Check of Dijet Angular Ratio 125

6.17 Dijet Angular Ratio and Compositeness 128

6.18 Limits on Compositeness Scale 130

List of Tables

1.1 The elementary particles. 2

1.2 Subprocess cross sections for lowest order $2 \rightarrow 2$ processes . . . 9

1.3 Excited Quark Decay Modes and Branching Ratios 16

3.1 Level 1 Jet trigger calorimeter tower threshold. 44

3.2 Level 2 Jet E_T threshold and prescale factor. 46

3.3 Level 3 Jet E_T threshold. 47

4.1 Cosmic ray filter cut summary 58

4.2 Z vertex Cut efficiency 59

4.3 Triggers, Mass Cuts, Efficiency and Luminosity 64

5.1 QCD Simulation summary 69

5.2 Dijet Mass Data, QCD, and Background Fit 70

5.3 Results for Background Fits 79

5.4 Systematic Uncertainty. 87

5.5 Limits on new particle production. 92

6.1 Dijet balancing results. 103

6.2 Jet energy resolution fitting parameters. 104

6.3 Systematic Uncertainty on Acceptance. 115

6.4 χ Distribution, trigger efficiency, and acceptance 121

6.5 R_χ Distribution, trigger efficiency, and acceptance. 122

Chapter 1

Theory

1.1 Introduction to Standard Model

Decades of particle physics research has produced an elegant and concise theory of particle interactions at the subnuclear level, which is frequently referred to as the "Standard Model".

In the Standard Model, all matter is described as composed of quarks and leptons, which are pointlike, structureless, and spin-$\frac{1}{2}$ fermions. These fundamental fermions may be divided into three "generations" or "families":

First Generation	*Second Generation*	*Third Generation*
$\begin{pmatrix} e^- \\ \nu_e \end{pmatrix}$	$\begin{pmatrix} \mu^- \\ \nu_\mu \end{pmatrix}$	$\begin{pmatrix} \tau^- \\ \nu_\tau \end{pmatrix}$
$\begin{pmatrix} u \\ d \end{pmatrix}$	$\begin{pmatrix} c \\ s \end{pmatrix}$	$\begin{pmatrix} t \\ b \end{pmatrix}$

Each generation contains two "flavors" of quark and lepton. The leptons carry "lepton number" $L = +1$, but zero "baryon number", while the quarks have baryon number $B = +\frac{1}{3}$, but $L = 0$. In addition to flavor, baryon and lepton number, spin, and charge, the quarks have another intrinsic quantum

number: color. The "color" charges have three different values with the fundamental $SU(3)_C$ representation: "red" (R), "green" (G) or "blue" (B). Color is what distinguishes the quarks from leptons. Each particle has an associated anti-particle, which is identical in mass with the particle, but which has opposite charge and color. The quarks and leptons and some of their properties are shown in Table 1.1.

Table 1.1: The elementary particles.

Generation	Flavor	Charge	Spin	Colors	Mass
1	u (up)	+2/3	1/2	3	$\sim$ 6 MeV
	d (down)	−1/3	1/2	3	$\sim$ 10 MeV
	e (electron)	−1	1/2	No	0.511 MeV
	ν_e (neutrino)	0	1/2	No	$\leq$ 7 eV
2	c (charm)	+2/3	1/2	3	1.3 GeV
	s (strange)	−1/3	1/2	3	0.2 GeV
	μ (muon)	−1	1/2	No	0.1057 GeV
	ν_μ (neutrino)	0	1/2	No	$\leq$ 0.27 MeV
3	t (top)	+2/3	1/2	3	174 GeV
	b (bottom)	−1/3	1/2	3	4.3 GeV
	τ (tau)	−1	1/2	No	1.776 GeV
	ν_τ (neutrino)	0	1/2	No	$\leq$ 21 MeV

In the Standard Model, these fundamental particles undergo four known types of gauge interaction: gravitational, electromagnetic, and the weak and strong. If we leave aside gravitation, which is a negligible perturbation at the energy scales usually considered here, the other three interactions have an underlying unity and are all described by gauge theories mediated by spin 1 gauge bosons. The quarks experience all three interactions. The leptons participate only in the weak and electromagnetic interactions.

The electromagnetic and weak interactions are described by a unified elec-

troweak theory, which was provided by Glashow-Weiberg-Salam theory [1] based on the gauge group $SU(2)_L \otimes U(1)_Y$. In this theory, the local gauge invariance is spontaneously broken, or hidden, by the Higgs mechanism. This causes the intermediate bosons W^+, W^-, and Z^0 of weak interactions to acquire large masses and leaves the photon massless. A consequence of this form of spontaneous symmetry breaking is the existence of at least one scalar Higgs boson of unspecified mass. The $SU(2)_L \otimes U(1)_Y$ model has had a number of notable successes: The prediction and detailed description of the weak neutral current interaction observed later in experiment, the prediction of charm, and the predictions of the masses of the charged, and neutral intermediate bosons.

The strong interaction, which binds quarks together to form hadrons, is the strongest of the three interactions. It is described by a formal gauge theory called quantum chromodynamics (QCD). QCD is based on the exact local color gauge symmetry $SU(3)_C$. Strong interactions are mediated by an $SU(3)_C$ octet of colored spin 1 gauge bosons called gluons. The gauge symmetry is exact, and the gluons are massless particles. QCD is a non-Abelian theory, i.e., the gauge bosons (the gluons), carry color charges. This means that gluons, unlike photons in electrodynamics, can couple to themselves. This leads to an interesting property of colored objects called confinement. In QCD quarks and gluons are permanently confined within color singlet hadrons. A crucial property of non-Abelian gauge theories in general and of QCD in particular is asymptotic freedom, the tendency of the coupling strength to diminish at short distances. This behavior suggests a resolution to the parton model paradox that quarks behave as free particle within hadrons, but can never be liberated.

Finally, it is suspected that gravity is mediated by an as yet unobserved particle called the graviton and acts on all particles with mass. The strength of

the force between two quarks at a distance of 10^{-15} cm is $\sim 10^{-41}$ of the strength of the electromagnetic force. It is indeed a negligibly small perturbation at the energy scales usually considered!

The so called "Standard Model", QCD plus electroweak theory, describes all the principle systematics of elementary particle phenomenology and achieves a wide-ranging synthesis of elementary phenomena.

1.2 Quantum Chromodynamics and Jet Production

The success of QCD in describing the strong interactions is summarized by two terms: asymptotic freedom and confinement. These behaviors can be explained by the "running" coupling constant of the strong interaction, $\alpha_s(Q^2)$, which may be expressed to the lowest order as

$$\alpha_s(Q^2) = \frac{12\pi}{(33 - 2n_f)\ln(Q^2/\Lambda^2)}, \tag{1.1}$$

where Q^2 is the interaction momentum transfer scale, n_f is the number of quark flavors with mass less than Q, and Λ is the QCD scale parameter determined experimentally to be about 0.2 GeV.

The running of the strong coupling constant causes the strong interaction to be very different at short versus large distances. The effective coupling is very large at large distance (small Q^2) where the confinement of quarks occurs, but decreases to zero at short distance (large Q^2) where quarks and gluons are asymptotically free particles.

To understand the importance of these two attributes we should recall some

facts about the strong interactions. Hadron spectra are very well described by the quark model, and certain high energy cross sections are quite successfully described by a model in which the valence quarks do not interact at all. But quarks have never been seen in isolation. Any effort to produce single quarks at high P_T at high energy collision experiments leads to jets of the familiar mesons and baryons. Confinement means that quarks and gluons must be studied indirectly. From studying the "jet" one can learns about the initiating quark and gluon.

The Parton Model

Jet production in high energy hadron-hadron collisions, as depicted in Fig 1.1, is thought to arise from the hard scattering of the elementary constituents of the incident hadrons which can be regarded as collections of quasi free partons which sharing the momentum of the hadron. These constituents then scatter at wide angles and merge with outgoing partons to materialize into the hadrons that are observed experimentally.

The cross section for producing two jets at large P_t is factorized into a convolution of structure functions $f_a^{(h_1)}(x_{h_1}, Q^2)$, for finding parton constituent 'a' in hadron h_1 with momentum fraction x_{h_1}, and a hard scattering cross section $\hat{\sigma}_{ab\to cd}$ to be computed in perturbative QCD for the $2 \to 2$ parton-parton scattering subprocess $ab \to cd$.

The cross section is conveniently written in terms of the rapidities y_1 and y_2 of the two jets and their common transverse momentum p_t [2]. The differential cross section is given by

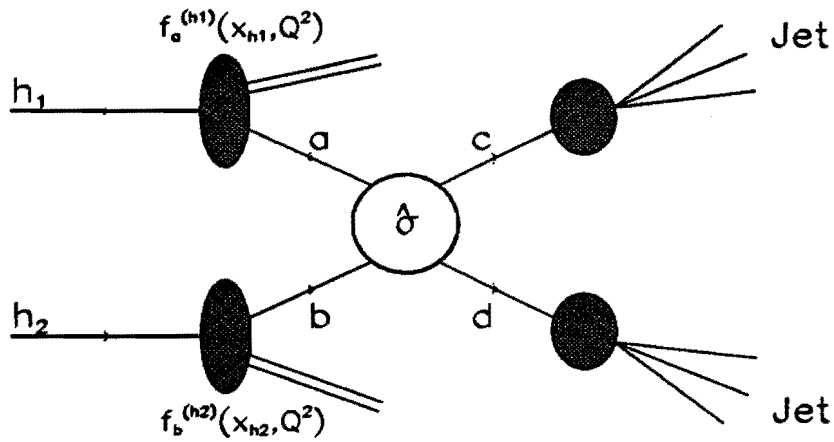

Figure 1.1: High energy hadron-hadron collision in the parton model

$$\frac{d\sigma}{dy_1 dy_2 dp_t} = \frac{2\pi\tau}{\hat{s}} p_t \sum_{a,b} \frac{\hat{\sigma}_{ab\to cd}(\hat{s},\hat{t},\hat{u})}{(1+\delta_{ab})} \quad [\ f_a^{(h_1)}(x_{h_1},Q^2) f_b^{(h_2)}(x_{h_2},Q^2) + f_b^{(h_1)}(x_{h_1},Q^2) f_a^{(h_2)}(x_{h_2},Q^2)]. \quad (1.2)$$

The quantities $\hat{s}$; $\hat{t}$, and $\hat{u}$ are parton level Mandelstam variables for the $2 \to 2$ parton-parton scattering subprocess $ab \to cd$, which are defined as

$$\hat{s} = (p_a^\mu + p_b^\mu)^2 \quad (1.3)$$

$$\hat{t} = (p_c^\mu - p_a^\mu)^2 \quad (1.4)$$

$$\hat{u} = (p_d^\mu - p_a^\mu)^2 \quad (1.5)$$

Defining

$$y_i = \frac{1}{2}\ln(\frac{E_i + P_{iz}}{E_i - P_{iz}}), \quad (i = 1,2) \quad (1.6)$$

$$y^\star = \frac{1}{2}(y_1 - y_2), \quad (1.7)$$

$$y_{boost} = \frac{1}{2}(y_1 + y_2), \tag{1.8}$$

we may write

$$\tau = \frac{4p_t^2}{\hat{s}} cosh^2 y^\star \tag{1.9}$$

and

$$x_{h_1} = \sqrt{\tau} e^{y_{boost}} \tag{1.10}$$

$$x_{h_2} = \sqrt{\tau} e^{-y_{boost}} \tag{1.11}$$

The invariant mass distribution of the two jets, within the rapidity region $[-Y, Y]$, is obtained by integrating y_1 and y_2 as

$$\frac{d\sigma}{d\mathcal{M}} = \frac{\pi \mathcal{M} \tau}{2} \int_{-Y}^{Y} dy_1 \int_{y_{min}}^{y_{max}} dy_2 \sum_{ab} \frac{\hat{\sigma}_{ab}(\hat{s}, \hat{t}, \hat{u})}{(1 + \delta_{ab})\ \hat{s}\ cosh^2 y^\star}$$
$$[f_a^{(h_1)}(x_{h_1}, Q^2) f_b^{(h_2)}(x_{h_2}, Q^2) + f_b^{(h_1)}(x_{h_1}, Q^2) f_a^{(h_2)}(x_{h_2}, Q^2)], \tag{1.12}$$

where $y_{min} \equiv max(-Y, ln \tan -y_1),\ and\ y_{max} \equiv min(Y, -ln\tau - y_2)$.

The subprocess cross section $\hat{\sigma}_{ab \to cd}$ is predicted by perturbative QCD. For the high momentum transfer parton-parton hard scattering process where the strong interaction becomes weaker, perturbation theory can be used. The Feynman rules for computing the cross section in terms of a perturbation expansion in the strong coupling α_s are determined from the QCD Lagrangian. It is straight forward to calculate the fundamental parton interaction cross section $\hat{\sigma}$ [3], at least at lowest order in perturbation theory, from the underlying theory. The expressions for the subprocess cross sections have been listed in Table 1.2 for all of the lowest order Feynman diagrams shown in Fig. 1.2.

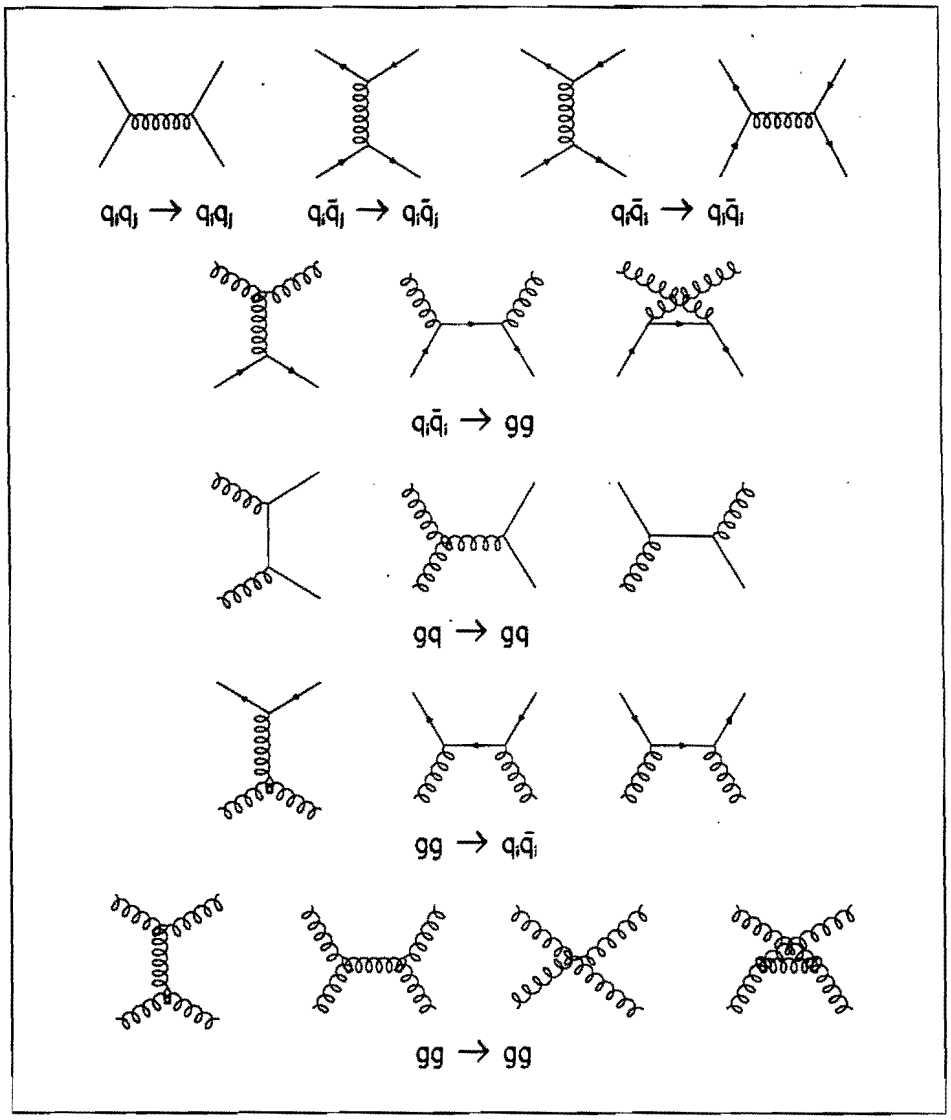

Figure 1.2: Lowest Order Feynman graph for $2 \to 2$ processes

Subprocess	$\sigma_{ab\to cd}(\hat{s},\hat{t},\hat{u})$
$q_iq_j \to q_iq_j$	$\frac{4\alpha_s^2}{9\hat{s}}\frac{\hat{s}^2+\hat{u}^2}{\hat{t}^2}$
$q_i\bar{q}_i \to q_j\bar{q}_j$	$\frac{4\alpha_s^2}{9\hat{s}}\frac{\hat{s}^2+\hat{u}^2}{\hat{t}^2}$
$q_i\bar{q}_i \to q_i\bar{q}_i$	$\frac{4\alpha_s^2}{9\hat{s}}[\frac{\hat{t}^2+\hat{u}^2}{\hat{s}^2}+\frac{\hat{s}^2+\hat{u}^2}{\hat{t}^2}+\frac{2\hat{u}^2}{3\hat{s}\hat{t}}]$
$q_i\bar{q}_i \to gg$	$\frac{8\alpha_s^2(\hat{t}^2+\hat{u}^2)}{3\hat{s}}[\frac{4}{9\hat{t}\hat{u}}-\frac{1}{\hat{s}^2}]$
$gg \to q_i\bar{q}_i$	$\frac{3\alpha_s^2(\hat{t}^2+\hat{u}^2)}{8\hat{s}}[\frac{4}{9\hat{t}\hat{u}}-\frac{1}{\hat{s}^2}]$
$gq \to gq$	$\frac{\alpha_s^2(\hat{s}^2+\hat{u}^2)}{\hat{s}}[\frac{1}{\hat{t}^2}-\frac{4}{9\hat{s}\hat{u}}]$
$gg \to gg$	$\frac{9\alpha_s^2}{2\hat{s}}[3-\frac{\hat{t}\hat{u}}{\hat{s}^2}-\frac{\hat{s}\hat{u}}{\hat{t}^2}-\frac{\hat{s}\hat{t}}{\hat{u}^2}]$

Table 1.2: Lowest Order Feynman graph for $2 \to 2$ processes

Parton Distribution Functions

In the naive parton model the distribution functions are independent of the momentum transfer, Q, of the hard scattering. However, this picture is only an approximation because, according to QCD, scaling will be violated at first order in α_s with $f_a^{(h_1)}(x_{h_1}) \to f_a^{(h_1)}(x_{h_1}, Q^2)$ as a result of gluon emission by the quarks and of $q\bar{q}$ creation by the gluons. In order to calculate the cross section, one must have available the relevant distributions at the appropriate Q scale. The quark and antiquark distribution functions are measured at low values of Q^2 in deep inelastic lepton scattering experiments and the gluon contribution is also inferred from the Q-dependence of these data in a model dependent way. The evolution of the parton distribution function with Q^2 can then be calculated using the Altarelli-Parisi equations [4] for distribution functions or their equivalent for the fragmentation functions. These are a set of coupled differential-integral equations that describe the Q^2 dependence of the quark and gluon distribution or fragmentation functions.

There are several widely used sets of parton distribution functions currently

available. Many recent sets have incorporated all relevant modern high statistics experimental results and are applied using the next to leading order (NLO) QCD formalism.

Parton Hadronization

QCD perturbation theory, formulated in terms of quarks and gluons, is valid at short distances. At long distances, QCD becomes strongly interacting and perturbation theory breaks down. In this confinement regime, the coloured partons are transformed into colorless hadrons by a process called either hadronization or fragmentation.

The fragmentation process has yet to be understood from first principles starting from the QCD Lagrangian. The natural way out has been the introduction of phenomenological models for jet fragmentation, implemented in terms of computer programs that generate complete events, which can be directly compared with experimental data. Three different approaches have been used extensively: independent fragmentation model [5], cluster fragmentation model and string fragmentation model [6].

The model used in our PYTHIA simulation in this analysis is the string fragmentation model. The string model is most easily illustrated for the production of a back-to-back $q\bar{q}$ jet pair. As the partons move apart, the physical picture is that of a colour flux tube stretched between the partons. The potential energy stored in the string increases. With the tube assumed to be uniform along its length, this automatically leads to a linear confinement picture. The string may break by production of a new $q'\bar{q}'$ pair, so that the system splits into two colour singlet systems $q\bar{q}'$ and $q'\bar{q}$. If the invariant mass of either of these systems is large enough, further breaks may occur until only ordinary

hadrons remain, each hadron corresponding to a small piece of string with a quark in one end and an antiquark in the other.

Although the jet fragmentation does not appear in the dijet cross section and the dijet invariant mass distribution formula, we are still concerned about it because the detector response to a jet depends on how the jet fragments. We will discuss these effects in detail in Chapter 3.

1.3 Beyond the Standard Model

Despite its great success, it is essential to recognize that the current Standard Model is not an ultimate theory and leaves a host of crucial problems open. For example, it fails to unify all the fundamental forces, and a large number of coupling constants and masses are left unspecified. Furthermore, the pattern of observed mass ratios and quantum numbers is rich in nontrivial unexplained features. The masses of charged fermions span several orders of magnitude. The iteration of three identical generations of quark and lepton flavors is impressive and without explanation. Many features are put in by hand with their profound origins remaining mysterious. This is at odds with our viewpoint, fostered by a history of repeated simplifications, that the world should be comprehensible in terms of simple laws. Given this, it is not surprising that there are many directions of theoretical speculation departing from the current Standard Model. Many of these have important implications which can be observed at the present time. The following sections describe the phenomena we will search for in this analysis.

All theoretical cross sections were calculated at lowest order using CTEQ2L [7] (leading order) parton distributions and one loop calculations of α_S using a

renormalization scale μ=M (mass of new particle). Each phenomena considered has a half-width at half maximum $\Gamma/2$ which is much smaller than our dijet mass resolution ($\sigma \approx 0.1M$).

1.3.1 Axigluons

The Standard Model offers a consistent description of all elementary particle phenomena and presents the threat of a desert at higher energies. In its minimal version, the only new particle awaiting discovery is the Higgs boson. But, is the standard theory unique? Like its electroweak sector, which is spontaneously broken from $SU(2)_L \otimes U(1)_Y \rightarrow U(1)_Q$ near the Fermi scale $M_F \approx 250GeV$, the strong interaction may be described by a larger chiral color group $SU(3)_L \times SU(3)_R$, which breaks to normal $SU(3)_C$ at some scale, leaving standard QCD at low energies. Unfortunately, there appears to be little motivation for this model, except perhaps that it predicts so many new particles that "the desert is turned into a teeming jungle" [8].

There are many different implementations of chiral models [8, 9], and all demand the existence of a wide variety of new particles. The most important model-independent prediction of chiral color is a massive color octet of gauge bosons, the axigluons.

Lagrangian

The axigluon is constrained by gauge invariance to couple to all quark flavors according to the following interaction lagrangian [10]:

$$\mathcal{L}_A = -ig_s t^a_{ij} \bar{q}^i \gamma_5 \gamma_\mu A^{\mu a} q^j, \tag{1.13}$$

where t^a_{ij} are the usual SU(3) color matrices. The axigluon cannot decay to two gluons because of parity conservation. So its dominate decay is expected to be to $q\bar{q}$.

Width and Branching Ratio

The width of the axigluon is given by [9]:

$$\Gamma_A = \frac{N_A \alpha_s M_A}{6}, \tag{1.14}$$

where N_A counts the number of open decay channels, i.e., the number of quarks with mass less than the $M_A/2$. We will assume a Standard Model version of axigluons in which $N_A = 5$ when the axigluon has mass less then $2M_t$ (M_t top quark mass) and $N_A = 6$ when the axigluon has mass greater than $2M_t$ but less than around a TeV. With this assumption $\Gamma_A/2 \approx .05M_A$ which is smaller than the CDF dijet mass resolution ($\sigma \approx 0.1M$). Additional families of quarks and leptons are required by this theory [8], but for convenience we will assume they have a mass greater than $M_A/2$. With these assumptions when $M_A < 2M_t$ the branching ratio to light quarks (u,d,s,c,b) is 1 and when $M_A > 2M_t$ the branching ratio is taken to be [10]:

$$BR(A \to q\bar{q}) = \frac{1}{5 + [1 - (2M_t/M_A)^2]^{3/2}}, \tag{1.15}$$

where $M_t = 174$ GeV/c^2.

Cross Section

One of the axigluon signatures at hadronic colliders is the appearance of an axigluon resonance in the dijet invariant-mass plot, which depends on the resonant production of s-channel axigluons as in Fig. 1.3.

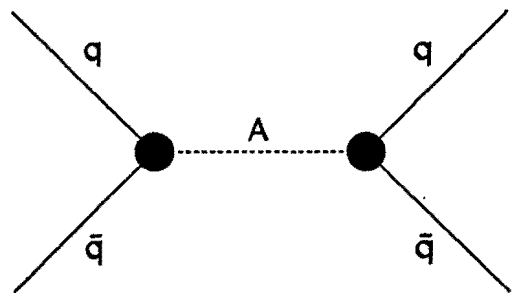

Figure 1.3: Quark-antiquark annihilation through axigluon exchange in the S-channel.

The production cross section is easily computed to be

$$\sigma = \int_{y_b^{min}}^{y_b^{max}} \frac{16\pi^2\alpha_s}{9s} L(x_p, x_{\bar{p}}) \mathcal{A}(y_b, y_{cut} \cos\theta^*_{cut}) dy_b, \tag{1.16}$$

where the minimum boost is y_b^{min}=max$(-y_{cut}, \ln\sqrt{\tau})$, the maximum boost is y_b^{max}=min$(y_{cut}, -\ln\sqrt{\tau})$, and $\tau = M^2/s = x_p x_{\bar{p}}$ with x_p and $x_{\bar{p}}$ being the momentum fraction of the quark and antiquark in proton and antiproton respectively. The parton luminosity in Eq. 1.16 is given by

$$L(x_p, x_{\bar{p}}) = \sum_i [f_{q_i}^{(p)}(x_p, M^2) f_{\bar{q}_i}^{(\bar{p})}(x_{\bar{p}}, M^2) + f_{\bar{q}_i}^{(p)}(x_p, M^2) f_{q_i}^{(\bar{p})}(x_{\bar{p}}, M^2)] \tag{1.17}$$

and $\mathcal{A}(y_b, y_{cut}, \cos\theta^*_{cut})$ is the acceptance for our jet rapidity and $\cos\theta^*$ cut, which is evaluated at each value of y_b within the integral using the axial-vector decay angular distribution

$$\frac{dN}{d\cos\theta^*} = 1 + \cos^2\theta^*. \tag{1.18}$$

This cross section is then multiplied by Eq. 1.15 to obtain the cross section times branching ratio we compare to our limit.

1.3.2 Excited Quarks

Compositeness is the most historically compelling extension of the standard model. Many times in the past physicists have assumed incorrectly that all the known particles were truly fundamental. Perhaps history will once again repeat itself. If quarks are composite particles then excited states are expected.

Lagrangian

For simplicity only the simplest kind of excited quark, one with spin 1/2 and weak isospin 1/2 is discussed. The Lagrangian for transitions between an excited quark of mass M^* and a quark plus a gauge boson ($q^* \leftrightarrow q+[\gamma, g, W, Z]$) is constrained by gauge invariance to be of magnetic moment type [11]:

$$\mathcal{L} = \frac{1}{2M^*}\bar{q}_R^*\sigma^{\mu\nu}(g_s f_s \frac{\lambda_a}{2}G^a_{\mu\nu} + gf\frac{\tau}{2}W_{\mu\nu} + g'f'\frac{Y}{2}B_{\mu\nu})q_L + h.c., \qquad (1.19)$$

where $G^a_{\mu\nu}$, $W_{\mu\nu}$, and $B_{\mu\nu}$ are the field-strength tensors of the gluon, the SU(2), and the U(1) gauge fields; Y is the weak hypercharge (baryon number + Strangeness), and g_s, g and g' are the gauge coupling constants. Finally f_s, f and f' are unknown couplings determined by the composite dynamics and are all assumed to be equal to one.

Width and Branching Ratios

Production of a single excited quark will take place in hadronic collisions via quark gluon fusion. The excited quark can then decay into a common ground state quark and any gauge boson. The relative decay rates [11] are listed in Table 1.3.

Decay Mode	Br. Ratio(%)	Decay Mode	Br. Ratio(%)
$u^* \to ug$	83.4	$d^* \to dg$	83.4
$u^* \to u\gamma$	2.2	$d^* \to d\gamma$	0.5
$u^* \to dW$	10.9 ($e\nu$ 1.2)	$d^* \to uW$	10.9 ($e\nu$ 1.2)
$u^* \to uZ$	3.5 (ee .27)	$d^* \to dZ$	5.1 (ee .39)

Table 1.3: The decay modes and branching ratios of excited up and down quarks for $f_s = f = f'$ and $\alpha_s = 0.1$.

Expressions for the partial decay rates are given in reference [11]. The q^* half width for $f_s = f = f'$ is approximately given by

$$\frac{\Gamma(q^*)}{2} \approx 0.02 f^2 M^*, \tag{1.20}$$

which for $f \leq 1$ is significantly narrower than our dijet mass resolution.

Cross Section

The invariant mass distribution of the final state quark and gauge bosons for $p\bar{p} \to Q^* \to q'V$ ($V = g, \gamma$, W, and Z) is given by

$$\frac{d\sigma}{dm}(p\bar{p} \to Q^* \to q'V) = \frac{2}{m}\int_{ln\sqrt{\tau}}^{-ln\sqrt{\tau}} dy\tau\mathcal{L}(x_1, x_2)\hat{\sigma}(m^2)\mathcal{A}(y, y_{cut}, \cos\theta^*_{cut}), \tag{1.21}$$

where $\tau = x_1 x_2 = m^2/s$, $y = \frac{1}{2}ln(\frac{x_1}{x_2})$, s is the $p\bar{p}$ center of mass energy squared, and the partonic cross section is given by

$$\hat{\sigma}(m^2) = \pi\frac{\hat{\Gamma}(Q^* \to q'V)\hat{\Gamma}(Q^* \to q'g)}{(m^2 - M^{*2})^2 + \hat{\Gamma}(Q^*)M^{*2}} \tag{1.22}$$

with

$$\hat{\Gamma}(Q^* \to q'V) = \frac{{f_V}^2(m^2)}{{f_V}^2}[\frac{m}{M^*}]^3\Gamma(Q^* \to q'V) \tag{1.23}$$

and

$$\hat{\Gamma}(Q^*) = \sum_V \Gamma(Q^* \to q'V) \tag{1.24}$$

$\mathcal{A}(y, y_{cut}, \cos\theta^*_{cut})$ is the acceptance for our jet rapidity and $\cos\theta^*$ cut, and

$$\mathcal{L}(x_1, x_2) = q(x_1, m^2)g(x_2, m^2) + q(x_2, m^2)g(x_1, m^2) \tag{1.25}$$

is the luminosity function for Q^* production.

1.3.3 Technirhos

The origin of electroweak symmetry breaking is arguably the last remaining puzzle of the Standard Model. Symmetry breaking arising from a fundamental Higgs boson is admittedly ad hoc. Instead, technicolor assumes that pairs of fundamental techniquarks are bound into a composite scalar, a technipion, which generates a dynamical symmetry breaking. The mechanism is similar to the way Cooper pairs [12] of electrons generate a superconducting phase transition in the BCS theory of superconductivity. In a recent technicolor model [13, 14] there also exists a color octet technirho (ρ_T) which couples to $q\bar{q}$ and gg via a virtual intermediate gluon ($\rho_T \to g \to q\bar{q}, gg$). Here we search for ρ_T in the dijet channel as depicted in Fig. 1.4.

Width and Branching Ratios

In the technicolor model [14] we assume that all the various technipions have a mass that is greater than half the mass of ρ_T which consequentially can decay only to dijets. The branching ratio is therefore 100% to dijets. The width of the ρ_T is given by it's decays into gluons and five species of light quarks with

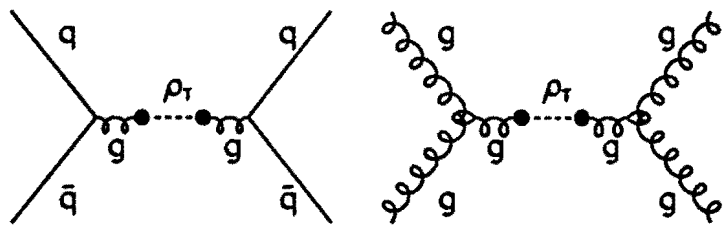

Figure 1.4: Feynman graphs for technirho (ρ_T) production and decay into dijet channel.

a relative decay rate of three to one [13, 14]:

$$\Gamma = (1 + 5/3) * \frac{\alpha_s^2}{\alpha_{\rho_T}} M_{\rho_T}, \tag{1.26}$$

where the technirho coupling constant α_{ρ_T} is related to the $\rho_T \to \pi_T \pi_T$ decay constant g_{ρ_T} as

$$\alpha_{\rho_T} \equiv \frac{g_{\rho_T}^2}{4\pi} \approx 2.97 \frac{3}{N_{TC}}. \tag{1.27}$$

Here g_{ρ_T} is assumed to be scaled from the constant for $\rho \to \pi\pi$ in QCD, and $N_{TC} = 6$ is the number of technicolors. The resulting half width of the technirho $\Gamma/2 \approx .01 M_{\rho_T}$ is an order of magnitude less than the dijet mass resolution $\sigma \approx .1M$.

Cross Section

The dijet invariant-mass distribution in a $p\bar{p}$ collider with center-of mass energy $\sqrt{s}$, where both jets are required to have rapidity $|y_{1,2}| < y_{cut}$ and $|\cos\theta^*| <$

$\cos\theta^*_{cut}$, is given by [13]

$$\frac{d\sigma(p\bar{p} \to jet\ jet)}{d\mathcal{M}} = \frac{2\mathcal{M}}{s}\int_{-Y_B}^{Y_B} dy_B \int_{-Z_0}^{Z_0} dz \sum_{i,j} f_i^{(\bar{p})}(\sqrt{\tau}e^{Y_B}) f_j^{(p)}(\sqrt{\tau}e^{-Y_B})$$

$$\frac{1}{2}\sum_{k,l}\frac{d\hat{\sigma}(ij \to kl)}{dz}, \tag{1.28}$$

where $z(\equiv cos\theta^* = 2\hat{t}/\hat{s}+1)$ is the scattering angle. The quantity $\tau = \mathcal{M}^2/s, y_B$ is the boost rapidity of the subprocess frame, and the rapidities y_1, y_2 of the produced jets are related to y_B and z by

$$y_{1,2} = y_B \pm \frac{1}{2}ln[\frac{(1+z)}{(1-z)}]. \tag{1.29}$$

The cut on the jet rapidities corresponds to the limits

$$\begin{aligned} Y_B &= min[y_{cut}, -\frac{1}{2}ln\tau] \\ z_0 &= min[cos\theta^*_{cut}, tanh(Y - |y_B|)] \end{aligned} \tag{1.30}$$

In Eq. 1.28, $d\hat{\sigma}(ij \to kl)/dz$ is the subprocess cross section. All subprocesses involved are presented in reference [13]. The analysis is complicated by the fact that there is no direct coupling between the technirho and $q\bar{q}$ or gg, only an indirect coupling that originates from a mixing between the technirho and a virtual gluon. The technirho comes into the cross section through the interference between pure QCD and technicolor in a complex propagator D_{gg} in the subprocess cross sections:

$$D_{gg} = \frac{D^2}{Q^2(D^2 - 2\alpha_s Q^2 D/\alpha_{\rho_T})}, \tag{1.31}$$

where the complex number $D = Q^2 - M^2 + iQ\Gamma$ contains the technirho. This produces a peak that is very much like a Breit-Wigner. The resonance peaks at

a dijet mass 8%±0.5% higher than the input technirho mass parameter because of QCD corrections (see equation 2.27 in reference [13]). Since QCD corrected mass peak is the observable variable, we will set limits on that instead of the input technirho mass parameter.

1.3.4 New Gauge Bosons

New gauge bosons, W' and Z', appear in certain attempts to enlarge the $SU(2)_L \otimes U(1)_Y$ gauge group of the standard model. For example, left-right handed symmetric models [15, 16] feature a right-handed $SU(2)_R$ and corresponding new gauge bosons, including heavier right handed W' and Z'.

Width and Branching Ratios

We assume the W' and Z' are just heavier versions of the conventional Standard Model W and Z, which means that the new gauge bosons have the same couplings as for the ordinary W and Z.

Under these assumptions the half width of the W' and Z' are given by

$$\frac{\Gamma_{W'}}{2} = \frac{\Gamma_W}{2}\frac{M'_W}{M_W} \tag{1:32}$$

$$\frac{\Gamma_{Z'}}{2} = \frac{\Gamma_Z}{2}\frac{M'_Z}{M_Z} \tag{1.33}$$

Here $\Gamma_W \approx 2.0GeV$ and $\Gamma_Z \approx 2.5GeV$. The half width of the W' and Z' are significantly less than the dijet mass resolution $\sigma \approx .1M$.

Since the couplings for $W'q\bar{q}'$ and $Z'q\bar{q}$ are taken as in the Standard Model, the corresponding widths are given by [15]

$$\Gamma_{W'\to q\bar{q}'} = \frac{\alpha}{12}N_c\frac{M_{W'}}{sin^2\theta_w} \tag{1.34}$$

$$\Gamma_{Z'\to q\bar{q}} = \frac{\alpha}{48} N_c \frac{M_{Z'}}{sin^2\theta_w cos^2\theta_w}[1 + (1 - 4|Q_q|sin^2\theta_w)^2], \qquad (1.35)$$

where $N_c = 3$, and Q_q is the quark electric charge.

The branching ratios for W' and Z' in the dijet channel are equal to the branching ratios to the five light quarks.

$$B(W' \to q\bar{q}') = \frac{\sum_{q,q'\neq t} \Gamma_{W'\to q\bar{q}'}}{\Gamma_{W'}} \qquad (1.36)$$

$$B(Z' \to q\bar{q}) = \frac{\sum_{q\neq t} \Gamma_{Z'\to q\bar{q}}}{\Gamma_{Z'}} \qquad (1.37)$$

Cross Section

The new gauge bosons production cross sections can be obtained from the ordinary W and Z production cross sections by replacing $M_{W,Z}$ with $M_{W',Z'}$. For example, the subprocess cross section of hadronic W' production is given by [17]

$$\hat{\sigma}(q\bar{q}' \to W') = 2\pi|V_{q\bar{q}'}|^2 \frac{G_F}{\sqrt{2}} M_{W'}^2 \delta(\hat{s} - M_{W'}^2). \qquad (1.38)$$

The differential cross section for hadronic W' production is the convolution of the subprocess cross section with the quark densities, including a color factor of $\frac{1}{3}$,

$$\frac{d\sigma(p\bar{p} \to W')}{dx_p dx_{\bar{p}}} = \frac{K}{3} \sum_q f_q^{(p)}(x_p, M_{W'}^2) f_{\bar{q}'}^{(\bar{p})}(x_{\bar{p}}, M_{W'}^2) \hat{\sigma}(q\bar{q}' \to W')\mathcal{A}. \qquad (1.39)$$

Here the usual K factor [17] takes into account the first order QCD corrections,

$$K \approx 1 + \frac{8\pi}{9}\alpha_s(M_{W'}^2) \qquad (1.40)$$

and the variable $\mathcal{A}$ is the kinematic acceptance that is discussed below. It is convenient to get the total hadronic W' production cross section by integrating over the variables $m = \sqrt{\hat{s}}$ and $y_b = (y_1 + y_2)/2 = (1/2)\ln(x_p/x_{\bar{p}})$ rather than x_p and $x_{\bar{p}}$, so we transform to these variables using $dm\ dy_b = (s/2m)dx_{\bar{p}}\ dx_p$. In this integral the kinematic acceptance is

$$\mathcal{A} = \mathcal{A}(y_b, y_{cut}, cos\theta^*_{cut}). \tag{1.41}$$

The production cross section for Z' can be obtained from Z in the same way.

1.3.5 E_6 Diquarks

Superstring theory in 10 dimensions, which holds the prospect of unifying all forces including gravity, is anomaly free if the gauge group is $E_8 \times E_8$. The compactification of the extra 6 dimensions can lead to E_6 as the grand unification group for the strong and electroweak interactions. The E_6 models in turn predict the existence of many kinds of new particles [10, 18, 19], including a color triplet scalar diquark $D(D^c)$ with charge $-1/3(+1/3)$ which couples to $\bar{u}\bar{d}(ud)$. Thus the discovery of a dijet mass resonance could indicate an E_6 diquark and be interpreted as evidence for a "theory of everything".

Lagrangian

The interaction Lagrangian for transitions between E_6 diquarks and up and down quarks is [10]:

$$\mathcal{L}_D = \lambda\epsilon_{ijk}\bar{u}^{ci}\frac{1-\gamma_5}{2}d^j D^k + \frac{\lambda_c}{2}\epsilon_{ijk}\bar{u}^i\frac{1+\gamma_5}{2}d^c{}^j D^c{}^k + h.c., \tag{1.42}$$

where it is commonly assumed that the unknown couplings are of electromagnetic strength ($\lambda = \lambda_c = e$) and that the masses are degenerate ($M_{D^c} = M_D$).

Width and Branching Ratio

Assuming electromagnetic strength Yukawa couplings, the width of the E_6 diquarks is given by [18]:

$$\Gamma_D = \alpha M_D, \qquad \Gamma_{D^c} = \alpha M_{D^c}/4, \tag{1.43}$$

where $\alpha = \lambda^2/4\pi$ is the electromagnetic coupling constant which is 1/128 after running to high masses. E_6 diquarks in the first family decay into u and d quarks only. The branching ratio to dijets is 100%.

Cross Section Calculation

The E_6 diquark cross section is obtained from integrating the subprocess cross sections. Following reference [18], the differential cross section for D is given by:

$$\frac{d^2\sigma}{dx_p dx_{\bar{p}}} = \frac{\hat{s}}{108\pi} \frac{16\lambda}{(\hat{s} - M_D^2)^2 + \Gamma_D^2 M_D^2} [\bar{u}(x_p)\bar{d}(x_{\bar{p}}) + \bar{u}(x_{\bar{p}})\bar{d}(x_p)]\mathcal{A} \tag{1.44}$$

and similarly for $\bar{D}$ with $\bar{q} \rightarrow q$ in the parton distributions. The cross section for D^c is given by

$$\frac{d^2\sigma}{dx_p dx_{\bar{p}}} = \frac{\hat{s}}{108\pi} \frac{\lambda}{(\hat{s} - M_{D^c}^2) + \Gamma_{D^c}^2 M_{D^c}^2} (u(x_p)d(x_{\bar{p}}) + u(x_{\bar{p}})d(x_p))\mathcal{A} \tag{1.45}$$

and similarly for $\bar{D}^c$ with $q \rightarrow \bar{q}$ in the parton distributions. In Eq. 1.44 and 1.45, $\hat{s} = s x_{\bar{p}} x_p$, and the variable P is the kinematic acceptance that is discussed below. Like the new gauge boson case, It is more convenient to

integrate over the variables m and y_b by transforming to these variables using $dm\ dy_b = (s/2m)dx_{\bar{p}}\ dx_p$ and then integrate Eq. 1.44 and Eq. 1.45 from y_b^{min} to y_b^{max} to obtain the Breit-Wigner $d\sigma/dm$ for the diquark resonance. In this integral the kinematic acceptance is

$$\mathcal{A} = \mathcal{A}(y_b, y_{cut}, cos\theta^*) \tag{1.46}$$

which is the probability that both final state partons pass our cuts in rapidity and $cos\theta^* = \tanh(y^*) = \tanh(y_1 - y_2)$ as a function of the variable y_b.

Chapter 2

Experimental Apparatus

2.1 The Tevatron Collider

The Tevatron Collider at Fermi National Laboratory is currently the world's highest energy accelerator, colliding protons with antiprotons at center of mass energy $\sqrt{s} = 1.8$ TeV. A schematic drawing of the Fermilab Collider is shown in Figure 2.1.

Protons are accelerated in the Tevatron up to 900 GeV through several stages. In the first step, negative hydrogen ions are released in a device called a Cockcroft-Walton accelerator, which produces an electromagnetic field to propel the ions to an energy of 750 KeV. The ions then enter a linear accelerator (Linac) to boost their energy to 400 MeV. The ions then pass through a carbon foil, striping the electrons off the ions.

In the second step, the protons are guided into the booster where the energy is raised to 8 GeV. Then protons are assembled in bunches and enter the Main Ring, where they are accelerated up to 150 GeV. The protons are then transferred to the Tevatron ring where they await the antiprotons.

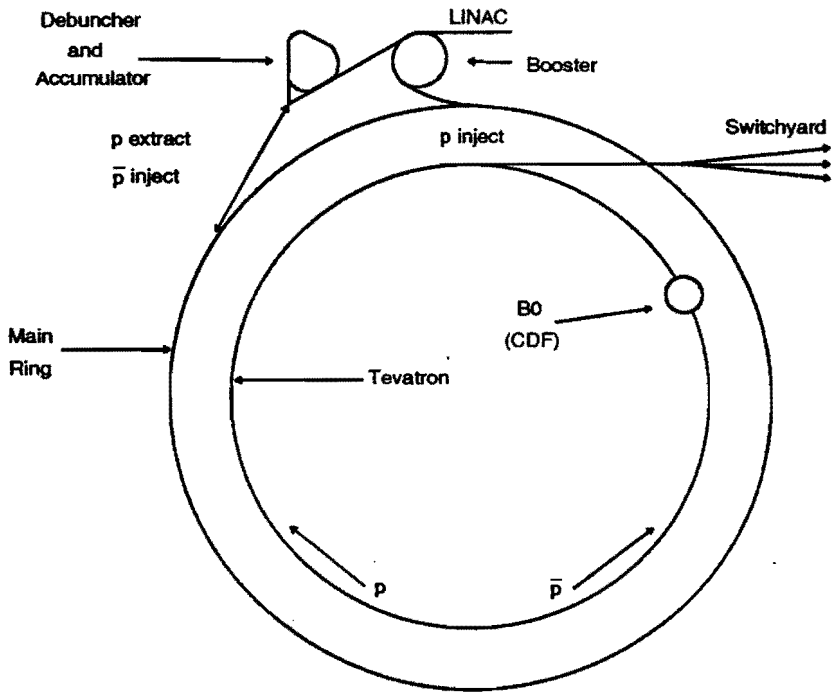

Figure 2.1: Schematic of the Fermilab accelerator complex. The main ring and the Tevatron physically occupy the same tunnel. The CDF experiment is located at the B0 interaction region, as shown.

The Main Ring also provides primary protons at 120 GeV to the antiproton source. The protons are focused into short bunches at 120 GeV. They are then extracted from the main ring and strike a copper target, producing antiprotons. The antiprotons are collected and focused through a lithium lens. Then the antiprotons are directed to the first antiproton storage ring, known as the Debuncher. The Debuncher uses two cooling processes, called debunching and stochastic cooling, to reduce the momentum spread and transverse motion of the antiprotons. After the Debuncher squeezes the antiproton energy and bunch size, they are sent to the Accumulator. After enough antiprotons are

accumulated, a portion of the stored antiproton beam is transferred to the Main Ring. The antiprotons are boosted to 150 GeV in the Main Ring and then injected into the Tevatron ring where protons have been circulating. Because the protons are positively charged and the antiprotons are negatively charged, the protons circulate in a direction counter to that of the antiprotons. The antiproton bunches pass through the proton bunches many times, but at this stage the bunches are much too diffuse for significant collisions to take place.

During the final step, both bunches of proton and antiproton are accelerated to full energy 900 GeV. Strong quadrupole magnets in the Tevatron's ring then squeeze the particles together. The beam cross sections are focused down to a diameter of about 0.1mm. The focusing greatly increases the density of each bunch. The protons and antiprotons then collide at the B0 and D0 interaction regions at a center of mass energy of 1800 GeV.

2.2 The Collider Detector at Fermilab (CDF)

In this section, an overview of the CDF detector will first be provided, together with a more detailed description of the components used to make jet measurements. Full details of the detector can be found elsewhere [20].

CDF (Collider Detector at Fermilab) is a general purpose detector that surrounds the B0 interaction region of the Fermilab Tevatron. It was designed for testing many different predictions of the Standard Model and also to search for processes beyond the Standard Model.

To provide such general-purpose measurements, CDF is a combination of several detector components. It is a forward-backward and azimuthally symmetric detector with its geometric center positioned at the nominal collision

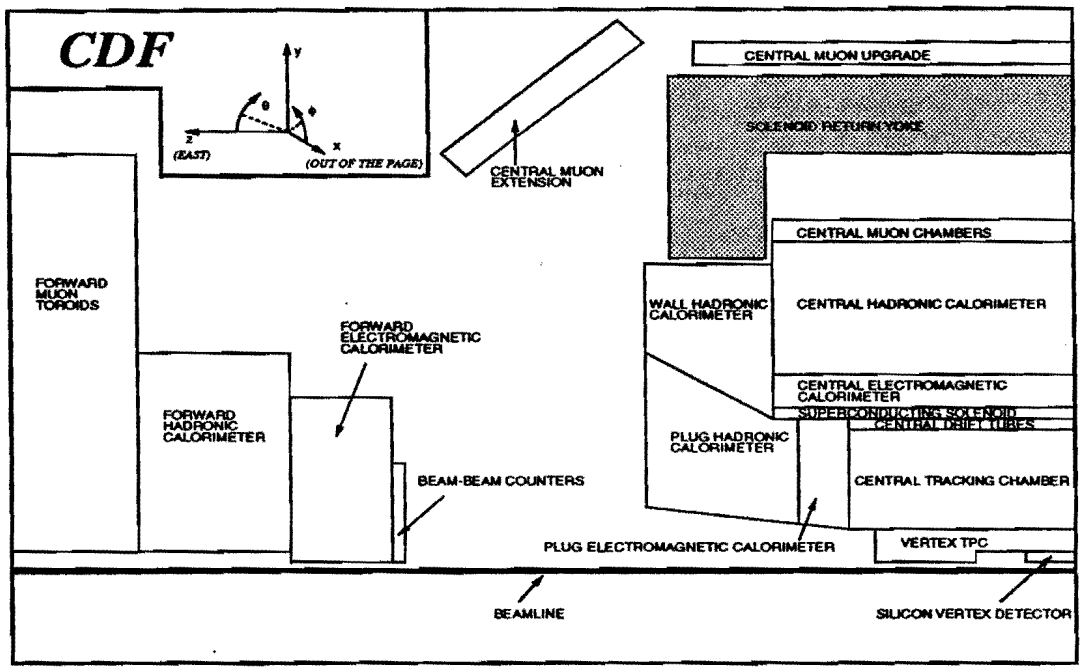

Figure 2.2: A side view cross section of the CDF detector. The detector is forward-backward symmetric about the interaction region, which is shown at the lower right corner of the figure. The proton direction is to the left, along the positive z axis.

point. Its coverage includes the full azimuthal range and extends to within 2° of the beam axis on either end. A side view of one half of the detector is shown in Figure 2.2.

Starting at the collision point and moving outward, the final-state particles first traverse the thin beryllium shell of the Tevatron beam-pipe. Then the Silicon Microvertex Detector (SVX) which is designed to track particles very near the interaction point and distinguish sequential decay vertices on the tens of microns level. Further out from the beam pipe is the Vertex Chamber (VTX) that is designed to measure tracks with high resolution in (z,r) coordinates. The particles then traverse the Central Tracking Chamber (CTC) that measures the

position and curvature of the charged particle trajectory. Outside the tracking chambers is a superconducting magnet which immerses the tracking chambers in a 1.5 Tesla solenoidal field. Surrounding the magnet are electromagnetic and hadronic calorimeters for measuring the energy of the particles. Beyond the calorimeters are muon detectors.

The CDF coordinate system takes the direction of the proton beam to be the positive z-axis. The y-axis points upward; the x-axis points radially out of the Tevatron ring in compliance with the right-hand rule. The azimuthal angle ϕ is measured from the positive x-axis; the polar angle θ is measured with respect to the positive z-axis. At CDF a polar coordinate is generally given in terms of the pseudorapidity η, which is defined as

$$\eta = -\ln(\tan\frac{\theta}{2}), \tag{2.1}$$

η is equivalent to rapidity, y, for a massless particle where rapidity is defined as

$$y = \frac{1}{2}\ln(\frac{E+P_z}{E-P_z}). \tag{2.2}$$

If $E \gg m$ then $\eta \cong y$. Particle production in $\overline{P}P$ collisions is best described in terms of y and P_T. This is because, if the system is Lorentz boosted along the z axis with a velocity u, the P_T is unchanged and y is a simple additive quantity

$$y' = y + y_{boost}, \tag{2.3}$$

where

$$y_{boost} = \frac{1}{2}\ln(\frac{1+u}{1-u}). \tag{2.4}$$

This simplicity of the transformation is important because the scattered quark system is often boosted in the z direction. This is because, although the

proton and antiproton have equal beam energy, the constituent quarks do not necessarily carry equal fractions of proton and antiproton momentum. For this reason, we will often use η in describing both the detector geometry and the particle kinematics.

The following sections describe of the CDF components used in this analysis in more detail.

2.2.1 The Tracking system

The Silicon Detector (SVX)

The detector component closest to the interaction point is the silicon vertex detector (SVX) [21]. This detector was installed for the 1992-1993 run, as part of the upgrade of the original CDF tracking system. It was replaced with the radiation-hard SVX′ in 1994. The SVX is designed to track particles very near the interaction point to a precision of about 10 microns. It is used to improve tracking resolution via precise determination of the beam interaction position. This precision also enables it to reconstruct the secondary vertices arising from c and b quark decays.

The SVX consists of two independent cylindrical modules (barrels), laid end-to-end, with the nominal beam-beam interaction point in the center between them. It is 51 cm long and its acceptance covers about 60% of the interaction region. The SVX contains 4 radial layers of silicon strip detectors with the strip parallel to the beam. The inner and outer radii are approximately 3 and 7.9 cm. It provides information in the transverse $(r - \phi)$ plane, with a resolution of approximately 15 μm in each layer. One of the barrels is shown in Figure 2.3. The SVX barrels each have twelve 30° ϕ-wedges. In order

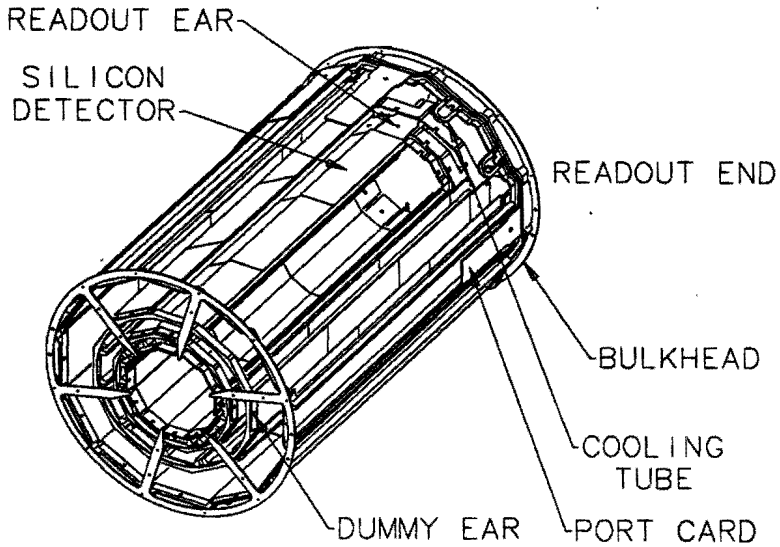

Figure 2.3: Isometric view of the SVX.

to obtain a length of 25.5 cm along the beam direction, three silicon detectors of 8.5 cm each were electrically bonded together. A group of three connected detectors is called a "ladder" and it is the basic subdivision of the device. The structure of one ladder is shown in Figure 2.4. The total number of readout channel is 46,080 in SVX.

The Vertex Time Projection Chamber

The vertex time projection chamber (VTX) [22] system consists of eight adjacent octagonal chambers surrounding the SVX and beamline in the region $|\eta| < 3.25$ and having an outer radius of 22 cm. It provides tracking information that gives a good z and θ measurement, which is then used to determine the interaction vertices.

Each VTX module contains a central high voltage grid that divides it into

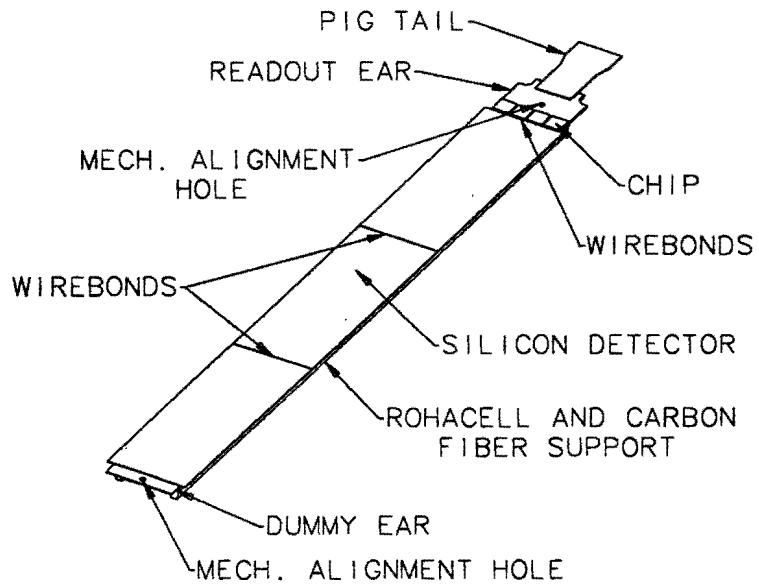

Figure 2.4: Schematic view of one SVX ladder.

two 12.25 cm long drift regions. The modules are filled with an argon-ethane mixture. At the end of each module are two end caps, divided into octants, with 24 sense wires and 24 cathode pads in each. The arrival times of the electrons at the sense wires provide an event picture in the $r-z$ plane. Adjacent modules are rotated relative to each other by 11.3° about the beam axis. This provides ϕ information from small angle stereo. By combining the $r-z$ information from the wires and the ϕ information from the pads, a three-dimensional track can be accurately reconstructed and the event vertices can be determined with a resolution of 1 mm.

The Central Tracking Chamber (CTC)

The central tracking chamber (CTC) [23] is a 3.2 meter long cylindrical drift chamber encased in a superconducting solenoid magnet of central field 1.4 Tesla. It provides three dimensional tracking and high-resolution momentum

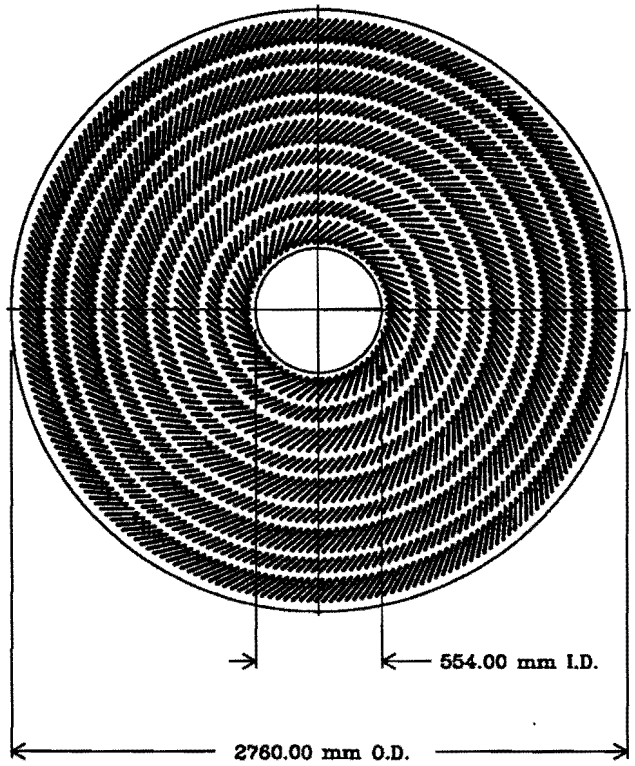

Figure 2.5: Endplate of the Central Tracking Chamber.

measurement for charged particle in a angular region -1.2 < η < 1.2. The resolution for the CTC is $\frac{\delta p_T}{p_T} = 0.0011 p_T$ for tracks from known position of the Tevatron beam ($\frac{\delta p_T}{p_T} = 0.002 p_T$ without the beam constraint).

The chamber is made up of a large cylindrical drift cells arranged in 9 superlayers, containing a total of 84 layers of sense wires as shown in Figure 2.5. Five axial superlayers each consist of 12 sense wires parallel to the beam axis; Four stereo superlayers each consist of six sense wires tilted by 3° relative to the beam axis; The axial or stereo superlayers alternate. The 5 axial superlayers

provide measurements of the position of charged particles in the $r - \phi$ plane with a spatial precision per hit about 200 μm. Combined with the information from the axial and stereo superlayers this provides z information for tracks with a resolution of 6 mm.

2.2.2 The Calorimetry

The CDF calorimeters were the most important detector subsystems used in this analysis. Jets were reconstructed and their four-momenta determined solely from their energy depositions in the calorimeters.

CDF calorimetry coverage is complete in azimuth and extends to within about 2° of the proton-antiproton beam axis. The calorimeters are grouped into three different sections: central ($|\eta|$ <1.1), plug (1.1< $|\eta|$ <2.2) and forward (2.2< $|\eta|$ <4.2). Each section consists of an electromagnetic calorimeter and a hadronic calorimeter. They are segmented into projective towers which point back to the nominal interaction point at the center of the detector. While lead and iron are the interactive medium for the electromagnetic and hadronic calorimeters respectively, the collection or sampling media are regionally dependent. In the central calorimeter the sampling medium is scintillator, while for the Plug and Forward regions it is gas proportional chambers with segmented cathode pad readout.

The Central Calorimetry

The CDF central calorimeters are also constructed in a projective tower geometry. Each tower covers approximately 0.1 units of pseudo-rapidity and 15° of azimuthal angle ϕ: this segmentation is small enough that a typical jet is spread over multiple towers. Each half of the central detector is divided into 24

wedge-shaped modules that are arranged in a barrel around the solenoidal coil and provide nearly full azimuthal coverage. Each wedge is 15° in ϕ. Figure 2.6 is a cutaway view of a single wedge which contains 10 towers. The central calorimeters can be pulled apart for servicing or access to the inner detector components.

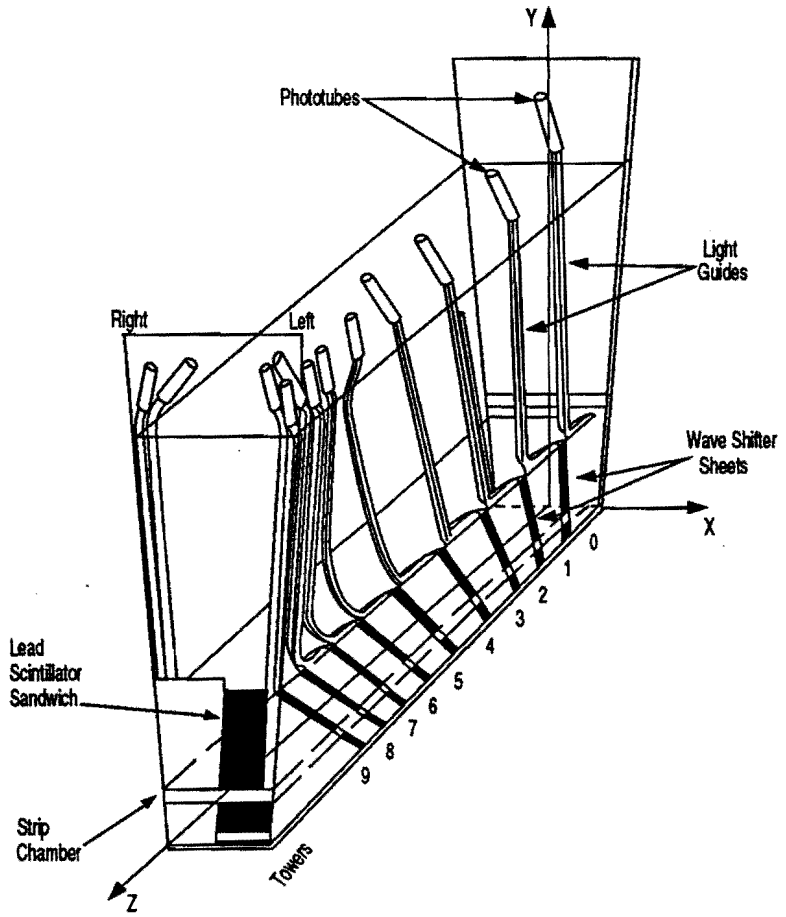

Figure 2.6: View of one wedge of the central calorimeter. The Central Electromagnetic Strip (CES) proportional chamber is embedded at shower maximum.

The central electromagnetic calorimeter (CEM) [24] consists of 31 layers of polystyrene scintillator interleaved with 30 layers of lead absorber. The

calorimeter is 18 radiation lengths (0.6 absorption lengths). Electrons and photons that interact with the lead will generate an electromagnetic shower through bremsstrahlung and pair production. The total number of particles created in this shower will be proportional to the energy of the incoming particle; therefore the number of photons coming out of the scintillator will be proportional to the initial particle's energy. Light from the scintillators is read out through wavelength shifters on both sides of a wedge in projective slices of the calorimeter that cover 0.1 units of η per cell. The energy resolution for electrons centered in towers is given by

$$\frac{\sigma_E}{E} = \frac{13.7\%}{\sqrt{E_T}} \oplus 2\%, \tag{2.5}$$

where energy E_T ($E_T = E \sin\theta$) in GeV and the symbol $\oplus$ signifies that the constant term is added in quadrature in the resolution.

The CEM is a hybrid detector, that incorporates a strip chamber (CES) near shower maximum to determine shower position and transverse development. The CES is a gas proportional chamber. Sixty-four wires positioned parallel to the beam gather information in $R - \phi$ views, while 128 stripes perpendicular to the wires give z information. The position resolution of the CES is on the order of 2 mm by 2 mm. Figure 2.7 shows the orientation of the cathode strips and anode wires.

Behind the CEM are two iron-scintillator hadron calorimeters: the central hadron (CHA) [25] and the endwall (WHA), which cover the ranges $0 < |\eta_d| < 0.9$ and $0.6 < |\eta_d| < 1.1$ respectively. The central hadronic calorimeter uses steel absorber interspersed with acrylic scintillator as the active medium. There are 32 layers of 2.5 cm thick steel and 1 cm thick scintillator, making a

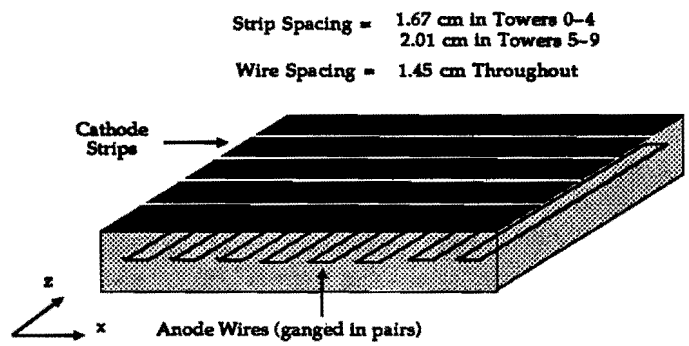

Figure 2.7: A schematic diagram of a CES chamber.

total thickness of 4.7 absorption lengths. The resolution of the CHA is

$$\frac{\sigma_E}{E} = \frac{50\%}{\sqrt{E_T}} \oplus 3\% \tag{2.6}$$

for isolated pions.

The wall hadronic calorimeter is designed to complete the pseudorapidity coverage of the CEM where the CHA left off. It is located outside the barrel endwall of the detector and covers the range $0.9 < |\eta| < 1.3$. The WHA employs the same type of the detector as CHA at a similar thickness of 4.5 pion absorption lengths, except that the WHA uses a 5 cm steel sampling size instead of 2.5 cm for the CHA. This reduces the resolution of the WHA with respect to the CHA. Its energy resolution is

$$\frac{\sigma_E}{E} = \frac{75\%}{\sqrt{E_T}} \oplus 4\%. \tag{2.7}$$

The Plug Calorimetry

The plug calorimeters consist of the plug electromagnetic calorimeter (PEM) [26] and the plug hadronic calorimeter (PHA) [27]. Both calorimeters employ

gas multi-wire proportional chambers to measure the showers. The central calorimeters use scintillators for good energy resolution, but in the more forward region of the detector, the radiation exposure becomes too great for plastic scintillators.

The PEM covers the region 1.2< $|\eta|$ <2.4. This calorimeter is cylindrical in shape with a conical hole in the center corresponding to an η of 2.4. It consists of 34 layers of lead and gas MWPC's and is located at either end of the CTC. The total thickness is 18-21 radiation lengths (0.6-0.7 absorption lengths). As is the case with all the gas calorimeters at CDF, the most precise energy and position measurement is provided by an etched copper circuit board, segmented in $\eta - \phi$ into cathode pads. The cathode pads all form projective towers that point back to the nominal vertex. The PEM has an energy resolution of

$$\frac{\sigma_E}{E} = \frac{28\%}{\sqrt{E_T}} \oplus 2\% \tag{2.8}$$

(E_T in GeV) with a tower size of $0.09 \times 5°$ in $\eta \times \phi$. Shower positions are measured using information from the θ and ϕ pads resulting in a resolution of 0.2 cm by 0.2 cm.

The PHA covers the region 1.1< $|\eta|$ <2.2. It is situated behind the PEM, forming a partial conical shape. The PHA uses steel plates as absorber, with similar gas proportional chambers as the active medium. The PEM projective geometry and segmentation is preserved. The PHA is 5.7 absorption lengths thick and has an energy resolution of

$$\frac{\sigma_E}{E} = \frac{90\%}{\sqrt{E_T}} \oplus 4\% \tag{2.9}$$

for isolated pions.

The Forward Calorimetry

The forward calorimeters are positioned approximately 6.5 meters from the nominal interaction point, and cover the range 2.2< $|\eta|$ <4.2. Both calorimeters are gas multi-wire proportional chambers.

The forward electromagnetic calorimeter (FEM) [28] consists of 30 layers of 4.5 mm thick lead interleaved with gas sampling chambers and cathode pad readouts giving a total thickness of 25 radiation lengths (0.8 absorption lengths). The projective geometry is extended from the plug region in a grid of approximately 0.1 units in η and 5° in ϕ. The FEM has an energy resolution of

$$\frac{\sigma_E}{E} = \frac{25\%}{\sqrt{E_T}} \oplus 2\% \tag{2.10}$$

with a tower size 0.1 × 5° in $\eta \times \phi$. Shower positions are measured using information from the θ and ϕ pads with a resolution of 0.1-0.4 cm depending upon the location in the calorimeter.

The forward hadronic calorimeter (FHA) [29] consists of 27 layers of 5 cm thick steel interleaved with the gas sampling chambers. The FHA is 7.7 absorption lengths thick and has an energy resolution of

$$\frac{\sigma_E}{E} = \frac{130\%}{\sqrt{E_T}} \oplus 4\% \tag{2.11}$$

for isolated pions.

2.3 Beam-Beam Counters (BBC)

The beam-beam counters consist of two planes of scintillating plastic located 5.8 m from the nominal interaction point. These counters cover the range

$3.24 < |\eta| < 5.9$. Coincident hits in the BBC's at opposite ends of the interaction region are used to define the minimum-bias trigger. The BBC also provides a monitor of the luminosity delivered to CDF.

Chapter 3

Jets Measurement at CDF

To fully analyze high energy physics experimental data, one would like to measure the distribution of final state quarks and gluons. However, owing to the confinement of color charge these are not the final-state particles of the reaction, colorless hadrons are. Since quarks and gluons can not be isolated, they must be studied indirectly. When a quark or gluon recoils energetically from a hard collision, the broken lines of force behind it lead to a jet of hadrons. A typical CDF jet event can be seen in the event picture of figure 3.1.

One of the most difficult aspects of proton-antiproton collider experiment is the enormous total cross section for $\overline{P}P$ interactions. The interaction rate is 10^5 times higher than the CDF data-recording capability. The bulk of the cross section is due to soft processes, called minimum bias events. The more interesting physical processes (such as high E_T jets events) are buried under the soft processes. This requires a sophisticated trigger processor to pick out only events of particular interest. Section 3.1 describes the CDF trigger system with emphasis on the jet triggers used in this analysis.

From studying jets one learns about the initiating quarks or gluons. However, jets are not fundamental degrees of freedom in the theory, so an operational jet definition and reliable methods to calculate their properties are needed. Section 3.2 describes the CDF jet clustering algorithm and the definitions for relevant jet quantities.

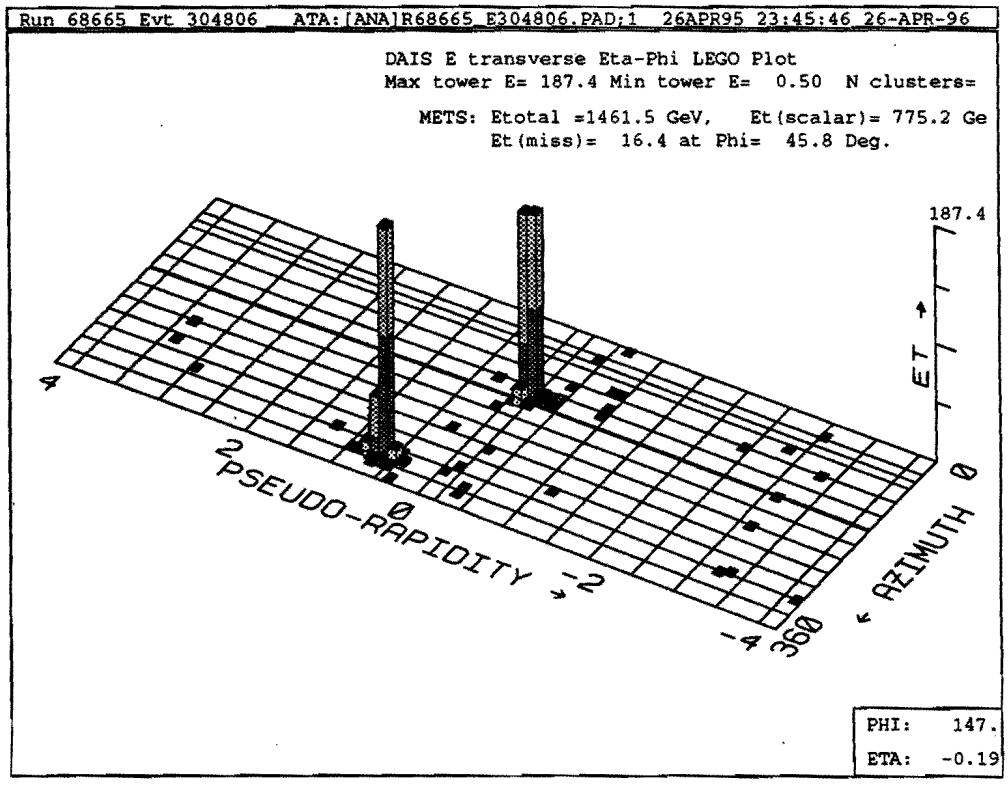

Figure 3.1: A typical dijet event taken during the CDF run 1B. The height of each lego tower shows the amount of energy detected in each section of a detector's calorimeter. The pseudo-rapidity is defined as $\eta = -\ln(\tan\frac{\theta}{2})$, and jets are defined in the (η, ϕ) space.

Due to the limitations of the detector performance and the fundamental elements of the physics process, a huge amount of work needs to be done to understand the jets observed in the calorimeter. Section 3.3 describes the methods used in CDF to correct the jet as closely as possible to the partons initiating the jets.

3.1 CDF Jet triggers

The Tevatron produces roughly 1,000,000 collisions per second; however, the CDF data is stored on magnetic tapes at a maximum rate of only a few events per second. This requires a sophisticated trigger processor to pick out only events of particular interest.

In order to accomplish the event rate reduction, CDF uses a three-level trigger system in which each level reduces the event rate sufficiently to allow a more detailed examination of the interesting events by the next level.

The level 1 trigger makes use of fast analog signals [30] with the decision being made in the 3.5 μs between beam crossings. It therefore incurs no dead-time. The Level 1 trigger system consists of the following main components:

- Coincidence hits in the BBC (Beam-Beam Counter).
- Single calorimeter towers over E_T threshold.
- Muon chamber track stubs over P_T threshold.

The projective geometry in the calorimeters is preserved in the trigger. But to reduce the number of signals to a manageable level, calorimeter towers are summed together to produce logical trigger towers with a width of 0.2 in η

and 15° in ϕ. This maps the detector into an array of 42 (in η) by 24 (in ϕ) in both electromagnetic and hadronic calorimeters. The EM and hadron towers produce separate trigger. The analog calorimeter signals are corrected for pedestal offsets and gain variations in the trigger system.

The trigger tower segments are also weighted by $sin\theta$, where θ is the detector polar angle, so the trigger threshold can be set as the transverse energy in the tower: $E_T = Esin\theta$. No correction is made for possible event variations in the z vertex position. The thresholds used by the two level 1 calorimeter triggers which are used later by some of the level 2 jet triggers are shown in Table 3.1.

Trigger Tower	Threshold (GeV)	
	Low E_t Trigger	High E_t Trigger
West FEM	4.0	51.0
West PEM	4.0	11.0
CEM	4.0	8.0
East PEM	4.0	11.0
East FEM	4.0	51.0
West FHA	51.0	51.0
West PHA	51.0	51.0
CHA	4.0	8.0
East PHA	51.0	51.0
East FHA	51.0	51.0

Table 3.1: Level 1 Jet trigger calorimeter tower threshold.

Level 1 passes events through to Level 2 at a rate of a few kHz. With the added processing time, a much more sophisticated decision can be reached level 2. At Level 2 trigger is able to determine the topology of the event and differentiate crudely between events containing jets, electrons and muons by using the following information from the detector.

- Fast CTC track pattern recognition (CFT) [32].
- Hadronic and Electromagnetic calorimeter clustering.
- Matching CFT tracks to muon hits and calorimeter clusters.
- Global energy sums (Total, Transverse, Missing transverse).

The procedure for finding calorimeter clusters is as follows. Two sets of thresholds "seed" and "shoulder" are applied to all calorimeter trigger towers. The threshold starts at a high value (e.g. 100 GeV) and begins to decrease until one or more calorimeter towers are above the threshold. This application of thresholds results in a map of seed towers. The map is then scanned sequentially in (η, ϕ) space. When a trigger tower is found passing the seed threshold, a cluster is flagged. The four nearest neighbors (the "diagonal" neighbors with different η and different ϕ values are not included) are then checked to see if they pass the low level threshold (e.g. 1 GeV). Then the nearest neighbors of the newly selected towers are checked and so on until no more contiguous towers are found. The process is repeated until no new seed towers exist. At this time the high threshold may be lowered and the process repeated. Once a tower is included in a cluster, it is prohibited from being included in any of the subsequent clusters.

When all towers in a cluster are identified, the cluster is digitized with associated values of E_x, E_y, E_T, η, ϕ, *etc.*. Appropriate analog and digital weighting is performed for the $sin\theta$, $sin\phi$ and $cos\phi$ factors, on a tower by tower basis. Global sums of calorimeter energies such as total energy, total transverse energy, and total missing energy are also available at Level 2. All information produced at Level 2 can be triggered on alone or in conjunction

with any combination of other Level 2 data. Each level 2 jet trigger used in this analysis requires that an event has at least one jet cluster with E_t above threshold and may be prescaled. The Level 2 E_T thresholds and prescale factors are listed in Table 3.2. Additionally, the level 2 jet 20 trigger requires a low E_T threshold level 1 calorimeter trigger, and the level 2 jet 50 trigger requires a high E_T threshold level 1 calorimeter trigger.

Trigger	E_t Cut (GeV)	Prescale Factor
Jet 20	20.0	1000
Jet 50	50.0	50
Jet 70	70.0	8
Jet 100	100.0	1

Table 3.2: Level 2 Jet E_T threshold and prescale factor.

Level 2 requires about 10 μs to make a decision and will reset the front-end electronics if no Level 2 trigger is satisfied. A deadtime of about 5-10% is incurred at this level. The prescale factors are chosen so that level 2 passes events through to Level 3 at a rate of a few Hz.

Level 3 is basically a software filter that has incorporated into it ideas and concepts derived from off-line analysis code. Level 3 has access to the full information from the detector. Thus it is possible to " fine-tune" the event selection process by, for example, employing more accurate clustering techniques and using more precisely reconstructed tracks for better rejection of various backgrounds.

Before executing the level 3 jet filter algorithms, signals due to noise sources such as cosmic rays, high-voltage discharge, neutrons giving large energy deposition in the gas calorimeter, and cable noise pickup were removed. Following

removal of calorimeter noise, clusters are found using the same clustering algorithm used off-line (see Section 3.2). Events are then required to have at least one jet cluster with E_t above some threshold based on the level 2 trigger threshold (see Table 3.3). All Level 3 jet triggers except jet 100 also require corresponding Level 2 jet triggers.

Trigger	Level 3 E_t Threshold
Jet 20	10.0 GeV
Jet 50	35.0 GeV
Jet 70	55.0 GeV
Jet 100	80.0 GeV

Table 3.3: Level 3 Jet E_T threshold.

3.2 Jet Clustering

There are many possible ways of defining jets. In CDF the jet clustering algorithm uses a cone of a fixed radius in (η, ϕ) space to define a jet which corresponds closely to the definitions used in calculating QCD cross sections. Cone algorithms are conceptually very simple to define, as a direction that maximizes the energy flowing through a cone drawn around it. In addition, studies have shown that the cone definition produces a clean separation in the (η, ϕ) metric, and one very nice feature of the cone algorithm is the apparent ease with which energy corrections can be made. This is because they are purely geometrical, so the amount of out-of-cone showering in the calorimeter for example, can be very easily calculated from known detector response and the energy inside the cone.

The jet finding algorithm begins by creating a list of towers above a fixed

where θ is the polar angle of the tower, corrected for the position of the event vertex. The jet position in (η, ϕ) space was determined using the cluster E_T weighted center of mass.

3.3 Jet energy correction

Since jets are a mixture of neutral and charged particles with a variable fragmentation spectrum and their energies are computed by adding up contributions from the EM and hadronic compartments, the calorimeter response to jets is a convolution of the calorimeter response to single particles with the fragmentation function for jets. The energies and momenta defined in Eq. 3.1-3.5 depend only on the energy deposition observed in the calorimeter. These quantities differ from the true partonic values for a variety of reasons. Some of these are due to limitations of the calorimeter performance and others result from fundamental elements of the physics process. The major sources of the difference between their true values and measured ones are given below.

- The calorimeter non-linearity: The calorimeter response to low-energy charged pions exhibits a nonlinearity for momenta below 10 GeV.
- The non-uniform nature of the calorimetry: Particles that shower in boundary regions of the calorimeter will have a smaller energy reported than for regions of uniform response.
- Energy of neutrinos and muons: They deposit either zero or only a small fraction of their energy in the calorimeter.
- Underlying events energy: Energy not associated with the hard- scattering process will be collected within the clustering cone.

- Out-of-cone energy: Transverse spreading of the jet due to fragmentation effects will cause particles to be lost outside the clustering cone, and charged particles with low transverse momenta will be bent outside the cone by the magnetic field.

A correction must be applied to take into account all of these effects. The procedure for generating the correction function has two parts. The first is compensating for known deficiencies in the detector which requires the determination of response of the calorimeter to jets. The second is adjusting for discrepancies between experimentally defined jets and theoretically defined partons which includes corrections for energy escaping the jet cone (out-of-cone addition), and being added by the underlying event (underlying subtraction). The theoretical uncertainties in correcting for detector effects is relatively small, as all the necessary pieces can be determined from jet data. However, the theoretical uncertainties involved in adjusting for out-of-cone loss and underlying event surplus are large and more serious, as the correction of these effects is very model dependent.

3.3.1 Calorimetery response determination

The calorimeter response determination is divided into two stages. First, the relative change in response as a function of jet location in the detector relative to the central region is determined using dijet balancing. Then the absolute response in the central region is determined using Monte Carlo generated events. The parameters in the Monte Carlo are tuned to reproduce the measured response to single particles, and the measured jet fragmentation properties.

Relative Jet correction

The aim is to correct jets back to an equivalent central jet in the η range $0.2 < |\eta| < 0.7$ where measurements were performed using scintillaters with superior resolution. The jets in this η range are sufficiently far from the 90 degree crack and the 30 degree crack, and the non-linear response is well understood [33, 34].

To measure the relative response of the detectors at large pseudorapidity, jet P_T balancing is used. Events are selected by requiring that there be two and only two jets with $P_T > 15$ GeV. To avoid trigger biases, the average jet transverse momentum $\bar{P}_T$ must be at least 5 GeV above the trigger threshold. Each jet in an event is then labeled either "trigger", meaning it is contained in the central region ($0.2 < |\eta| < 0.7$), or "probe", meaning it can be anywhere in η. If both jets fall in the central region, a random assignment of trigger and probe is made. Events with no jet in the central region are excluded from the study.

The balancing is performed using the missing E_T projection function (MPF),

$$MPF = \frac{\not{E}_{T_x} P_x{}^{probe} / P_T{}^{probe} + \not{E}_{T_y} P_y{}^{probe} / P_T{}^{probe}}{(P_T{}^{probe} + P_T{}^{trigger})/2}. \tag{3.6}$$

The component of $\not{E}_T$ along the probe jet is measured by MPF. Apart from the soft gluon radiation which gives the dijet system a small transverse boost, MPF should be zero if the correct relative energy scale is used. A systematic P_T unbalance in the calorimeter indicates an energy scale difference between the central region and the probe jet region. By using the $\not{E}_T$ of the event, rather than the P_T imbalance of the jets, the effects of any transverse boost of the system are minimized. The MPF is measured as a function of the η of the probe jet for five bins of $\sum P_T$. The correction factor is defined as

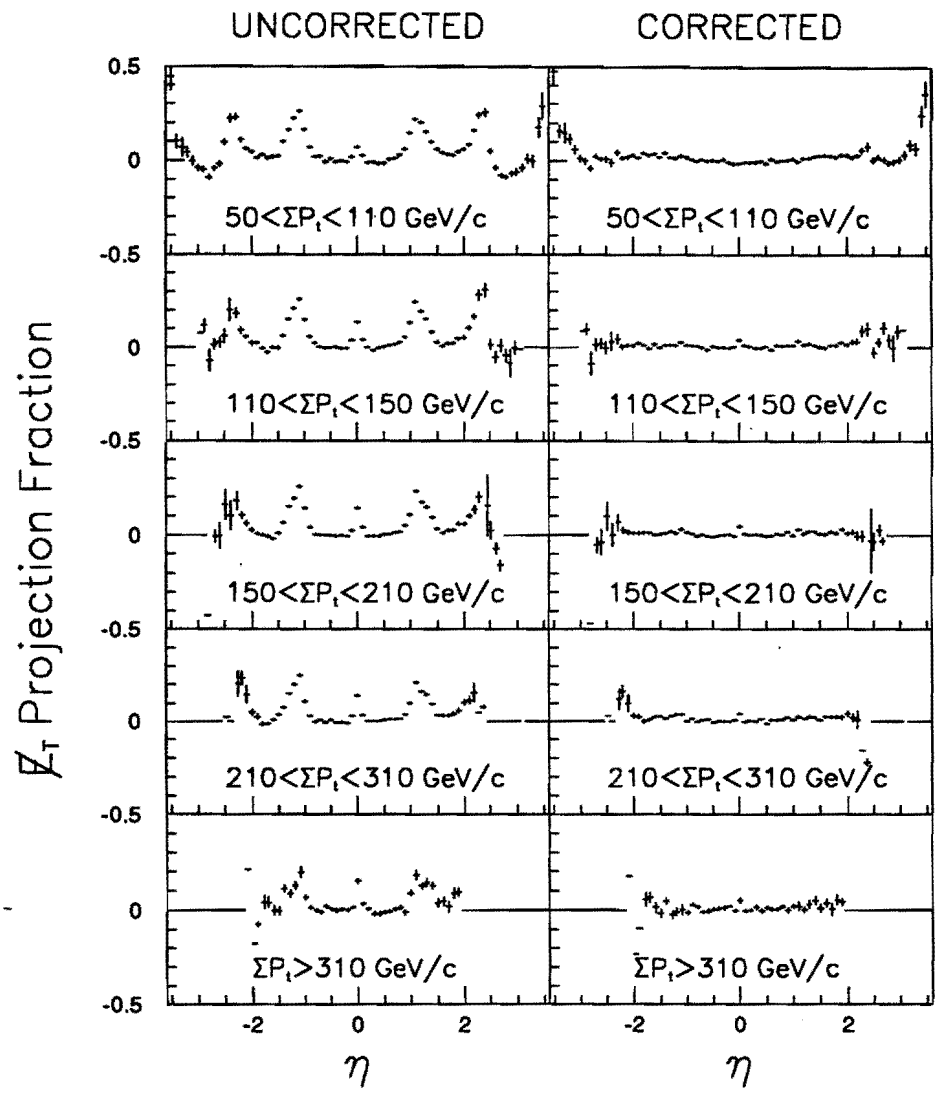

Figure 3.2: The jet balancing variable, missing E_T projection function MPF, is plotted as a function of η before and after the jet energy corrections for five bins of $\sum E_T$. The η's of the structures in the uncorrected plot correspond to the boundaries between the different calorimeters.

$< P_t^{trigger}/P_t^{probe} >$. This way the effect of the transverse boost cancels on the average. A correction function can be derived from the above information to correct the energy of each jet based on the η and P_T of the jet. Fig. 3.2 shows the MPF as a function of η before and after the relative jet energy correction function has been applied for five $\sum P_T$ for the Run 1B jet trigger events. After the jet energy corrections, the relative energy scales are equal at the (1-2)% level for all five bins of $\sum E_T$.

Absolute Jet correction

Because the η dependence of the jet response was determined from data, there was no need to measure the absolute jet response as a function of η. Consequently, the absolute scale was only determined for central jets. To be consistent with the relative scale analysis presented above, a central jet was defined by $0.2 < |\eta_{detecter}| < 0.7$.

The measured jet energy is distorted due to effects such as the non-linear response of the hadron calorimeter, which is caused by the non-linear low-energy response of the calorimeter to single hadrons. The jet energy measured in the calorimeter is a convolution of the single-particle response with the jet fragmentation function. So the observed jet energy is a function not only of the incident parton energy but also of the momentum spectrum of the particles produced in the fragmentation process.

The correction algorithm was derived using Monte Carlo simulation of both the fragmentation process and the CDF detector. It is important that Monte Carlo events used in jet studies reproduce both the observed fragmentation and the observed response of the calorimeter to charged hadrons. The response of the calorimeter to hadrons was determined from test beam data and isolated

tracks in the central tracking chamber. The jet fragmentation spectrum was also measured using central charged tracks. The Monte Carlo simulation incorporated both calorimeter response and tuned Field-Feynman [35] jet fragmentation to reproduce the observed jet fragmentation properties, and was used to determine detector response to central jets. Jets were clustered using the standard CDF algorithm, and cluster P_t was then compared to the magnitude of the vector sum of all particles whose initial direction was within the corresponding jet cone P_t^{cor}.

Even though the response of the calorimeter is linear for photons and electrons, the EM energy scale still needs to be corrected for scintillator aging in the EM calorimeter during the runs. The shift of EM energy scale is investigated by using the standard dielectron Z database [36], comparing the raw dielectron mass distribution from the data in Run 0 (88-89), Run 1A (92-93), and Run 1B (94-96). Figure 3.3 shows that dielectron mass spectrum for the three runs overlaid with Gaussian fits. The means of the Gaussian fits are 93.8 GeV/c^2, 89.8 GeV/c^2, and 89.4 GeV/c^2 ,respectively, for the three runs. Since all corrections are made relative to Run 0, the Run 1A correction is +0.045 and the Run 1B correction is +0.049.

3.3.2 Underlying Event correction

The underlying event refers to a collection of relatively low P_t particles not associate with the jet: This includes particles arising from interactions between spectator partons from the same interaction and particles from other possible interactions in the same event. These particles can contribute a small amount of additional energy within the jet cone. The underlying event correction depends on the luminosity of the run and the cone size. For Run 1B the luminosity

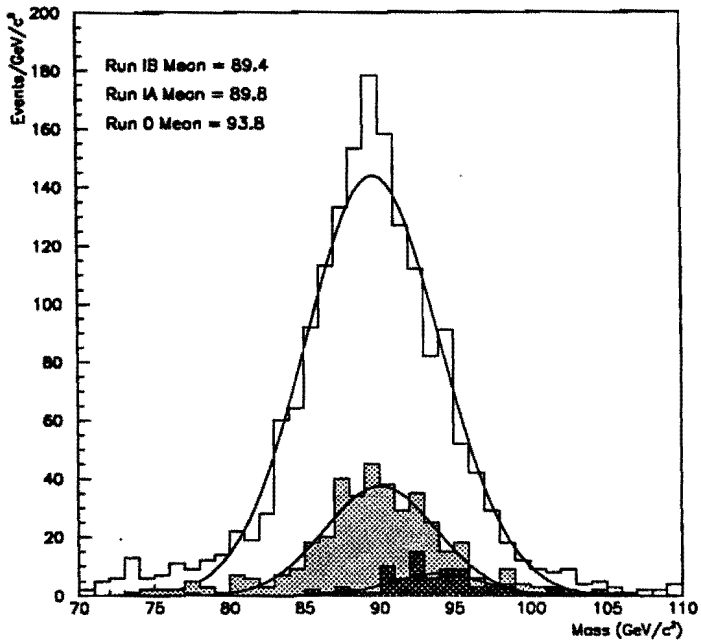

Figure 3.3: The dielectron mass distribution for Run 0 (cross hatched), the Run 1A (shaded), and Run 1B, showing the shift between the three runs

is much higher than Run 1A, so the effects of the multiple underlying event correction on the jet energy is more important, especially for the low energy and large cone size jets. The underlying event correction includes the effects of multiple interactions run. For a cone of size R = 0.7 an average P_T of 2.21 GeV or 3.29 GeV will be contributed from the underlying event for run 1A and run 1B respectively.

3.3.3 Out of cone correction

The nature of the fragmentation process generally results in some fraction of the fragmentation products falling outside the cone. The magnitude of the

vector sum P_t of the particles falling outside a cone was determined with the Monte Carlo simulation program used to determine the jets absolute energy scale. The out of cone energy for cone size of R = 0.7 was well described by the relation,

$$OUTCONE = 8.382\ (1 - 0.846\ e^{-0.00728\ P_t}). \tag{3.7}$$

In a real jet event, it is impossible to unambiguously associate specific jets with initiating partons. However, this is precisely the information required to make an out-of-cone correction. Consequently, a theoretical model of jet particle production must be used to determine the amount of energy/momentum lost out-of-cone. Therefore, the correction is very model dependent and has large uncertainties.

In this analysis, the estimated amount of energy falling outside the cone was added to the jet energy.

Chapter 4

Measurement

4.1 Data Set

The data set used in this analysis is from Tevatron Run 1A (1992-1993) and Run 1B (1994-1996) using four single jet triggers, which have yielded total 106 pb^{-1} of data. The jet triggers used have been described in chapter 3. For run 1A, jet ntuples on disk were used which contain clustered jets (cone size 0.7) and level 2 jet triggers information for the five highest E_T jets. For Run 1B split stream B pad data stored on 8mm tapes was used to produce similar jet ntuples. To limit the introduction of the duplicate events, only these files listed for a given tape in the production manager were used. But there are still some event duplications in the jet ntuples which were removed by the analysis code. The events were also required to pass cosmic ray filter COSFLT, which was used in HATFLT mode. In this mode COSFLT rejects the events which have 6 GeV or more out of time energy. Cosmic ray events which fall into the interaction time gate are not removed by this filter program, these in-time background events were removed in the analysis program. The COSFLT cut is summarized in table 4.1.

4.2 Dijet Event Selection

When processing the ntuples we select events that are good for non-muon analyses [37] and are required to pass the following cuts.

Trigger	Tested	Accepted	Fraction
Jet 20	555502	554136	99.75%
Jet 50	357421	317622	88.87%
Jet 70	388241	301976	77.78%
Jet 100	2200050	1751950	79.63%

Table 4.1: Cosmic ray filter (COSFLT) cut summary

- Vertex cut: $|Z_{vertex}| < 60$ cm
- Missing E_T significance cut: $\not{E}_T/\sqrt{\sum E_T} < 6.0$
- Junk Event cut: $\sum E_T < 2$ TeV and $\sum E < 2$ TeV
- Forward Jets cut: $|\eta_{1,2}| < 2.0$ and $|\cos\theta^*| < 2/3$

Each of these cuts will be discussed below.

Vertex Cut

The Z vertex position of the events in the final event sample is required to be within 60 cm of the mean interaction point to keep the projective geometry of the CDF detector.

In principle, the Z-vertex cut efficiency should be independent of the trigger type of the events used to measured it, but it may be a little biased because of the non-uniformity, and different online energy scales of the calorimeters. In this analysis, we measured the cut efficiency using the events from the level 2 jet trigger. The Z vertex cut efficiencies for these jet triggers are given in table 4.2 for Run 1A and Run 1B respectively.

Level 2	Tested		Passed		Efficiency	
Trigger	Run 1A	Run 1B	Run 1A	Run 1B	Run 1A	Run 1B
Jet 20	255383	517695	241155	476210	94.4%	92.0%
Jet 50	113550	301029	106588	275057	93.9%	91.4%
Jet 70	106383	281633	99914	259995	93.9%	92.3%
Jet 100	93230	333913	87733	308473	94.1%	92.4%
Total	568546	1434270	535390	1319735	94.2%	92.0%

Table 4.2: Z_{vertex} cut efficiency for various QCD triggers

Junk Event Cuts

The COSFLT filter has already cut a lot junk events produced by cosmic rays, main ring splash, and other detector background; but there is still some remaining. This remaining background is rejected by requiring the missing E_T significance to be less than 6.0, and that both the $\sum E_T$ and total energy deposited in the calorimeter be less than 2 TeV. The generic jet events are expected to have no missing E_T except that introduced due to mismeasurement of the jets or from neutrinos from semi-leptonic decay of heavy quarks.

Forward Jet Cuts

The dijet is defined to be the two jets with the largest corrected E_T in the event. In order to get more reliable measurements, both jets are required to be in the central region of the detector with a pseudorapidity cut $|\eta_d| < 2.0$. A cut on scattering angle in the dijet center of mass frame $|\cos\theta^*| < 2/3$ provides a more uniform acceptance as a function of mass and reduces the QCD background which peaks at $|\cos\theta^*| = 1$.

These cuts define the detector acceptance, but the data is not corrected for these cuts, instead the same cuts are applied to the theory predictions.

All the jets in the event are then corrected using JTC96X [38]. The corrections include the calorimeter response including degradation of the EM calorimeter over the run, energy outside the clustering cone, and underlying event including multiple interactions on average over the run. The control input parameter to JTC96X was CODE='YY', ERROR='DD', OFFVER=5(7) for run 1A(1B).

4.3 Trigger Efficiency

The efficiencies of the Run 1A and Run 1B jet triggers were measured by looking at lower jet triggers and asking how often the higher E_T level 2 cluster passed the level 2 E_T threshold. For example, to measure the efficiency of the jet 70 trigger, we go to the jet 50 trigger and make two plots: the rate as a function of fully corrected dijet mass and the same plot with the requirement that the level 2 E_T is greater than 70 GeV. The ratio of the latter plot divided by the former is the efficiency of the level 2 jet 70 trigger as shown in Fig. 4.3.

For the jet 20 trigger there is no lower threshold trigger to measure the efficiency with, so we pick a a lower mass threshold that is safely 100% efficient ($M > 180$ GeV/c^2). For the sake of completeness the jet 20 trigger efficiency is estimated by using a self-checking method [39]. At mass threshold of 180 GeV/c^2 the estimate of the jet 20 trigger efficiency is 100%.

At level 2, the E_T was calculated assuming that the primary interaction took place at Z = 0.0 as opposed to actual vertex position. This leads to smearing in the effective E_T threshold. However the level 3 triggers were essentially fully efficient because they required the corresponding level 2 trigger and had an E_T threshold that was set significantly lower than level 2 threshold.

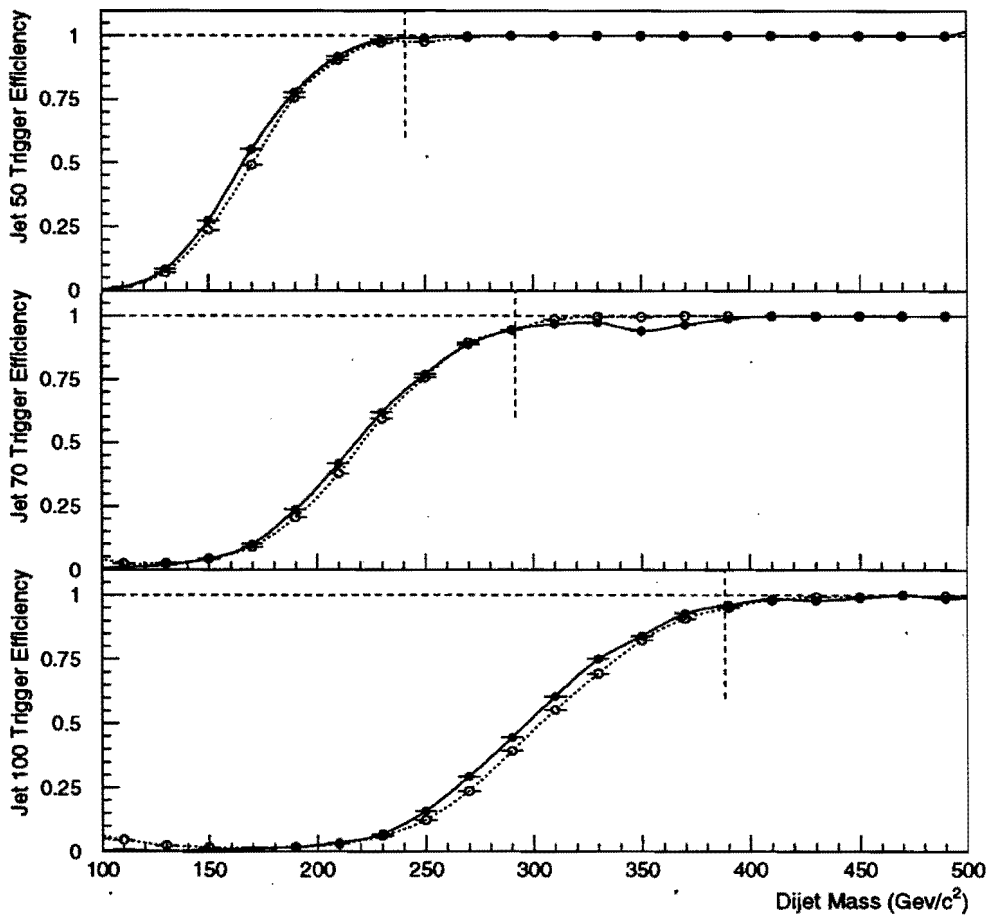

Figure 4.1: The Run 1A (closed circle, solid line) and 1B (open circle, dotted line) efficiency for the Jet 50 Trigger (top), Jet 70 Trigger (middle) and Jet 100 Trigger (bottom) as a function of dijet mass and smooth fits. The dashed lines indicate mass cuts for this analysis.

The efficiency plots as a function of fully corrected dijet mass are presented in Fig. 4.3. Data is used from the trigger begin at the mass in Fig. 4.3 marked with a dotted line and ending where the next trigger begins. The values of the mass cuts chosen and the the efficiency at those cuts are displayed in table 4.3. The value of the cut is chosen to be reasonably efficient and to correspond to our mass bin edges, which were chosen apriori so that each bin was roughly equal to the measured dijet mass resolution at the central value of the mass bin.

4.3.1 Trig Efficiency vs. χ

To correct the dijet angular distribution for the trigger efficiency, the trigger efficiency as a function of the angular variable χ is needed. Since the trigger cuts in jet E_T, for a given mass bin the trigger is expected to be less efficient at the lowest values of $\sin\theta^* \approx 2E_t/m$, corresponding to the highest values of $\cos\theta^*$ and χ. The trigger efficiency vs. χ is calculated in the same way as described in section 4.3, but plotted vs. χ in bins of dijet mass. In Fig. 4.3.1 the trigger efficiency vs. χ behaves as expected, falling off gradually at higher χ.

4.4 Luminosity

For both Run 1A and Run 1B the luminosity was determined using a program LUM_CONTROL, and summing the luminosity of runs that were good for "non-muon" analyses. The luminosity used by this analysis is listed in table 4.3.

For Run 1B, the luminosity was multiplied by 0.987 to correct for accidentals. This brings the total luminosity correction to the "standard" value of .903

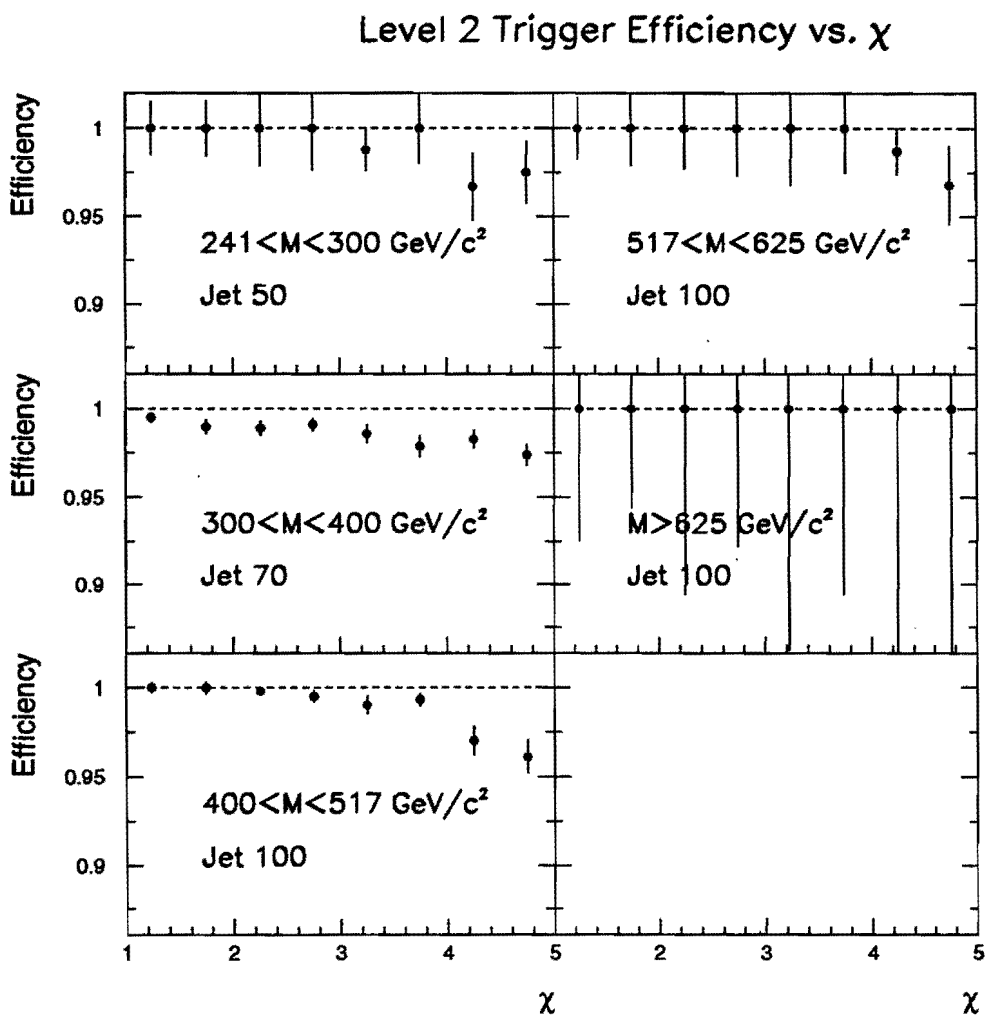

Figure 4.2: Jet trigger efficiencies as a function of angular variable χ for five different mass regions.

Level 2	Mass Cut (GeV)	Efficiency		Lum/Prescale (pb^{-1})	
		Run 1A	Run 1B	Run 1A	Run 1B
Jet 20	180	~1.00	1.00	19.1/500	87.3/1000
Jet 50	241	0.99	0.98	13.1/20	87.3/40
Jet 70	292	0.95	0.96	19.1/6	87.3/8
Jet 100	388	0.97	0.96	19.1/1	87.3/1

Table 4.3: Level 2 triggers, mass cuts, efficiency at threshold and luminosity divided by prescale factors.

used in Run 1A, which is the combined correction for both accidentals and the new measurement of the beam-beam counter (BBC) cross section. For run 1A LUM_CONTROL was also used, but for that run [55] LUM_CONTROL did not correct for the new BBC cross section or accidentals, so the full correction factor of 0.903 was used.

Chapter 5

Search for New Particles Decaying into Dijets

Many classes of new particles have a larger branching fraction into two partons (quarks and gluons) than into modes containing a lepton or electroweak gauge boson. However this channel (dijets) is difficult because of the large QCD background and the poor mass resolution. However, high statistics in the dijet sample allow exclusions of new particles with their cross sections that are a small fraction of the dijet cross section. Also, the poor dijet mass resolution can be turned to our advantage, allowing us to search for many different phenomena with a single dijet mass resolution function.

In this chapter, the dijet mass resolution function is presented in section 5.1. Sections 5.2 and 5.3 focus on the Monte Carlo simulation of the QCD background and the dijet mass resolution function of new particle production in the CDF detector. Section 5.4 will discuss the significance of observed fluctuations in the dijet mass distribution. The next two sections (section 5.5 and section 5.6) will describe and illustrate the method used to determine the limits for new particle production. Section 5.7 covers the discussion of the systematic uncertainties. The final section of this chapter (section 5.8) concludes with a summary of limits for new particle production set by this analysis.

5.1 The Measured Dijet Mass Distribution and Background Fit

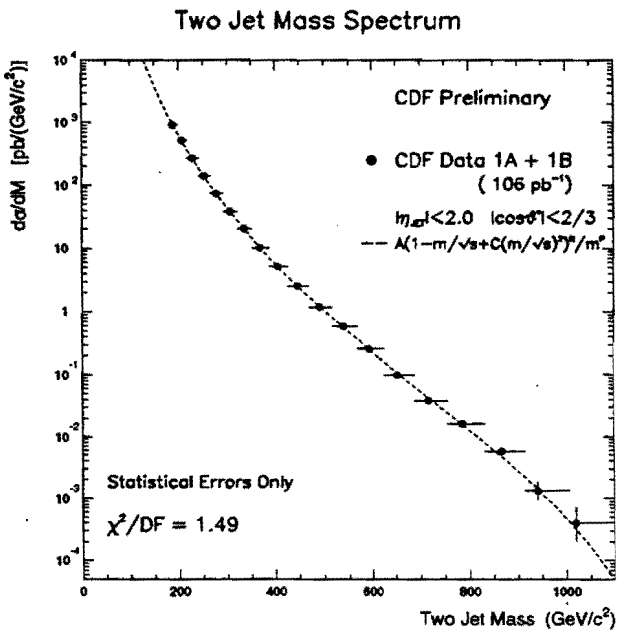

Figure 5.1: The dijet mass distribution (points) compared to a smooth background fit (dashed curve).

The dijet mass distribution, after correcting for the acceptance of the Z-vertex cut and the trigger efficiency, is shown in Fig 5.1. The bin widths are roughly equal to the dijet mass resolution at each energy, and the points are plotted at the mean mass value of the data in the bin. The error bars, which are mostly too small to see, are Poisson statistical uncertainties. The data has been fit to a smooth parameterization of the form:

$$d\sigma/dm = A(1 - m/\sqrt{s} + c(m/\sqrt{s})^2)^N/m^p, \tag{5.1}$$

where A, c, p and N are parameters. Here the $1/m^p$ term imitates the QCD matrix element and the $(1 - m/\sqrt{s} + c(m/\sqrt{s})^2)^N$ term imitates the parton

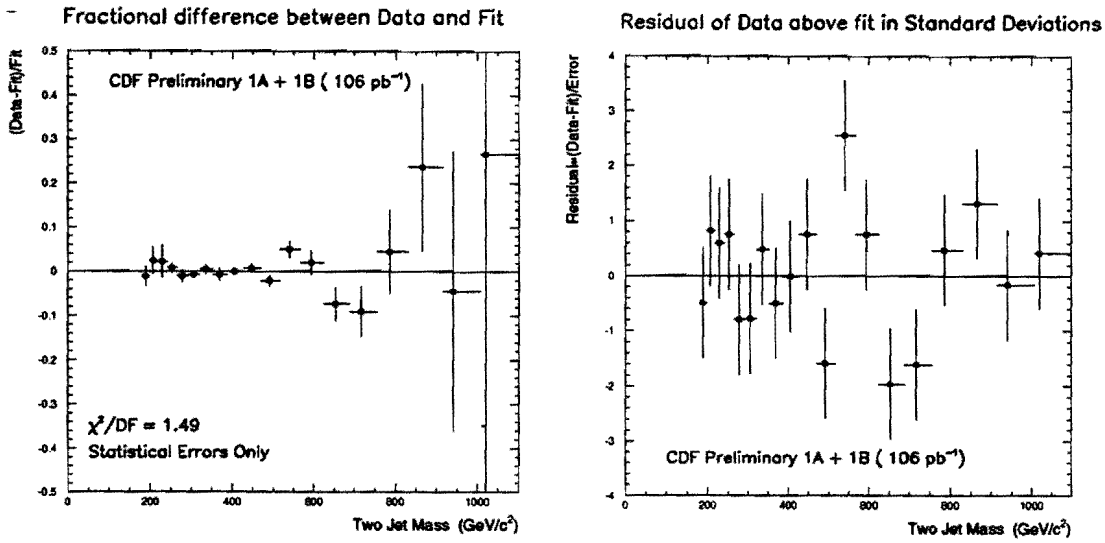

Figure 5.2: Left) The fractional difference between the dijet mass differential cross section and a smooth background fit. Right) The residuals between the dijet mass differential cross section and a fit to a smooth background parameterization. The residuals are in units of Gaussian standard deviations, as is the error bar.

distribution falloff at high $x \sim m/\sqrt{s}$. Clearly this parameterization is motivated by simple lowest order QCD. The χ^2 per degree of freedom is 1.49 for 18 degrees of freedom, corresponding to a probability of only 10%. The statistical power of the data is best illustrated by (Data - Fit)/Fit in Fig. 5.2, and the quality of fit is best illustrated by the residuals (Data - Fit)/Error in Fig. 5.2.

In this analysis the measured dijet mass spectrum begins at 180 GeV/c^2. Although jet 20 trigger efficiency is very high down to 124 GeV/c^2, the data in the region $124 < M < 180$ GeV/c^2 is not very well understood. If the fit is extended to lower dijet mass, a fluctuation appears near 200 GeV/c^2. It might be new physics, but could also be an artifact of the low energy jet corrections, which are more sensitive to run dependent underlying event corrections, or the inability of the parameterization to accommodate the true shape of the background, or some other unknown threshold effect. From the point of view

of searching for new particles away from our threshold, the threshold at 180 GeV/c^2 is chosen for its reasonably low χ^2/df for the background fit.

5.2 QCD background simulations

5.2.1 Event Generation

The Monte Carlo program used to generate QCD jet events is PYTHIA [41]. In this analysis, the string inspired matrix elements and CTEQ2L parton distributions [42] are used. No higher-order processes are explicitly included, nor any higher-order loop corrections to the $2 \rightarrow 2$ processes. However, by initial-and final-state QCD radiation, multijet events are being generated. The fragmentation processes in PYTHIA is modeled by the Lund string model [43]. In this model, the string break-up process is assumed to proceed until only on-mass-shell hadrons remain, each meson corresponding to a small piece of string with a quark in one end and an antiquark in the other.

5.2.2 QFL Detector Simulation

The response of the CDF detector to final-state particles generated by the Monte Carlo is simulated using QFL [44], which is a fast simulation of the CDF detector. This simulation is fast mainly because it parameterizes the detector response rather than deriving it from first principle. For electrons and photons, an electromagnetic shower model is used to simulate the energy deposition in the calorimeters and strip chambers. For hadrons, an hadronic shower model is used to simulate the energy deposition in the hadronic calorimeters. The simulation models used by QFL have several parameters which have been carefully tuned to match the CDF testbeam data, and have been shown to

do a good job of simulating the detector's response to leptons, photons, and hadrons.

QFL produces higher level analysis banks rather than raw data, thus eliminating the need to run the complete reconstruction on the simulation output. QFL output can be used as input for various CDF offline codes. Jets are reconstructed from towers using CDF jet clustering algorithms. This enables the sample of Monte Carlo events to be processed as real data, except that the jet energy corrections are specifically designed for QFL to reflect difference between events from the real detector and those from QFL.

5.2.3 Comparison of Data and QCD Simulation

In order to get a mass distribution over a wide range in mass with reasonable statistics, multiple generator mass thresholds were used in the QCD jet events simulation. Table 5.1 listed the details of the simulation.

Generator Mass Cut (GeV/c^2)	Generated Events (Million)	Saved Mass Cut (GeV/c^2)	Plotted Mass Range (GeV/c^2)	Plotted Events	Number of Bins
50	0.24	100	—	—	-
70	0.50	130	—	—	-
90	0.79	163	180-265	5030	4
150	0.83	241	265-470	7931	6
250	1.44	388	470-568	4071	2
325	3.19	450	568-832	11859	4
500	0.98	700	832-1108	1625	3

Table 5.1: For each generator level mass cut, the events generated and simulated, the dijet mass cut for saving events in the ntuple, the dijet mass range plotted, the number of simulated events plotted, and the number of mass bins.

In Fig. 5.3 and Table 5.2, data is compared to the QCD prediction using

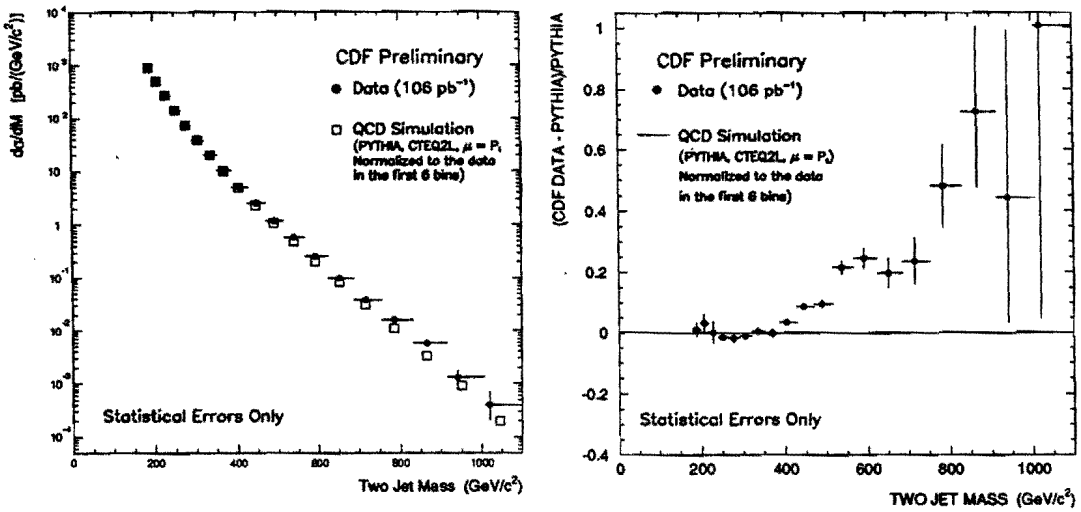

Figure 5.3: Left: The dijet mass distribution (circles) compared to QCD predictions (boxes). The QCD predictions are normalized to the data points in the first 6 bins. Right: The fractional difference between the dijet mass distribution (points) and a QCD simulation normalized to the data in the first 6 bins.

Mass Bin (GeV/c^2)	Mean Mass (GeV/c^2)	1A+1B Events	1A+1B Xsec ($pb/GeV/c^2$)	Stat. Error ($pb/GeV/c^2$)	QCD Sim. ($pb/GeV/c^2$)	B kgr. Fit ($pb/GeV/c^2$)
180-198	188.2	1942	9.2024e+2	2.0883e+1	9.1059e+2	9.3048e+2
198-217	206.6	1165	5.2300e+2	1.5323e+1	5.0694e+2	5.1047e+2
217-241	228.1	771	2.7402e+2	9.8683e+0	2.7363e+2	2.6810e+2
241-265	251.9	8813	1.4055e+2	1.4972e+0	1.4256e+2	1.3942e+2
265-292	276.9	5229	7.3293E+1	1.0136e+0	7.4631e+1	7.4097e+1
292-321	305.1	14093	3.8110e+1	0.3210e+0	3.8493e+1	3.8358e+1
321-353	335.2	8299	2.0101e+1	0.2207e+0	2.0004e+1	1.9995e+1
353-388	368.7	4599	1.0137e+1	0.1495e+0	1.0150e+1	1.0211e+1
388-427	405.4	19283	5.1329e+0	0.3697e-1	4.9592e+0	5.1333e+0
427-470	445.9	10723	2.5411e+0	0.2454e-1	2.3388e+0	2.5225e+0
470-517	490.6	5502	1.1822e+0	0.1594e-1	1.0793e+0	1.2074e+0
517-568	539.5	2973	0.5887e+0	0.1080e-1	0.4840e+0	0.5611e+0
568-625	592.8	1452	0.2573e+0	0.6751e-2	0.2063e+0	0.2522e+0
625-688	652.3	614	0.9842e-1	0.3972e-2	0.8218e-1	0.1062e+0
688-756	716.8	258	0.3816e-1	0.2385e-2	0.3099e-1	0.4215e-1
756-832	786.8	121	0.1608e-1	0.1462e-2	0.1087e-1	0.1538e-1
832-915	867.0	47	0.5719e-2	0.8341e-3	0.3314e-2	0.4622e-2
915-1007	941.3	12	0.1317e-2	0.3803e-3	0.9129e-3	0.1378e-2
1007-1108	1020.0	4	0.4000e-3	0.2000e-3	0.1993e-3	0.3157e-3

Table 5.2: For each mass bin in the analysis, the mean corrected dijet mass, the number of events in run 1A + run 1B, the combined differential cross section, it's Gaussian statistical error (same as Poisson except for last 3 bins), a QCD simulation (normalized to the data in the first 6 bins by dividing the simulation by 0.65), and the background from the fit to the data are listed.

PYTHIA and QFL. The simulation is normalized to the first 6 data points by dividing the simulation by a factor of 0.65. The left figure shows the comparison of data and QCD predictions on a logarithmic scale, and the right one shows the fractional difference between the simulation and the data on a linear scale. These figures show there is an excess in the data at the high mass end, similar to what is seen in the inclusive jet cross section from run 1A [45].

Clearly, the difference between the data and the simulation is quite significant. As for the high E_t excess in the inclusive jets [45], hypotheses for the origins of this difference range from the mundane suggestion of an unknown experimental systematic, to the possible solution of a larger than expected gluon distribution of the proton, to many exotic suggestions of new physics.

5.3 Dijet Mass resonance line shape from New Particle Production

New particles with a natural width significantly smaller than the measured dijet mass resolution should all appear as a dijet mass resonance of the same line shape in the CDF detector, so the mass resonance line shape of the signal only needs to be modeled for a single type of new particle decaying to dijets. When a new particle is produced and decays, QCD radiation off the initial and final state partons gives rise to additional jets, which smear the meaning of the basic processes and worsen the dijet mass resolution. The processes being searched for in this analysis are mainly $qq \rightarrow X \rightarrow qq$ and $qg \rightarrow X \rightarrow qg$. The process $gg \rightarrow X \rightarrow gg$ is only a small component of the ρ_T signal.

In this analysis the line shape of a new particle signal in the CDF detector is parameterized using the PYTHIA Monte Carlo and QFL detector simulation

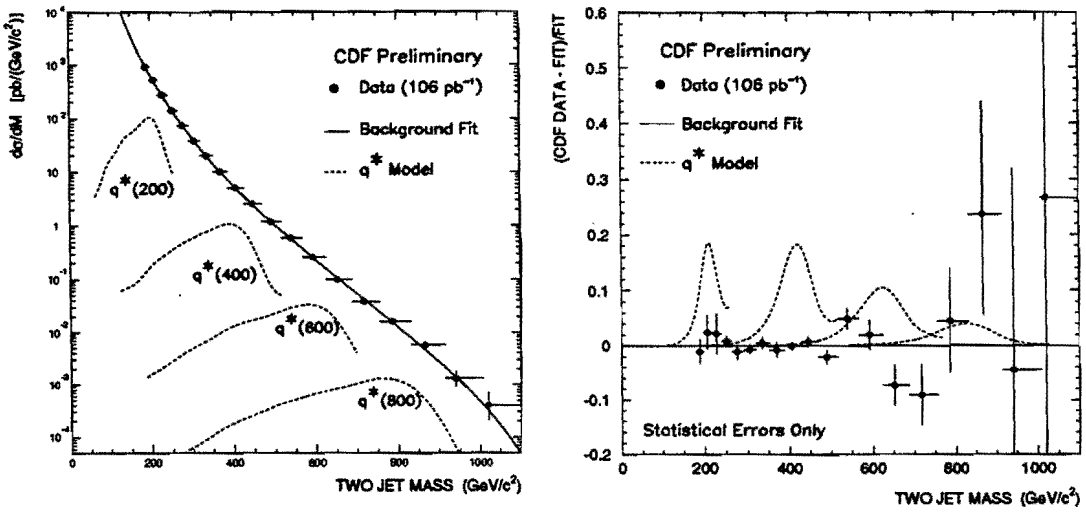

Figure 5.4: Left) The dijet mass distribution (points) and fit to a smooth parameterization (solid curve). Also shown simulation of an excited quark signal in the CDF detector (dashed curves). Right) The fractional difference between the dijet mass distribution (points) and a smooth background fit (solid line). Also shown is a simulation of excited quark signals in the CDF detector (dashed curves)

for the $qg \rightarrow Q^* \rightarrow qg$ process. The dijet mass line shape has a Gaussian core from jet energy resolution and a long tail toward low mass resulting from QCD radiation. Fig. 5.4 shows the simulation of an excited quark signal for excited quarks of mass 200, 400, 600, and 800GeV/c^2 in CDF detector on a logarithmic scale (left figure) and the fractional difference between the dijet mass distribution and background on a linear scale (right figure). The figure shows a signal will show up in at least 2 and as many as 4 mass bins.

5.4 Search for New Particles

There are upward fluctuations appearing in the data near 200, 550 and 850 GeV/c^2. Although these effects are likely statistical fluctuations, this is a search for new particles, so the possibility that they are real effects due to new

physics will be investigated in the following sections.

5.4.1 Significance of Observed fluctuations

For the purpose of searching for a resonance, the fit to the data using the parameterization presented previously in equation 5.1 is used as background.

In the 200 GeV mass region ($198 < M < 241$ GeV/c^2), there are 1936 events with an expected background of 1918 $\pm$ 44 events from the straight background fit without signal. This corresponds to 0.4 σ effect. The probability that the estimated background has fluctuated up to greater than the number of events seen in this mass region is about 34.1%. In the 550 GeV mass region ($517 < M < 625$ GeV/c^2), there are 4425 events with an expected background of 4254 $\pm$ 65 events from the background fit. It is about 2.6 σ effect, which corresponds to a probability of 0.44%. In the 850 GeV mass region ($756 < M < 1007$ GeV/c^2), there are 180 events with an expected background 167 $\pm$ 13 events. It is about a 1 σ effect, with a corresponding probability of 15.7%.

Currently, the probability of seeing a background fluctuation is not sufficiently small to claim that new particle production has been found in any of these mass regions.

5.4.2 Search unusual features

Fig. 5.5 and Fig. 5.6 show 8 different variables separately to check whether the 550 GeV "feature" and the high mass excess have any unusual features. Their distributions are compared in the three mass regions: $400 < M < 517$ GeV/c^2 indicated by a solid histogram, $517 < M < 625$ GeV/c^2 indicated by points with errors, and $M > 625$ GeV/c^2 indicated by a dashed histogram (errors on

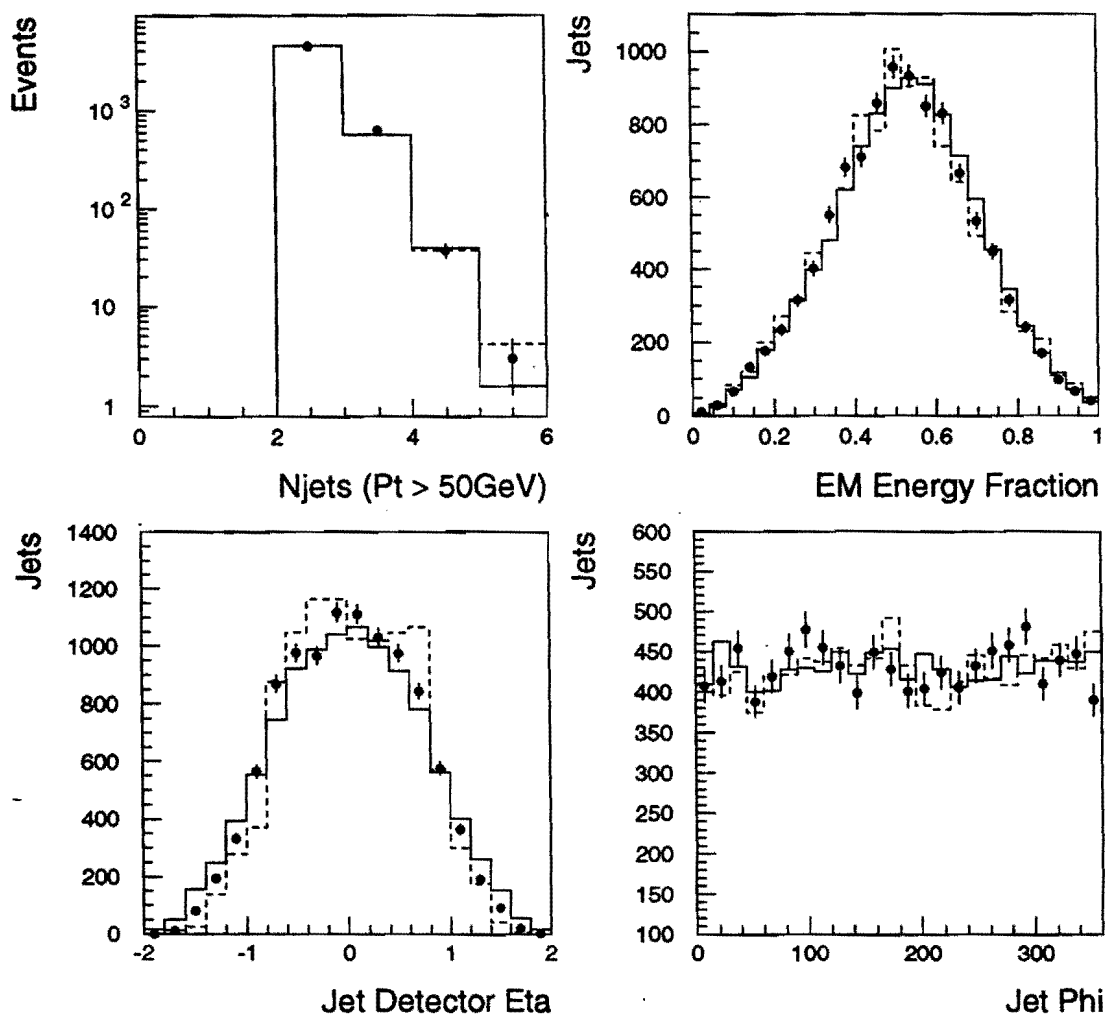

Figure 5.5: The jet multiplicity, EM Fraction, Detector η and ϕ distributions for events or leading jets with $400 < M < 517$ GeV/c^2 (solid hist), $517 < M < 625$ GeV/c^2 (points), and $M > 625$ GeV/c^2 (dashed hist). The histograms are normalized to the sum of the points.

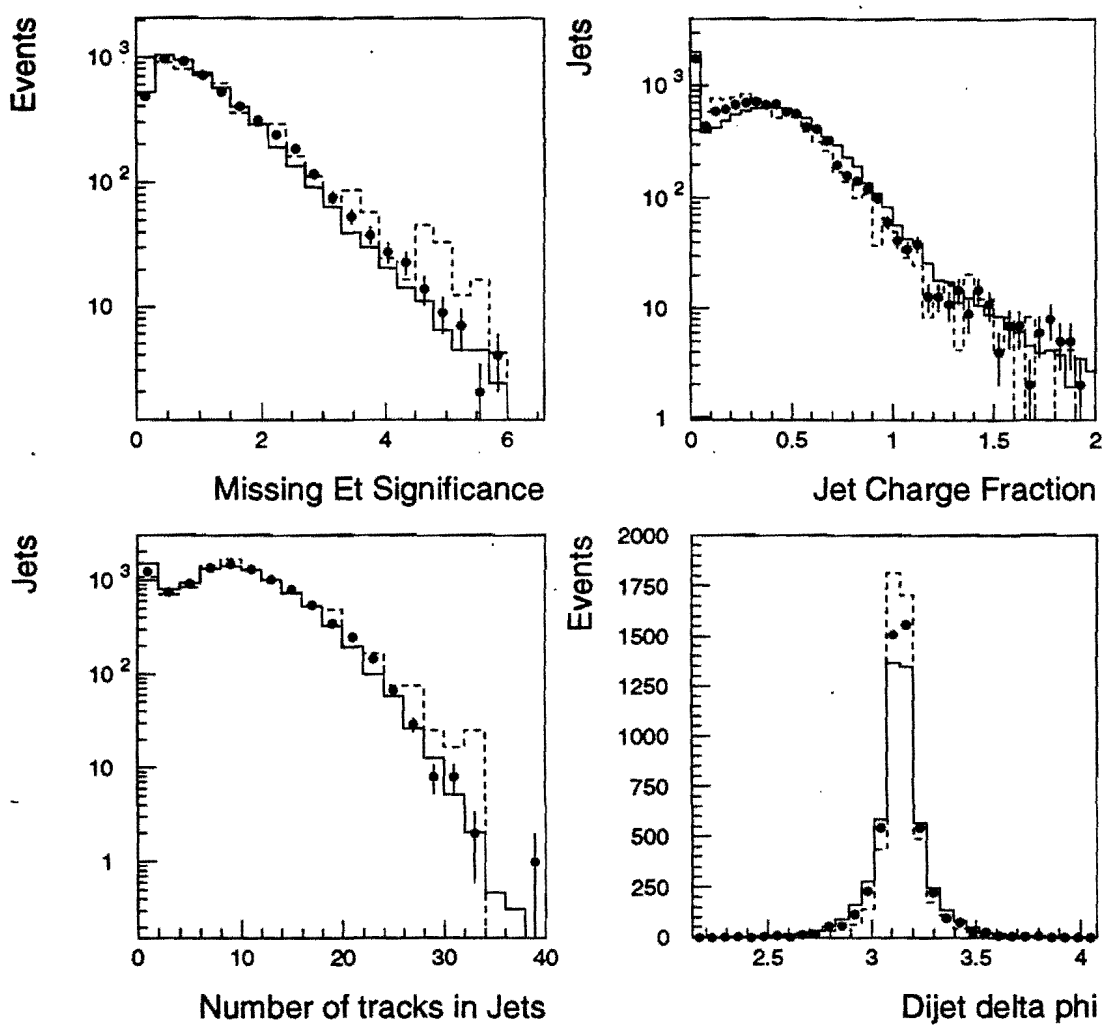

Figure 5.6: The missing E_T, jet charge fraction, track multiplicity and jet mass for events or leading jets with $400 < M < 517$ GeV/c^2 (solid hist), $517 < M < 625$ GeV/c^2 (points), and $M > 625$ GeV/c^2 (dashed hist). The histograms are normalized to the sum of the points.

this region are roughly twice as big as the errors on the points). In all the plots, the low mass region and high mass region are both normalized to the entries in the $517 < M < 625$ GeV/c^2 region. In those plots where the vertical axis is "jets", both leading jets of the dijet are plotted.

In Fig. 5.5, the jet multiplicity distributions (from 2 to 5) are the same in the three mass regions within statistics (the 5 jet bin has only a single event for the high mass region). The EM energy fraction of jets in the 3 mass regions is also virtually identical, eliminating the possibility that high mass effect is due to photons or detector noise in EM or HAD sections separately. The jet detector η distributions are also quite similar within statistics, given that the errors on the dashed histogram are twice those on the points. It is possible that a slightly larger correction for the 90 degree crack would be appropriate for the highest mass jets, but such a small correction would not produce a noticeable change in the angular or mass distributions. The jet ϕ distributions also do not show any significant effects, but it is possible that the small fluctuations near 90 and 270 degrees represent a residual contamination of main ring splash or cosmic rays at the level of 1% of the total rate in the $517 < M < 625$ GeV/c^2 region. However, the distributions for jets with ϕ of 90 and 270 degrees show no indication of an enhancement of main ring splash or cosmic rays: they have good distributions of jet EM fraction, jet charge fraction, missing Et significance, number of tracks per jet, etc.

In Fig. 5.6, the rise in the missing E_t significance in the $M > 625$ GeV/c^2 region may indicate that there is a 1% residual contamination of cosmic rays or main ring splash, or perhaps the distribution is just slowly evolving as dijet mass goes higher: in either case, this is an acceptable amount of possible contamination, given that the statistics in this region are poor. In Fig. 5.6, the

jet charge fraction and track multiplicity for the three mass regions is roughly the same. Finally, the dijet $\Delta\phi$ distribution shows the back-to-back ϕ location of the two leading jets. It is expected that this distribution should be narrower for the higher mass dijet events.

There appears to be nothing unusual about the events in the mass regions of the 550 GeV/c^2 fluctuation or the high mass excess.

5.5 Determination of the New Particle Production Limits

Using the measured dijet mass spectrum, limits can be set on the amount of new particle production that can be present in the data. A 95% confidence limit on the cross section for producing new particles, times the branching ratio into dijets, was determined using a binned maximum likelihood method.

To set a limit on the cross section for new particle production as a function of particle mass, the number of events observed in the data are assumed to come from a mass resonance signal sitting on a large QCD background. The signal differential cross section at mass m for a new particle of mass M^*, is calculated using the excited quark line shape discussed in the previous section and the cross section normalization from the theory for the new particle. This gives the predicted signal events in the i_{th} mass bin: $N_i(q^*$ signal). The QCD background is given by the parameterization in Eq. 5.1. This gives the predicted QCD background events in the i_{th} mass bin: N_i(QCD background). The total predicted number of events in the i_{th} mass bin μ_i is then given by adding the predicted signal, normalized by an unknown factor α, and the QCD background events. That is:

$$\mu_i = \alpha N_i(\text{ signal}) + N_i(\text{QCD background}). \tag{5.2}$$

The probability P_i of observing n_i events when μ_i are predicted is given by Poisson statistics

$$P_i = \frac{\mu_i^{n_i} e^{-\mu_i}}{n_i!}. \tag{5.3}$$

The likelihood for seeing the observation, L, is the product of P_i over all bins in the mass spectrum. That is:

$$L = \prod_i P_i. \tag{5.4}$$

For each value of new particle mass M^*, from 200 GeV/c^2 to 1150 GeV/c^2 in 50 GeV/c^2 steps, the best fit value of the q^* normalization parameter α, and the background parameters of Eq. 5.1 (A, c, p, N) is found by minimizing $-\ln L$. Next, by varying α with the background parameters A, c, p and N held constant, the 95% confidence upper limit can be determined by finding the value of α_{95} such that

$$\frac{\int_0^{\alpha_{95}} L(\alpha)d\alpha}{\int_0^{\infty} L(\alpha)d\alpha} = 0.95. \tag{5.5}$$

Multiplying the total expected cross section for the new particle of mass M^* by α_{95} gives the 95% confidence upper limit on the cross section for new particle production and decay.

Results of the fit are presented in Table 5.3.

Mass (GeV)	A×10^{-15} (pb/GeV)	p	N	C	Signal (pb)	Error (pb)	95% CL (pb)
200.	11.428	5.655	4.966	-0.296	3529.626	1049.712	12766.905
250.	19.006	5.755	4.587	-0.356	98.687	306.406	756.048
300.	30.893	5.853	4.144	-0.434	0.005	16.501	76.717
350.	31.232	5.856	4.101	-0.450	0.661	7.451	37.549
400.	24.851	5.808	4.377	-0.380	0.028	7.006	16.055
450.	24.680	5.807	4.367	-0.388	0.276	1.405	15.170
500.	17.607	5.726	5.124	-0.225	10.174	3.686	30.628
550.	17.727	5.730	4.983	-0.280	7.682	2.436	21.036
600.	20.918	5.772	4.561	-0.363	1.231	1.710	8.303
650.	19.307	5.755	4.664	-0.329	0.002	0.508	2.916
700.	27.495	5.828	4.270	-0.403	0.002	0.191	1.294
750.	22.212	5.783	4.549	-0.340	0.000	0.236	0.859
800.	26.398	5.819	4.330	-0.395	0.001	0.396	0.840
850.	25.696	5.814	4.370	-0.376	0.004	0.201	0.933
900.	25.774	5.816	4.294	-0.409	0.000	0.134	0.947
950.	23.927	5.802	4.346	-0.405	0.076	0.152	0.735
1000.	24.103	5.803	4.351	-0.403	0.064	0.163	0.561
1050.	27.356	5.828	4.256	-0.412	0.000	0.029	0.409
1100.	28.777	5.839	4.188	-0.430	0.000	0.053	0.305
1150.	33.654	5.871	4.025	-0.465	0.000	0.041	0.118

Table 5.3: Results from the fit. As a function of new particle mass, the amplitude A and C and powers p and N of the background function $(A(1-M/\sqrt{S}+C(M/\sqrt{S})^2)^N/M^p)$ are listed, the mean cross section of the new particle signal, its statistical uncertainty, the 95% confidence level upper limit including systematic uncertainties.

5.6 Fit to background + new particle signal

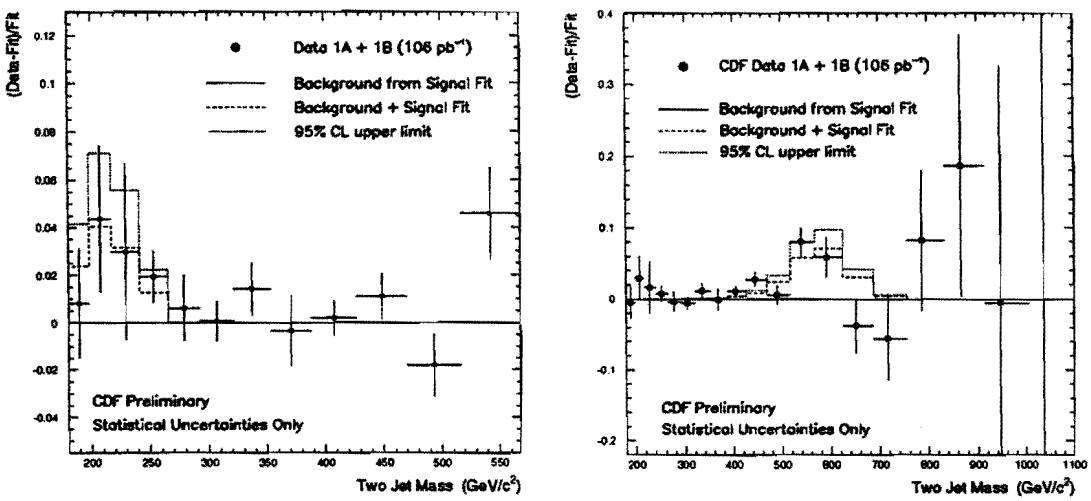

Figure 5.7: The fractional difference between data and the background from a fit to background plus a resonance (points), and compared to the fractional difference between best fit from a fit to background plus 200 GeV/c^2 (Left) and 550 GeV/c^2 (Right) resonance (dashed line) and the same background. Also shown is the 95% C.L. upper limit on resonance (dotted line).

Figure 5.7 is an illustration of the method used to set limits on the search for mass resonances. It shows the fractional difference between data and the background from a fit to background plus a resonance, and compares to the fractional differences between the best fit to a background plus 200 GeV/c^2 and 550 GeV/c^2 resonance and the same background. The most statistically significant fluctuation in the data occurs at 200 GeV/c^2, which has a signal of 3529.6 ± 1049.7 picobarns (3.4 σ). Note that the 95% CL upper limit (dotted hist) is above all of the points in the region of this peak. In the 550 GeV/c^2 mass region the data favors a new particle signal of 7.682 ± 2.436 picobarns (3.2 σ), but the shape of the data does not look like a mass resonance because the next two data points are too low.

5.7 Systematic Uncertainties

This section first describes the method that was used to include the systematic uncertainties in the limits calculation, and then discusses each of the systematics and concludes with a summary.

5.7.1 Procedure for Including Systematics

The method for including systematic uncertainties in the new particle production limits calculation is similar to that used for previous CDF analysis [47, 48, 49, 55].

Each source of systematic uncertainty is estimated by varying the uncertainty by 1σ, and redoing the fit for new particle production. The effect of each systematic uncertainty on the limit is expressed as an uncertainty on the 95% CL limit in the signal normalization parameter ($\Delta\alpha$) at each value of new particle mass. Once the uncertainty on α is known for each systematic, the total systematic uncertainty $\Delta\alpha_{TOT}$ is generated by adding all sources of systematic uncertainties in quadrature.

Given the total systematic uncertainty on α, $\Delta\alpha_{TOT}$, a new likelihood function is formed by smearing the old likelihood function with a Gaussian whose sigma is $\Delta\alpha_{TOT}$:

$$L'(\alpha) = \int_0^\infty L(x) \frac{1}{\sqrt{2\pi}\,\Delta\alpha_{TOT}} e^{-\frac{1}{2}(\frac{\alpha - x}{\Delta\alpha_{TOT}})^2} dx. \tag{5.6}$$

Then the 95% CL upper limit is determined using the new likelihood distributions that includes systematic uncertainties. The convolution smears out the probability distribution and therefore increases the 95% limit by moving

more probability from low α to high α.

5.7.2 Estimates of Systematic Uncertainties

There are several sources of systematic uncertainties in the limits calculation. In the following paragraphs the systematics are discussed in decreasing order of importance. In all cases where there is both a positive and a negative systematic uncertainty: the largest one is taken as the systematic uncertainty.

Uncertainty in Absolute Jet Energy Scale

The systematic uncertainty on the central jet energy scale for a cone size $R = 0.7$ was $^{+4.5\%}_{-3.8\%}$ ($^{+2.6\%}_{-1.6\%}$) for $E_T = 25(300)$ GeV jets in the 1988-89 run [50]. Also, there is an additional 2.5% systematic associated with the relative calibration of the run 1A and 1988-89 energy scales [51], and an additional 1% systematic associated with the relative calibration of the run 1B and run 1A energy scale [52]. Combining these uncertainties in quadrature gives a systematic uncertainty of $^{+5.2\%}_{-4.7\%}$ ($^{+3.7\%}_{-3.1\%}$) for $E_T = 25(300)$ GeV jets in run 1A+1B.

A mass independent systematic uncertainty of $\pm 5\%$ was used in this analysis. The effect on limits was estimated by moving the mass position of the dijet resonance up and down by 5% and redoing the fits and corresponding limits. The systematic uncertainty on the limit coming from the uncertainty on the absolute jet energy scale, shown by open circles in Fig. 5.8, is very mass dependent and varies from 10% to 225%.

Uncertainty Introduced by Low Mass Data

As discussed in section 5.1, there is a fluctuation near 200 GeV/c^2 when low mass data is included in the analysis. Since it is not clear whether the effect is caused by the presence of a mass resonance, or an artifact caused by jet energy corrections, this is included in the systematic uncertainties. The effect on limits was estimated by comparing the default limits and the ones from including the low mass data ($150 < M < 180$ GeV/c^2). In Fig. 5.8 the solid squares show the resulting percent change in the limit as a function of new particle mass. The largest effect is at low mass, and the mass dependent systematic varies from 5% to 160%.

Uncertainty in Background Parameterization

In order to estimate the systematic uncertainty introduced by the background parameterization, the default parameterization in equation 5.1 was changed to $d\sigma/dm = A(1 - m/\sqrt{s})^N/m^p$. The difference between the two was taken as a 1σ systematic, which was highly mass dependent varying from 2% to 95%, as shown by the solid triangles (downward pointing) in Fig. 5.8.

Uncertainty in Jet Energy Resolution

The systematic uncertainty in the Gaussian jet energy resolution is quoted as 10% [53]. To incorporate this systematic the fits were redone for the data sample with the Gaussian cores of the dijet mass resolution widened or narrowed by 10%. This 1σ systematic gives a mass dependent uncertainty from 1% to 90%, as shown by the open diamonds in Fig. 5.8.

Uncertainty between Run 1B and Run 1A energy scales

A difference between the Run 1B and Run 1A energy scales can cause a shift within a mass resonance in the data, distorting its shape and potentially hiding the resonance. The Run 1B cross section is roughly 5% less than the Run 1A cross section, which could correspond to an energy scale shift of 1%. To account for the possibility that there is a 1% difference, the the energy scale in Run 1B have been shifted up by 1% before combining with Run 1A data. This shift gives a mass dependent systematic between 1% and 80%, shown by the solid triangles (upward pointing) in Fig. 5.8.

Uncertainty in Relative Jet Energy Scale vs. η

The jet correction routine JTC96X sets the relative scale using dijet balancing in both Run 1A and Run 1B data, and provides a relative energy scale error from the upper and lower statistical bounds (a curve vs. E_t) [54]. To incorporate this systematic uncertainty the data are corrected using both the low bound and the high bound and again fit for resonances. Here the systematic is applied to the data, instead of to the mass resonance theory. This 1σ uncertainty gives a mass dependent systematic from 1% to 75%, as shown by the open boxes in Fig. 5.8.

Uncertainty in Trigger Efficiency

The statistical uncertainty on each bin of the trigger efficiency is roughly 2% in the turn-on region. A systematic uncertainty of $\pm 2\%$ was used for trigger efficiency effects. The effect on limits was estimated by moving the trigger efficiency up and down by 2% and redoing the fits and corresponding limits.

This gives a very mass dependent systematic varying from 10% to 70%, as shown by the open stars in Fig. 5.8.

Uncertainty in Radiation Effects

When a new particle is produced and decays, QCD radiation off the initial and final state partons contributes to a long tail to low mass which distorts the otherwise Gaussian dijet mass resolution. The effect was discussed in the run 1A analysis [55], and here the same estimates of the systematic uncertainty in radiation are used, although the fits are redone with the entire run 1A and 1B data sample. The systematic is relatively flat with mass at roughly 5% to 40% on the cross section limit, as shown by the open triangles in Fig. 5.8.

Uncertainty in Luminosity and Efficiency

The official luminosity uncertainty of 3.6% was used. The Z vertex cut is 94% (93%) efficient in Run 1A (1B), and it's systematic uncertainty is of order 1% and entirely negligible. The jet finding efficiency is essentially 100% for jets from a 200 GeV new particle. The η and $\cos\theta^*$ cuts are not corrected for in the data, but are incorporated in the lowest order cross section calculations.

Table 6.3 summarizes the systematic uncertainties used to smear the original likelihood functions. The individual uncertainties are added in quadrature to obtain a total uncertainty on α. The total uncertainty is very mass dependent varying from 35% to 305%, as shown by solid circles in Fig. 5.8.

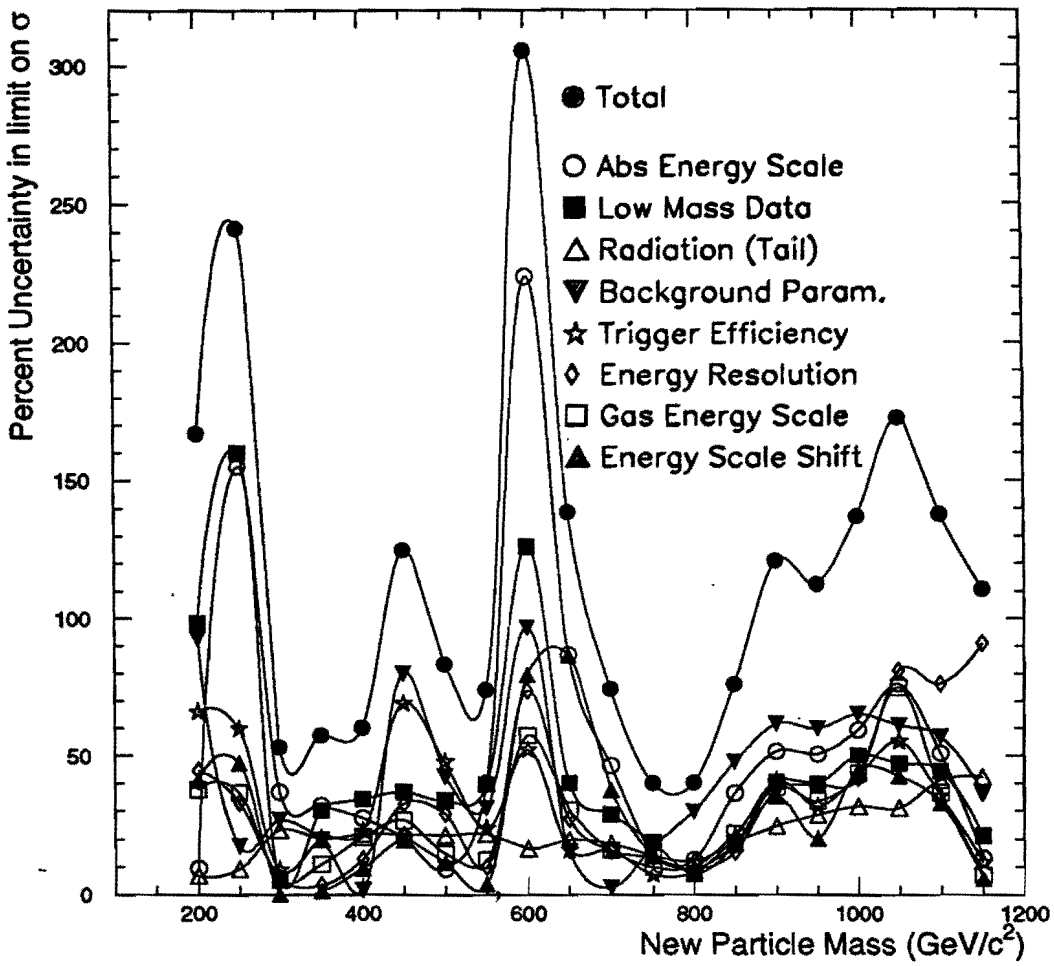

Figure 5.8: The systematic uncertainty in the cross section limit as a function of new particle mass resulting from the uncertainty in absolute central jet energy scale (open circles), including data with mass lower than 180 GeV/c^2 (solid squares), radiation's effect on the mass resolution (open triangles), the parameterization of the QCD background (solid down triangles), the jet trigger efficiency (open stars), the jet energy resolution (open diamonds), jet energy scale relative to the central (open boxes), and a possible shift in the run 1B energy scale compared to run 1A (solid up triangles). Not shown is a systematic uncertainty on the luminosity (3.6%) and efficiency (1%). These uncertainties are summed in quadrature to obtain the total uncertainty (closed circles).

Table 5.4: Systematic Uncertainty.

Source	Systematic	Effect on Xsec limit
Absolute Energy Scale	±5% in mass	10% – 220%
Low Mass Data	Low mass-High mass	10% – 160%
Background Parameter	added parameter	2% – 95%
Jet Energy Resolution	10% of RMS	5% – 90%
Trigger Efficiency	2% in efficiency	5% – 80%
Energy Scale Shift	1B-1A cross section	1% – 75%
Relative Energy Scale	Dijet balance stst.	1% – 70%
Radiation	w/wo radiation	5% – 40%
Luminosity	3.6% in Luminosity	1%
Total		35% – 305%

5.8 Limits on New Particle Production

5.8.1 Limits on New Particle Productions without Systematics

Fig. 5.9 shows the preliminary 95% confidence upper limit on the cross section times branching ratio vs. new particle mass. The cross section limit contains only statistical uncertainties. Also shown in Fig. 5.9 is the theoretical predictions for axigluons, technirhos, excited quarks, new gauge bosons (W', Z') and E_6 diquarks. The new particle production is excluded at a 95% confidence level in the mass ranges where it is above the limit curve. The limits are summarized in Table 6.3. Notice that the excited quarks have the steepest slope because they require a gluon in the initial state, and that the objects produced directly via strong interactions have the largest cross sections.

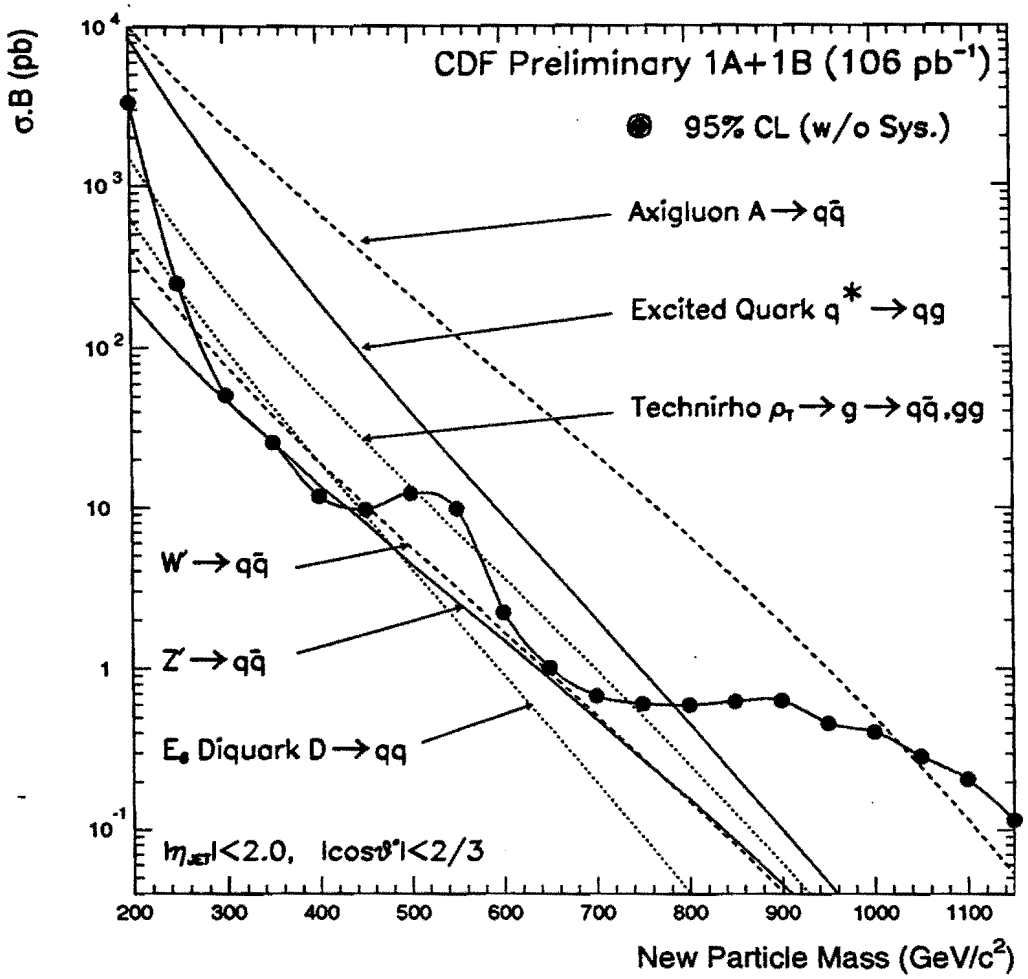

Figure 5.9: The 95% confidence level upper limit on the cross section times branching ratio for new particles decaying to dijets vs. new particle mass (points) is compared to the theoretical prediction for the cross section for axigluons, excited quarks, technirhos, new gauge bosons (W' and Z'), and E_6 diquarks. The cross section limit contains statistical uncertainties only.

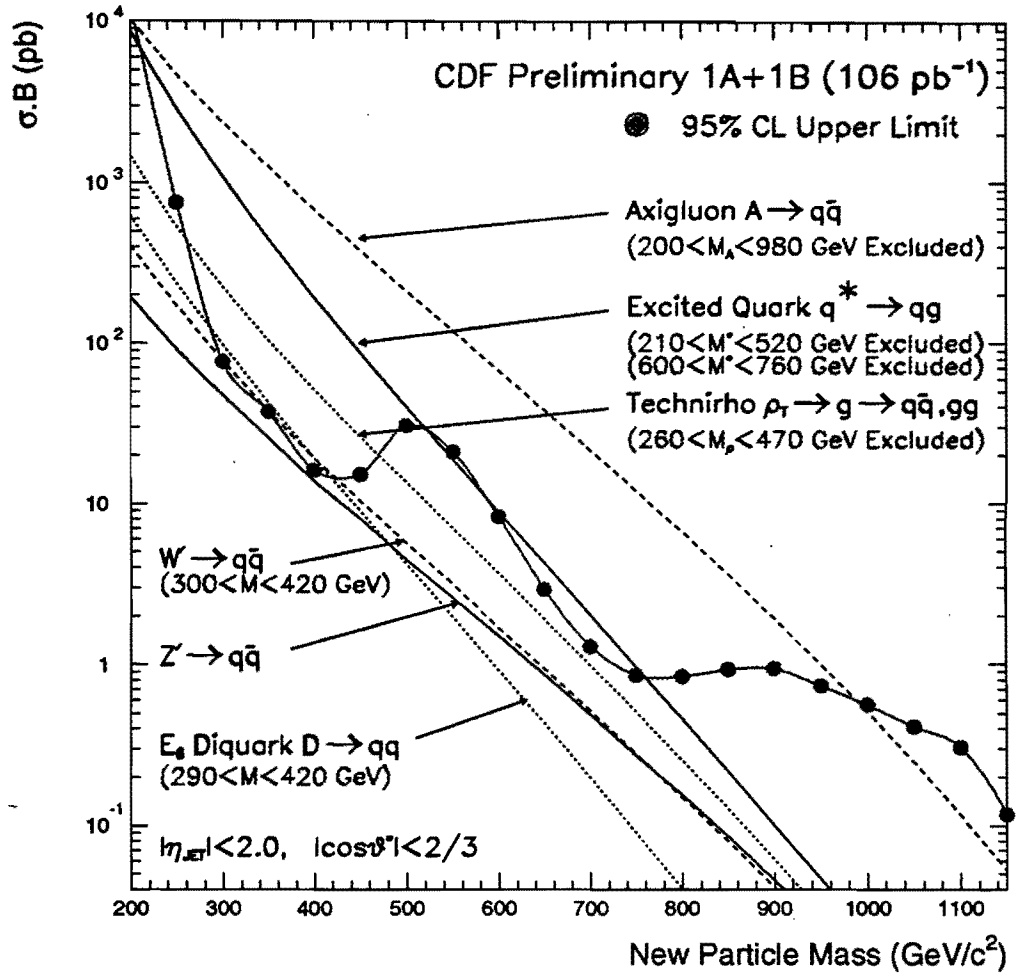

Figure 5.10: The 95% confidence level upper limit on the cross section times branching ratio for new particles decaying to dijets vs. new particle mass (points) is compared to the theoretical prediction for the cross section for axigluons, excited quarks, technirhos, new gauge bosons (W' and Z'), and E_6 diquarks. The cross section limit contains both statistical and systematic uncertainties.

5.8.2 Effect of Systematic Uncertainties on the Limit

Following the procedure outlined in Section 5.7.1, the 95% CL limits with systematics are found from the solid curves in Fig. 5.10. As the statistical precision of the data has increased, the systematics have become more important. The actual limits on new particles before and after systematic uncertainties are summarized in Table 5.5.

Limits on Axigluons

The 95% C.L. limit for the axigluons decaying to standard model quarks is $200 < M_A < 1020$ GeV/c^2 with statistic uncertainty only, and $200 < M_A < 980$ GeV/c^2 with systematic uncertainties. This extends CDF previous exclusions of $200 < M_A < 930$ GeV/c^2 from run 1A [47].

Limits on Excited Quarks

The 95% C.L. limit for the excited quarks is $200 < M < 780$ GeV/c^2 with statistic uncertainty only, and $210 < M < 520$ and $600 < M < 760$ GeV/c^2 with systematic uncertainties, extending the previous CDF exclusion of $80 < M^* < 570$ GeV/c^2 from run 1A [47]. Since the excited quark cross section depends on the coupling, so the mass limit is sensitive to its strength. Figure 5.11 shows the regions excluded at 95% CL in the coupling vs. mass plane.

Limits on Technirhos

The 95% C.L. limit for technirhos is $220 < M_\rho < 500$ and $580 < M_\rho < 740$ GeV/c^2 with statistic uncertainty only, and $260 < M < 470$ GeV/c^2 with systematic uncertainties. This extends CDF previous exclusions of $320 < M_\rho <$

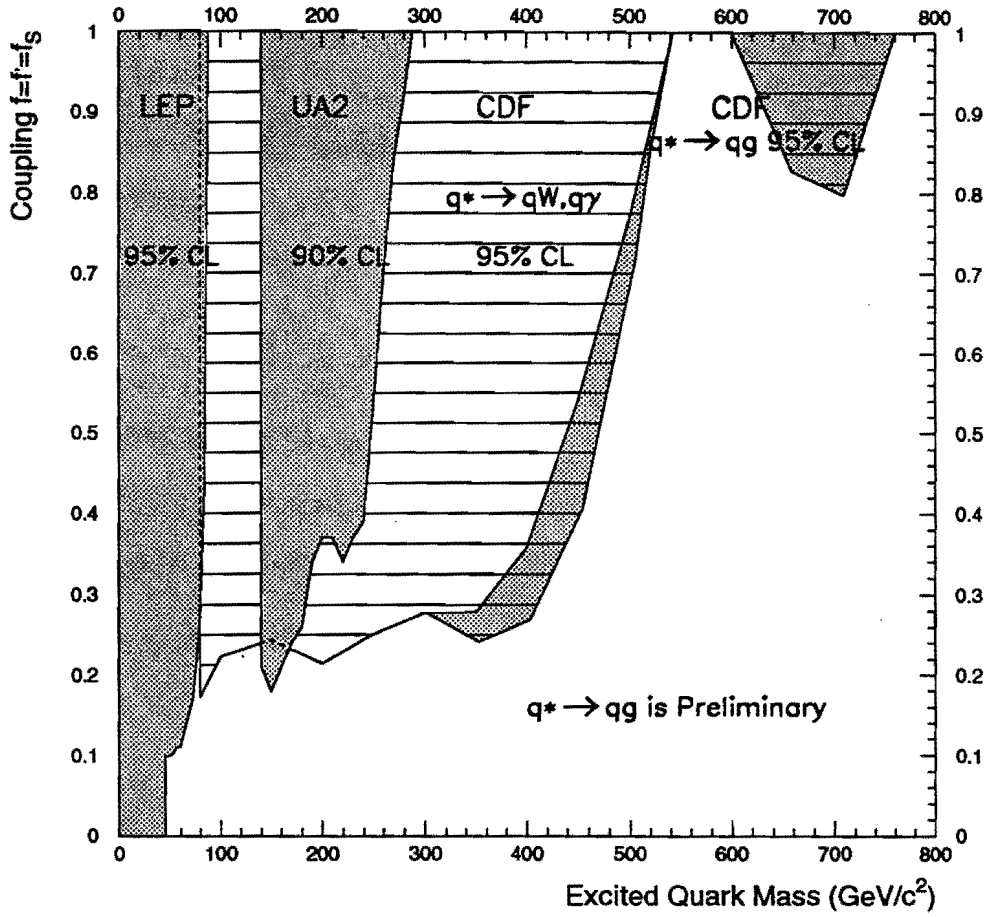

Figure 5.11: The region of the coupling vs. mass plane excluded by previous CDF measurements in the $q^* \to q\gamma$ and $q^* \to qW$ channels in run 1A (hatched region) is extended by this search in the $q^* \to qg$ channel in run 1A + 1B (shaded and hatched region). The CDF excluded regions are compared to the regions excluded by LEP [56] in the $q^* \to q\gamma, qg$ channels (shaded region) and the region excluded by UA2 [57] in the $q^* \to qg$ channel (shaded).

480 GeV/c^2 from run 1A [47].

Limits on New Gauge Bosons

The 95% C.L. limit for W′ is $270 < M_{W'} < 460$ GeV/c^2 with statistic uncertainty only, and $300 < M_{W'} < 420$ GeV/c^2 with systematic uncertainties. Although this is not as good as the current CDF limit on the W' in the electron channel [58] (652 GeV) it is important to check in as many channels as possible in case the relative couplings are different than expected.

The cross section for Z' was too small to exclude.

Limits on E_6 diquarks

The 95% C.L. limit for E_6 diquarks is $250 < M_{E6} < 440$ GeV/c^2 with statistic uncertainty only, and $290 < M_{E6} < 420$ GeV/c^2 with systematic uncertainties. This is the first exclusion of this particle, since at Tevatron energy it is produced by the interaction of a valence quark and a sea quark, thus reducing the production rate to very low level.

Table 5.5: Limits on new particle production.

New Particle	Limits (GeV/c^2) without Systematics	Limits (GeV/c^2) with Systematics
Axigluon	$200 < M < 1020$	$200 < M < 980$
Excited Quark	$200 < M < 780$	$210 < M < 520$
		$600 < M < 760$
Technirho	$220 < M < 500$	$260 < M < 470$
	$580 < M < 740$	
W'	$270 < M < 460$	$300 < M < 420$
Z'	$360 < M < 425$	--
E_6 *Diquark*	$250 < M < 440$	$290 < M < 420$

The limits on new particle productions are summarized in Table 5.5.

Chapter 6

Dijet Angular Distribution Analysis

In QCD, parton hard scattering produces jets with an angular distribution that is peaked strongly in the forward direction. At its lowest order, the shape of the dijet angular distribution is almost independent of the parton structure functions. Beyond QCD, any modification to the parton-parton interaction arising from new physics such as quark compositeness will modify the angular distribution, thus the dijet angular distribution provides not only a fundamental test of QCD but also a powerful tool to search for new physics.

This chapter describes the study of the dijet angular distribution. Section 6.1 will introduce the angular variables used in this analysis, and section 6.2 discusses the measurement of the dijet angular distribution. The major part of this chapter discusses the estimate of the acceptance correction on the measured dijet angular distribution and its systematic uncertainties (section 6.3). The goal is to get a dijet angular distribution that can be directly compared with the parton level calculation from QCD or QCD plus new physics. In section 6.4 the corrected dijet angular distribution and its comparison to leading order (LO) and next to leading order (NLO) QCD predictions are discussed. Finally, a test for possible quark compositeness has been done by comparing the dijet angular distribution to a model which adds a contact term to the leading order QCD Lagrangian: This is discussed in section 6.5.

6.1 Angular Variables

The angular variable used in this analysis is [59],

$$\chi = \frac{\hat{u}}{\hat{t}}, \tag{6.1}$$

where $\hat{u}$ and $\hat{t}$ are so called Mandelstam variables: the "hats" denote subprocess (quark or gluon interaction) variables.

In the approximation of onshell zero mass partons with zero intrinsic transverse momenta, χ is then simply related to experimentally measurable quantities by

$$\chi = e^{2|\eta^*|} = e^{|\eta_1 - \eta_2|}, \tag{6.2}$$

where η_1, η_2 are the rapidities of the two leading jets. This variable is related to scattering angle θ^* by the following equation,

$$\chi = \frac{1 + \cos\theta^*}{1 - \cos\theta^*}, \tag{6.3}$$

where for the case of $2 \rightarrow 2$ scattering θ^* is the angle between one of the jets and the proton beam in center of mass frame of the parton-parton. The variable χ has the benefit of only containing angular quantities, and hence is better understood than a variable that involves jet energies that must be boosted back to the center of mass frame of the two jets in the event.

To have a uniform acceptance as a function of mass and to avoid extreme sensitivity to regions outside the central detector, the analysis requires $\chi < 5$, which is equivalent to $|\cos\theta^*| < 2/3$. To have the greatest sensitivity to new

physics and to characterize the shape of the angular distribution in a mass bin with a single number, the angular variable R_χ is introduced

$$R_\chi = \frac{N(\chi < 2.5)}{N(2.5 < \chi < 5)}. \tag{6.4}$$

This variable is the ratio of the number of dijets with $\chi < 2.5$ to the number off dijets with $2.5 < \chi < 5$. The pivot point 2.5 in the ratio is chosen from Monte Carlo studies to optimize the sensitivity to a contact interaction from compositeness. Isotropic angular distributions and contact interactions both tend to produce more events in the region $\chi < 2.5$ than QCD, and will have a higher value of R_χ than QCD.

6.2 Dijet Angular Distribution Measurement

The dijet angular distribution analysis uses the same data sample and event selection criteria as the new particle search discussed in a previous chapter. The raw dijet angular distribution was measured in five mass bins of corrected dijet mass: $241 < M < 300$, $300 < M < 400$, $400 < M < 517$, $517 < M < 625$, and $M > 625$ GeV/c^2, using data from jet 50, jet 70 and jet 100 three single jet triggers. Jet 20 trigger data was not directly used in this analysis since there is no lower E_T threshold trigger to measure its trigger efficiency as a function as χ. The first 3 mass regions were chosen to be highly efficient for the jet 50, 70, and 100 triggers respectively. The high fluctuation around 550 GeV/c^2 region and the excess in the dijet mass spectrum at high mass leads to the last two mass bins.

In Fig 6.1 the raw angular distributions are plotted as a function of χ. The measured mean χ, number of events, trigger efficiency, $dn/d\chi$, acceptance and

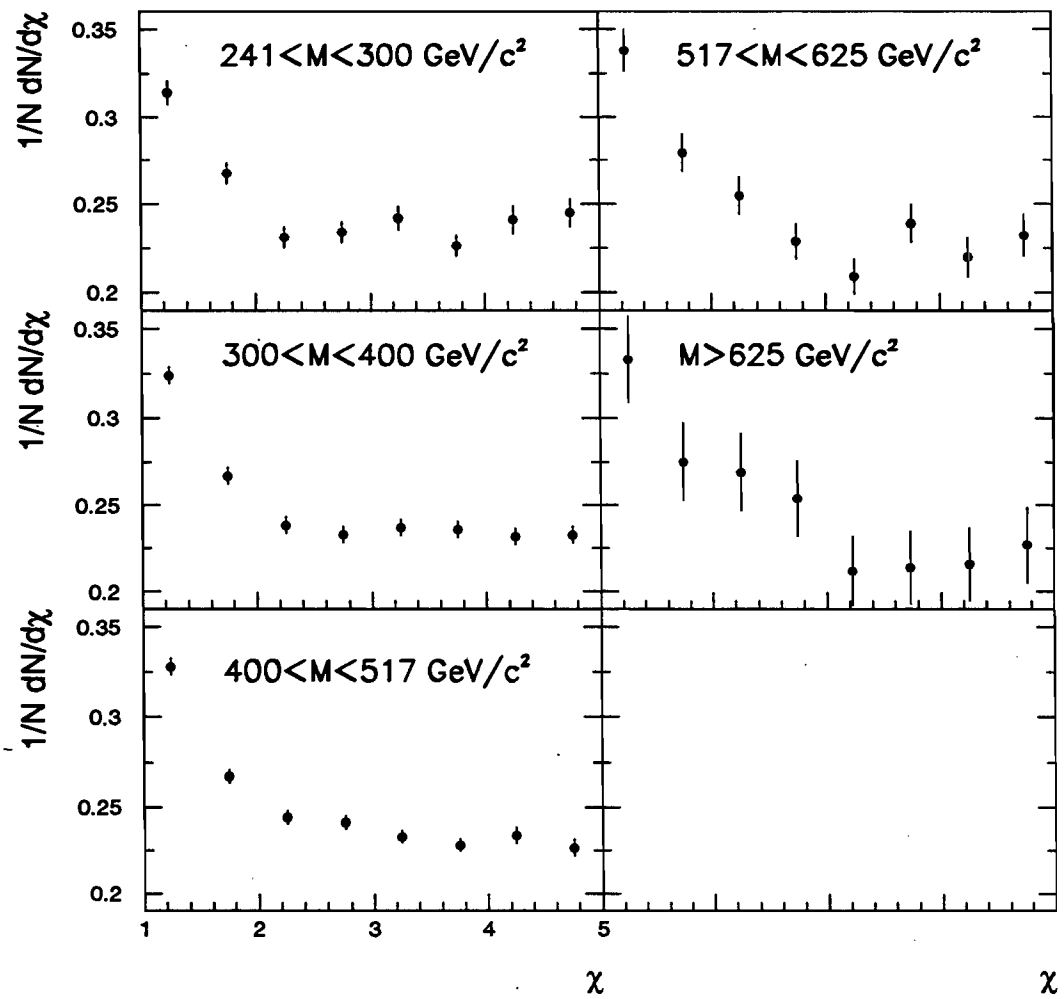

Figure 6.1: The dijet angular distribution (points), before smearing acceptance corrections, for five different mass regions.

statistical error are summarized in Table 6.4.

6.3 Acceptance and Systematics

The standard JTC96 jet response correction tries to correct jets back to partons, but it does not account for the possible energy resolution smearing effects on the angular distribution in the steeply falling dijet mass spectrum. A further correction has to be made for the measured dijet angular distribution. This additional correction will yield an angular distribution that can be directly compared to parton level calculations from QCD and QCD plus new physics.

As in the previous analysis [60], the derivation of the correction is based on the parton level fast jet detector simulation. The following sections provide a brief description and summary of the CDF fast jet simulation and the techniques used for deriving the corrections and corresponding systematics.

6.3.1 Fast CDF Jet Simulation

Monte Carlo simulations are used to understand the resolution and detector response to jets. Detailed event and detector simulation is very time consuming, and it is an impossible task to pass all generated events through a full detector simulation. Instead, this study uses a fast simulation program which can transform partons to jets very quickly without requiring a detailed detector simulation.

Monte Carlo event generator PAPAGENO

The PAPAGENO program [61] is a parton level event generator. This means that there is no initial or final state shower simulation. Instead of producing

hundreds of final state particles, PAPAGENO produces only final state partons. The PAPAGENO program starts with structure functions which describe the momentum distribution of the partons. Once the initial state partons have been chosen, using one of a variety of possible structure functions, PAPAGENO constructs a dijet event, constrained only by energy-momentum conservation. If the event falls within the kinematic boundaries specified, PAPAGENO then calculates a first order matrix element for the event. The events generated are assigned weights according to their probability of occurrence according to the matrix element used. The sum of all weights is equal to the cross section for the process generated.

Fast jet detector simulation QDJTMC

The CDF collaboration has developed a program, called QDJTMC [62], that takes the four vectors of generated partons and degrades the energy using the response map determined from jet balancing. The version of QDJTMC used in this analysis corresponds to the JTC96 jet corrections. QDJTMC simulates the jets in the following steps.

- A small transverse boost to the event is applied. This boost simulates the "intrinsic K_t", which is a result of the emission of low-P_t gluons and quarks in the interaction. QDJTMC gives the entire system a transverse momentum chosen randomly from a double Gaussian distribution. The widths of these Gaussian distributions are from CDF dijet balance analysis. This transverse momentum is applied in a random ϕ direction.

- The z position of the event vertex is chosen randomly from a Gaussian distribution. The mean and width of the Gaussian distribution is deter-

mined using data. Then a detector η for each jet is calculated using the simulated vertex.

- The η and ϕ of the parton are then smeared with Gaussian resolution functions whose widths were determined from more detailed Monte Carlo studies of jet fragmentation.
- The parton 4-vector was degraded using the inverse of the jet corrections described in section 3.3, which includes inverse corrections for underlying-event contribution, out-of-cone energy, relative and absolute energy scales (JTC96) and an additional EM energy scale drift over the run.
- Finally, the P_T of the parton was smeared to account for detector energy resolution as determined from jet P_T balance studies.

6.3.2 Jet Energy Resolution

For the purposes of kinematic comparison, correctly simulating the jet energy responses and resolutions in different detectors is of particular importance due to the rapidly falling P_t spectrum of the jets. The standard jet response JTC96 was used in the simulation. The jet energy resolution was measured using the dijet P_T balancing technique first introduced by the UA2 collaboration [63].

As in the previous analysis [64], four main detector regions are defined in the calorimeter:

- Ninety degree crack ($|\eta_d| < 0.15$)
- Central detector ($0.15 < |\eta_d| < 0.9$)
- Thirty degree crack ($0.9 < |\eta_d| < 1.4$)

- Plug detector ($1.4 < |\eta_d| < 2.2$)

The events used in the analysis were required to pass standard dijet cuts, and also required to pass the following additional cuts to reduce radiation effects and multiple interactions.

- $N_{vertex}(class > 10) \leq 2$.
- 2 and only 2 jets with P_T >15 GeV.
- At least one jet in central region.
- $\Delta\phi_{jj} < 30°$.

where $\Delta\phi_{jj} = \phi_{trigger-jet} - \phi_{probe-jet}$. The "trigger" jet means it is contained in the central region ($0.15 < |\eta| < 0.9$), and "probe" jet means it can be anywhere in η. If both jets were in the central region, then one jet at random is to be called the trigger jet, and the other is probe jet.

The dijet balancing variable is defined as,

$$K_{TL} = \frac{(P_t^{trigger} - P_t^{probe})}{(P_t^{trigger} + P_t^{probe})/2} sin(\frac{|\Delta\phi_{jj}|}{2}). \tag{6.5}$$

To check that the fast jet simulation is accurately reproducing the data, four plots of K_{TL} are made corresponding to the probe jet being in each of the four detector regions. This is reported for each of the 5 lower cuts on $2\bar{P}_t$: 241 GeV for the jet 50 trigger, 300 GeV for the jet 70 trigger, and 400, 517 and 625 GeV for the jet 100 trigger.

Fig. 6.2 shows the K_{TL} distributions for jet 50 trigger. Gaussian fits to these distributions are also shown. The values for the mean and standard deviation for this and similar fits to other P_T cuts are listed in Table 6.1.

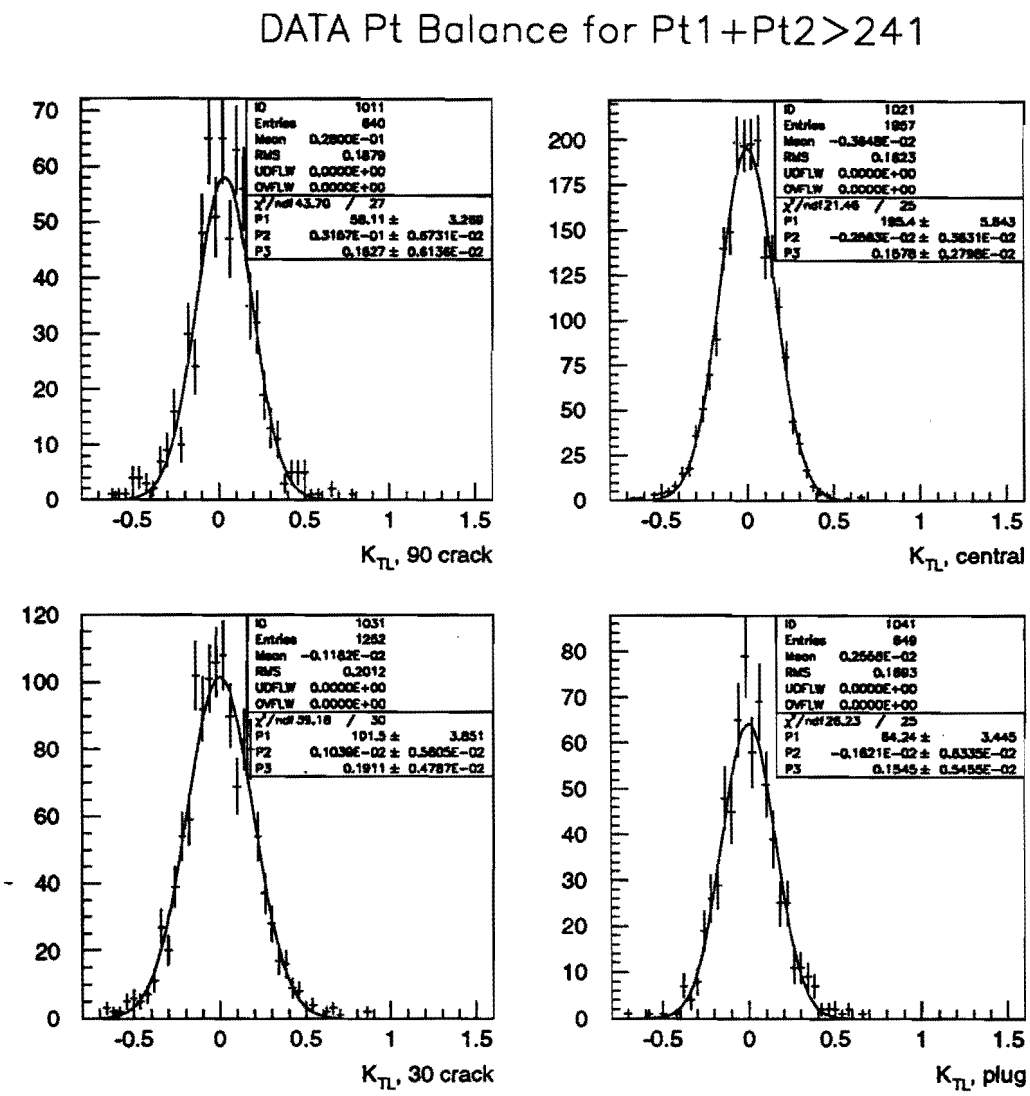

Figure 6.2: P_t balance for $2\bar{P}_t = P_{t1}+P_{t2} > 241$ GeV. The fractional difference between the jet response in a given region of the detector and the central region, K_{TL}, is shown for four regions of the detector. The data is compared to a Gaussian fit in the interval $-0.5 < K_{t\|}/\bar{P}_t < 0.5$.

Table 6.1: Dijet balancing results.

Regions	Cut on $2\bar{P}_t$	Mean×10^2			Width×10^2 (GeV/c^2)		
		Date	MC^*	MC^{**}	Data	MC^*	MC^{**}
90°Crack	241	3.16±0.67	0.10±0.07	2.91±0.07	16.27±0.62	16.63±0.05	16.55±0.06
	300	1.50±0.53	0.44±0.06	3.26±0.06	15.87±0.40	15.61±0.04	15.21±0.03
	400	2.28±0.41	0.10±0.05	3.60±0.05	14.45±0.35	14.41±0.03	14.24±0.03
	517	5.59±0.69	1.16±0.05	3.76±0.05	10.93±0.70	12.94±0.03	12.82±0.04
	625	5.68±1.84	1.59±0.05	4.09±0.05	12.70±1.90	12.00±0.04	11.88±0.03
Central	241	-0.26±0.36	-0.05±0.04	-0.04±0.04	15.78±0.28	15.99±0.03	16.00±0.03
	300	-0.39±0.28	-0.06±0.03	-0.03±0.03	14.78±0.24	14.83±0.02	14.80±0.02
	400	-0.23±0.21	-0.12±0.03	-0.11±0.03	13.09±0.18	13.14±0.02	13.15±0.02
	517	0.62±0.45	-0.26±0.03	-0.16±0.03	11.71±0.41	11.47±0.02	11.52±0.02
	625	1.92±0.96	-0.17±0.03	-0.14±0.03	11.22±1.41	10.27±0.02	10.21±0.02
30°Crack	241	0.10±0.56	2.21±0.06	-0.97±0.06	19.11±0.48	18.16±0.03	19.17±0.04
	300	-0.03±0.46	2.90±0.05	-0.56±0.05	17.80±0.37	17.62±0.03	18.06±0.04
	400	-0.52±0.43	3.41±0.48	0.14±0.05	16.61±0.37	16.13±0.03	16.35±0.03
	517	-1.90±1.44	3.93±0.06	0.87±0.07	14.66±1.32	14.51±0.04	14.63±0.04
	625	–	4.32±0.08	1.28±0.08	–	13.24±0.06	14.63±0.04
Plug	241	-0.16±0.63	1.21±0.07	1.22±0.07	15.45±0.55	17.05±0.05	17.09±0.05
	300	-0.11±0.66	0.84±0.08	0.09±0.07	14.78±0.61	15.74±0.05	15.73±0.05
	400	-0.46±1.01	0.98±0.09	0.84±0.09	13.27±0.82	14.05±0.07	14.18±0.06
	517	–	–	–	–	–	–
	625	–	–	–	–	–	–

Ideally, the K_{TL} distribution should be centered at zero with the corrected jets (i.e. after applying JTC96X). Deviation of the mean K_{TL} from zero comes from several sources such as the relative energy scales of different detectors, the effect of soft third jet, and the smearing effect due to the intrinsic detector resolutions. The width of the K_{TL} distribution is a two-jet resolution smearing effect, it relates to the one jet resolution by the following relation,

$$\bar{P}_T \cdot \sigma_{K_{TL}} = \sqrt{\sigma^2_{probe-jet} + \sigma^2_{trigger-jet}}. \tag{6.6}$$

So in the central region the single jet resolution is given by

$$\sigma_{probe-jet} = \bar{P}_T \cdot \sigma_{K_{TL}}/\sqrt{2}. \tag{6.7}$$

The jet energy resolution can be fit to a linear function of P_T as

$$\sigma = A + B \cdot P_T. \tag{6.8}$$

Table 6.2 shows parameter A and B for different detector regions for jet events with $P_{T1} + P_{T2} > 240GeV$.

Table 6.2: Jet energy resolution fitting parameters.

Region	A	B
90° Crack	0.20485	-0.26272×10^{-3}
Central	0.19964	-0.29093×10^{-3}
30° Crack	0.19904	-0.23169×10^{-3}
Plug	0.19120	-0.26573×10^{-3}

6.3.3 Comparison of Data and Fast Jet Simulation

The results of P_T balancing are shown in Fig. 6.3 and Fig. 6.4. The means and widths of the K_{TL} distributions in different detector regions from data are compared with two different versions of the fast jet Monte Carlo simulation. The two simulations differ only in the jet response in the 90 degree crack and the 30 degree crack regions. In the standard version of the fast jet simulation which is based on the jet correction JTC96, the simulation results agree adequately with the data for all regions except the 30 degree crack and the 90 degree crack.

To solve the inability of the standard version to reproduce the data in the crack regions, the jet corrections in the 90 degree crack and the 30 degree regions are "tuned" to get a better agreement between data and the Monte Carlo simulation. Fig. 6.3 and Fig. 6.5 are the comparisons of the K_{TL} distribution between data and the tuned simulation for $2\bar{P}_t = P_{t1} + P_{t2} > 241$ GeV. The agreement is considerably better for this tuned version Monte Carlo simulation.

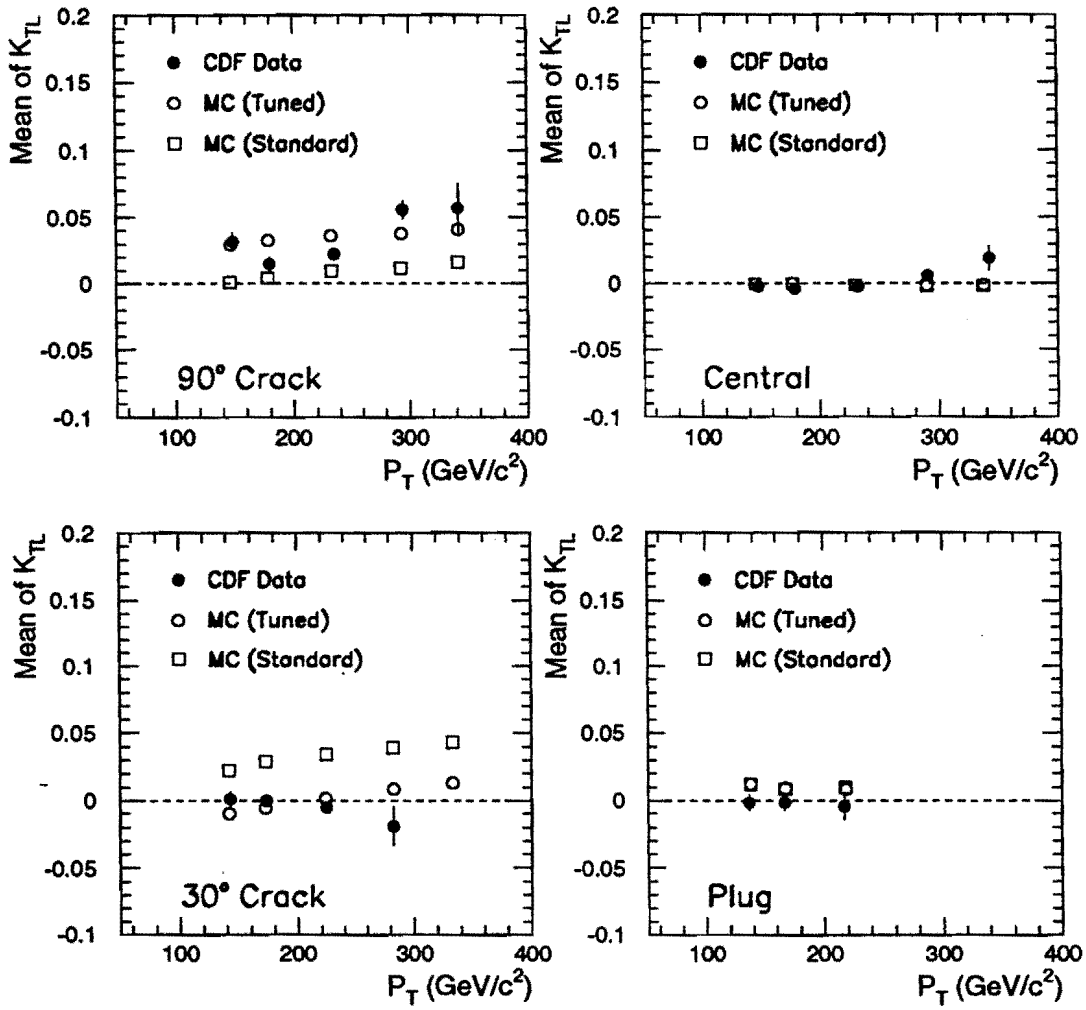

Figure 6.3: The σ of the K_{TL} distribution is shown in four regions of the detector as a function of $\bar{P}_t$. The data (solid) is compared to the jet simulation using (PAPAGENO + QDJTMC + JTC96) (open).

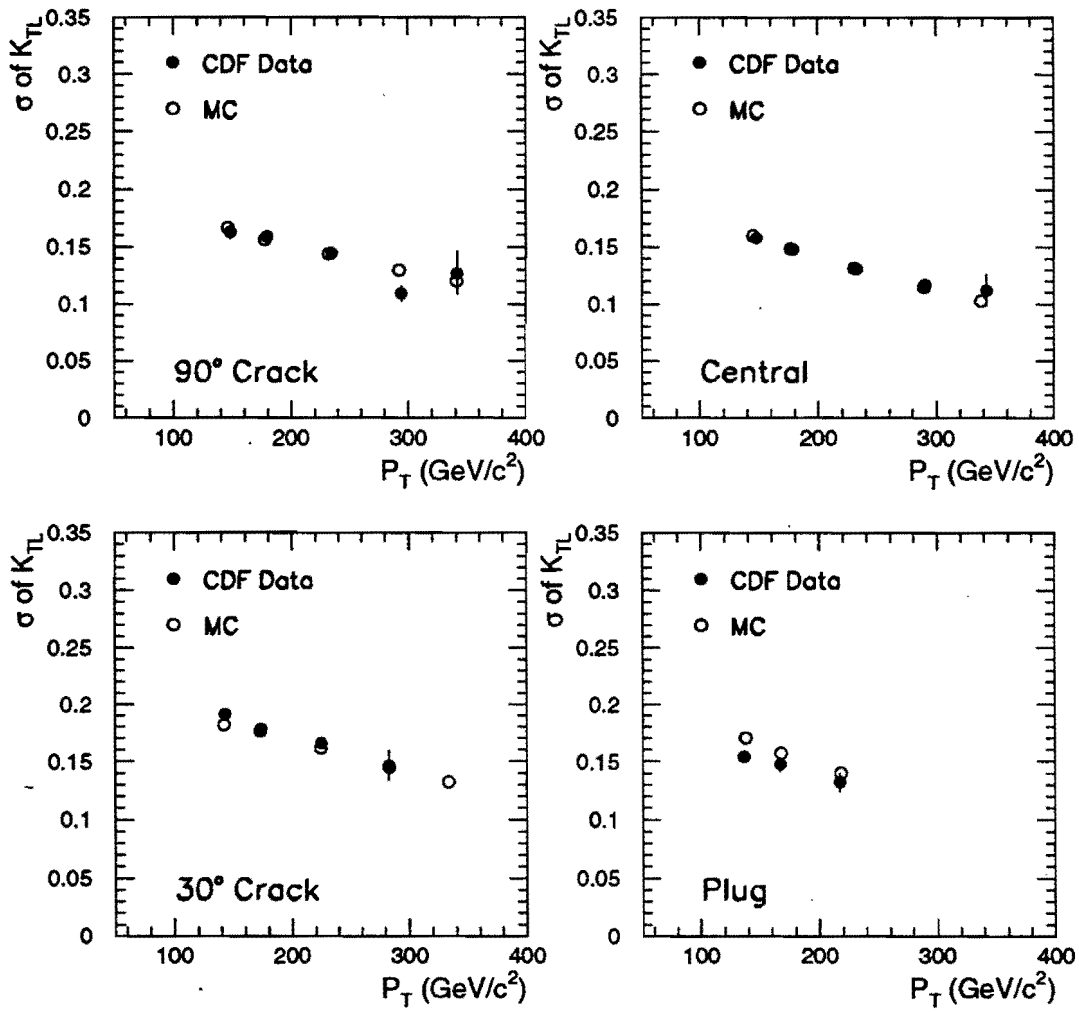

Figure 6.4: The σ of the K_{TL} distribution is shown in four regions of the detector as a function of $\bar{P}_t$. The data (solid) is compared to the jet simulation using (PAPAGENO + QDJTMC + JTC96) (open).

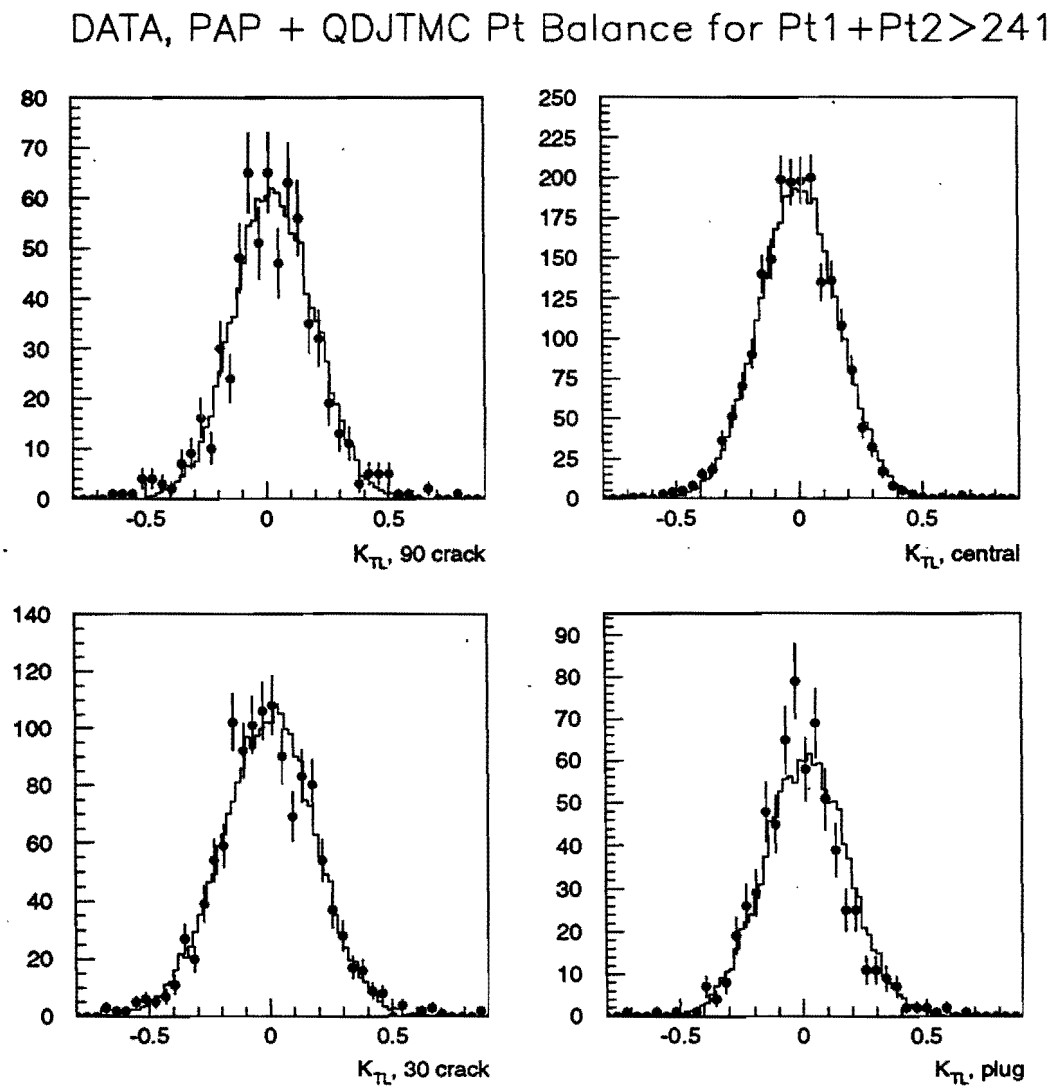

Figure 6.5: P_t balance for $2\bar{P}_t = P_{t1}+P_{t2} > 241$ GeV. The fractional difference between the jet response in a given region of the detector and the central region, K_{TL}, is shown for four regions of the detector. The data (points) is compared to our tuned jet simulation using PAPAGENO + QDJTMC + JTC96 (histogram).

The tuning is based on the difference between data and the standard simulation in Fig. 6.3. In the 30° crack region, the mean of the K_{TL} distribution in data is about 4% above zero. This can be explained as a jet energy resolution smearing effect, since the resolution is significantly worse in the 30 degree crack than in the central. This causes a resolution bias in the 30 degree crack, because a jet which fluctuates up to satisfy the $\bar{P}_t$ cut is more likely to be the jet in the 30 degree crack than the central region. This causes a shift to higher K_{TL}.

This has been checked by writing a toy Monte Carlo of two jets of unequal resolutions on a falling spectrum ($dn/dP_t \sim 1/P_t^5$). When the resolutions of the two jets in the toy Monte Carlo are set to be what was measured for the 30 degree crack and the central regions, a 4% shift in K_{TL} is obtained, which is just like the standard simulation. Clearly, this effect happens in the data too, so why is the mean K_{TL} zero in the data, and not 4%? This is presumably because the jet corrections were determined using a form of P_t balance (MPF vs $\bar{P}_t$) and therefore the jet corrections themselves were biased to be 4% low in the 30 degree crack. They therefore correct the data to have zero $MPF/\bar{P}_t$ which in the case of the 30 degree crack appears to also give zero K_{TL}. Thus there may be a 4% error in the jet corrections for the 30 degree crack region.

The difference in the 90° crack is not well understood. Since the most significant differences occur at high P_T, the differences might be caused by the way the low P_T data extrapolates to high E_T.

In the tuned simulation, the jet response is increased by 3% in the 90 degree crack and is decreased by 4% in the 30 degree region to get a better agreement with data.

The figures shown in Fig. 6.3 6.4 and 6.5 demonstrate that the tuned Monte Carlo is doing a good job of representing the data. Therefore, we can be confident in using the Monte Carlo prediction to study the acceptance correction and corresponding systematics uncertainties.

6.3.4 Acceptance

The acceptance is defined as the ratio of the angular distribution of jets after detector simulation to the angular distribution of the generated partons. This models detector smearing and response effects for a typical falling spectrum. Dividing the data by the acceptance gives a parton level angular distribution which can be directly compared with parton level QCD calculation.

The acceptance from the tuned simulation is shown in Fig. 6.6. Since it is really a smearing and response effect, it is always greater than one reflecting the resolution smearing of lower mass dijets into higher mass regions on a rapidly falling spectrum. Actually, it is the response and not the resolution that is most critical. The acceptance is falling as a function of χ mainly due to the raising response of the 90 degree crack and the lowering response of the 30 degree crack. When the standard monte carlo was used, the acceptance was pretty flat for most mass bins and rose vs. χ for the last two mass bins as shown in Fig. 6.7. The acceptances from two Monte Carlo simulations have the opposite affect on the angular distribution. Overall, the tuned Monte Carlo acceptance brings data into better agreement with QCD than the standard Monte Carlo acceptance.

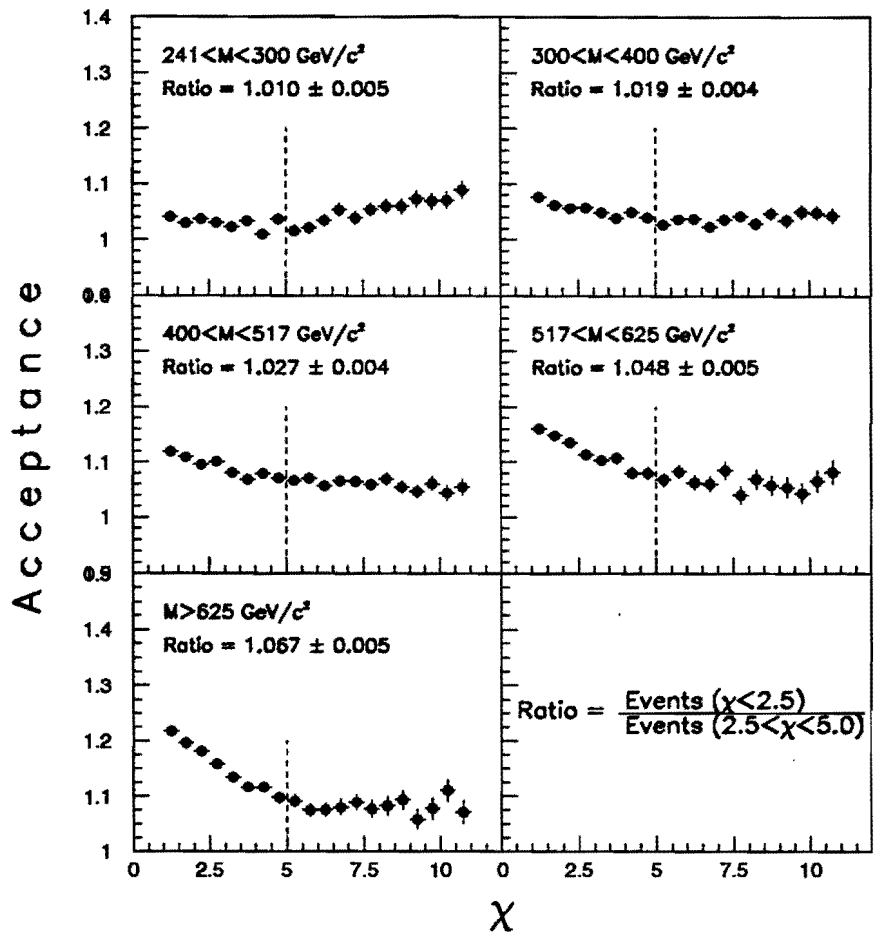

Figure 6.6: The acceptance from the TUNED simulation for the true dijet angular distribution is shown as a function of χ in 5 regions of dijet mass. We will only measure up to $\chi = 5$ shown by the dashed line. The acceptance for R_χ is indicated for each mass region.

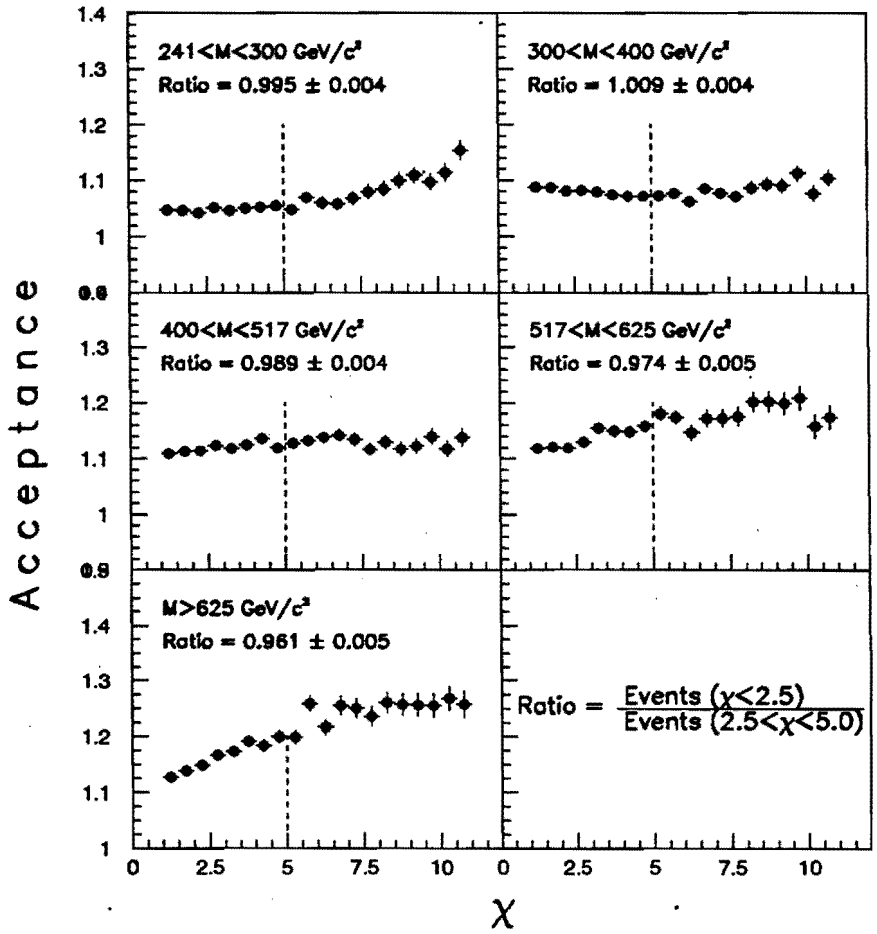

Figure 6.7: The acceptance from the standard simulation for the true dijet angular distribution is shown as a function of χ in 5 regions of dijet mass. We will only measure up to $\chi = 5$ shown by the dashed line. The acceptance for R_χ is indicated for each mass region. The acceptance is different than for the fully tuned Monte Carlo, and the difference is slightly smaller than the value of our final systematic uncertainty.

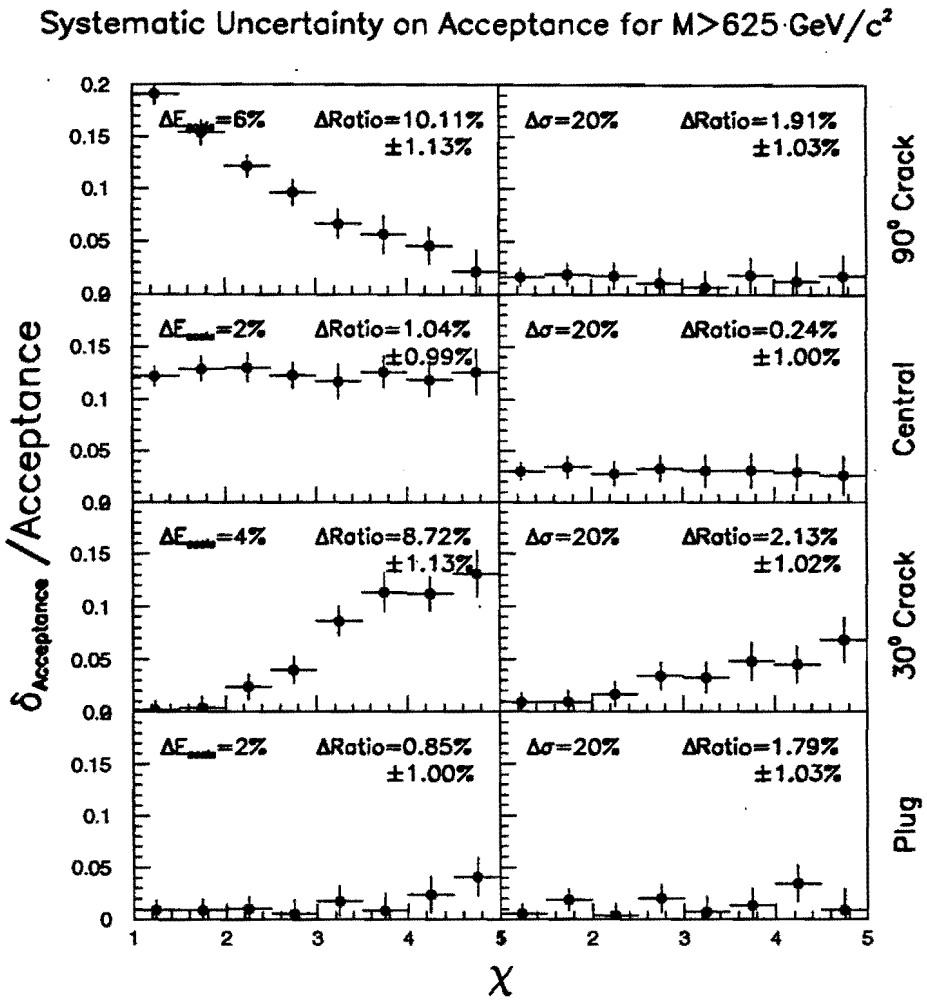

Figure 6.8: For $M > 625$ GeV, the fractional change in the acceptance when varying the jet response and resolution by the amount indicated, is shown for the four different detector regions. We are running longer jobs to improve the statistics.

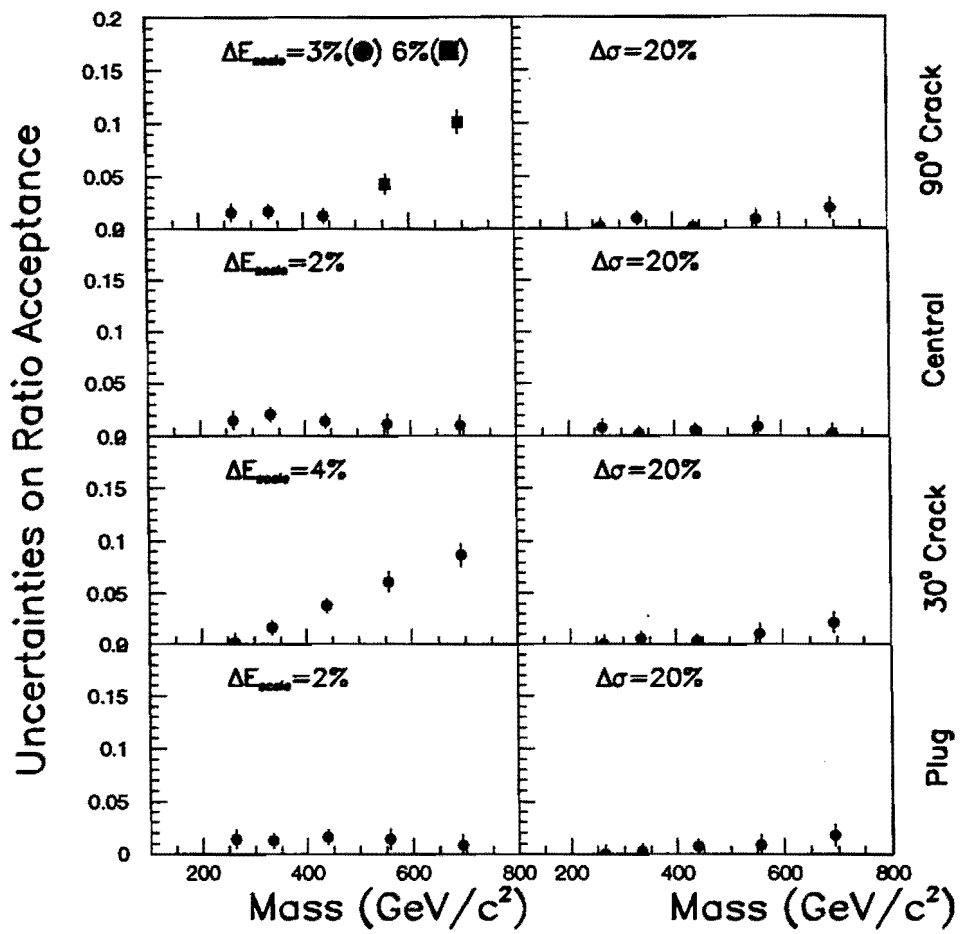

Figure 6.9: The change in the ratio acceptance when varying the jet response and resolutions by the amount indicated, is shown for the four different detector regions by solid circles. The solid squares are for varying the response in the 90 degree crack by 6% instead of 3%.

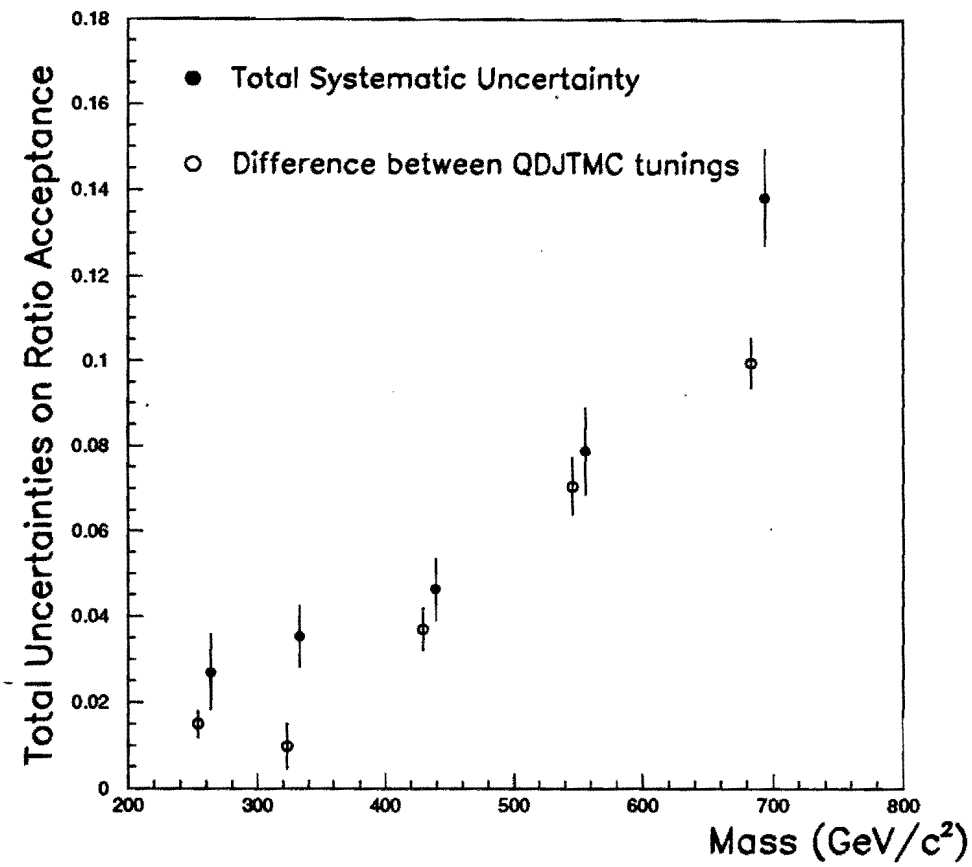

Figure 6.10: The total fractional systematic uncertainty on the R_χ (solid points) is compared with the difference in acceptance between the fully tuned and the partially tuned detector simulations (open points) as a function of mass.

6.3.5 Systematic Uncertainty on Acceptance

The systematic uncertainties of the energy scales in the 90° crack and 30° crack regions are assigned the values 3-6% and 4% respectively based on the Monte Carlo studies. For the central and plug regions the Monte Carlo and data agree to better than 2%, so an error of 2% is assigned for these regions. Like the previous analysis [60] a systematic uncertainty of 20% on the resolution is assigned to all detector regions, significantly more than the tiny differences between the data and Monte Carlo. Table 6.3 summarizes the systematics used in this analysis.

Table 6.3: Systematic Uncertainty on Acceptance.

Regions	Systematic Uncertainty	
	Energy Scale	Energy Resolution
90° Crack	3% ($M < 517$ GeV) 6% ($M > 517$ GeV)	20%
Central	2%	20%
30° Crack	3%	20%
Plug	2%	20%

To evaluate the effect of the possible difference in energy scales and resolutions between the different regions of the detector, 16 different runs of the fast jet simulation were performed. For each of the four regions (90° crack, central, 30° crack and plug) four separate sets of acceptance corrections were evaluated by raising or lowering the corresponding energy scale or resolution by the amount indicated in Table 6.3.

The affect on the acceptance of varying the jet response and resolution in QDJTMC by their assigned systematics for the mass bin $M > 625 GeV/c^2$ is

shown in Fig. 6.8. Analogous plots were also made for the other mass bins, and they showed similar behavior. The effect of changing the resolution is negligible compared to the effect of changing the relative energy scales.

The systematics are largest at high mass due to the steeper mass distribution and the larger systematics in the 90 degree crack.

The fractional error on the ratio R_χ is also given, and that error is plotted vs. mass in Fig. 6.9. Here the figure shows that the systematic uncertainty due to the energy response is growing as a function of mass in both the 90 degree and 30 degree cracks, and that the systematics due to the jet resolutions are negligible in comparison.

The total uncertainty, arising from adding all systematic uncertainties in quadrature, is shown in Fig. 6.10 (fractional error on R_χ). Note that this systematic is slightly greater than the difference in the two tunings of the Monte Carlo, reflecting the additional systematics due to the other regions of the detector.

6.4 Corrected Angular Distribution and QCD

The dijet angular distribution, corrected for trigger efficiency and acceptance, is shown in Fig. 6.11 and Table 6.4. In Fig. 6.11 the data is compared to LO QCD with different choices of the renormalization scale and CTEQ2L parton distribution function. In Fig. 6.12 it is compared to a NLO QCD calculation (JETRAD) with CTEQ2M parton distribution function. Many alternate parton distribution sets were tried, and the QCD predictions were insensitive to the choice. The only significant theoretical uncertainty in the QCD calculation is the renormalization scale μ. The scale dependence of the shape of the χ

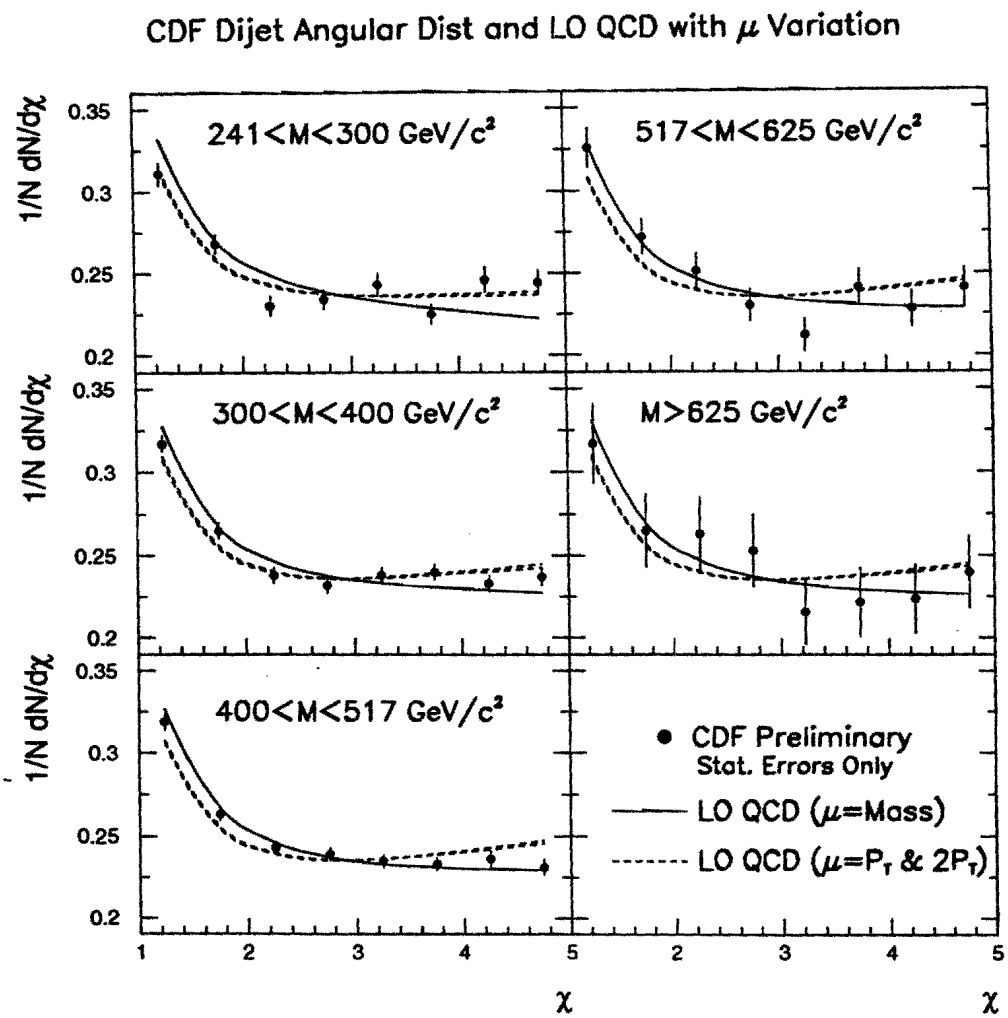

Figure 6.11: The dijet angular distribution (points), after acceptance corrections, is compared to parton level LO QCD with renormalization scale $\mu = Mass$ (solid) and $\mu = P_t$ and $\mu = 2P_t$ (dashed).

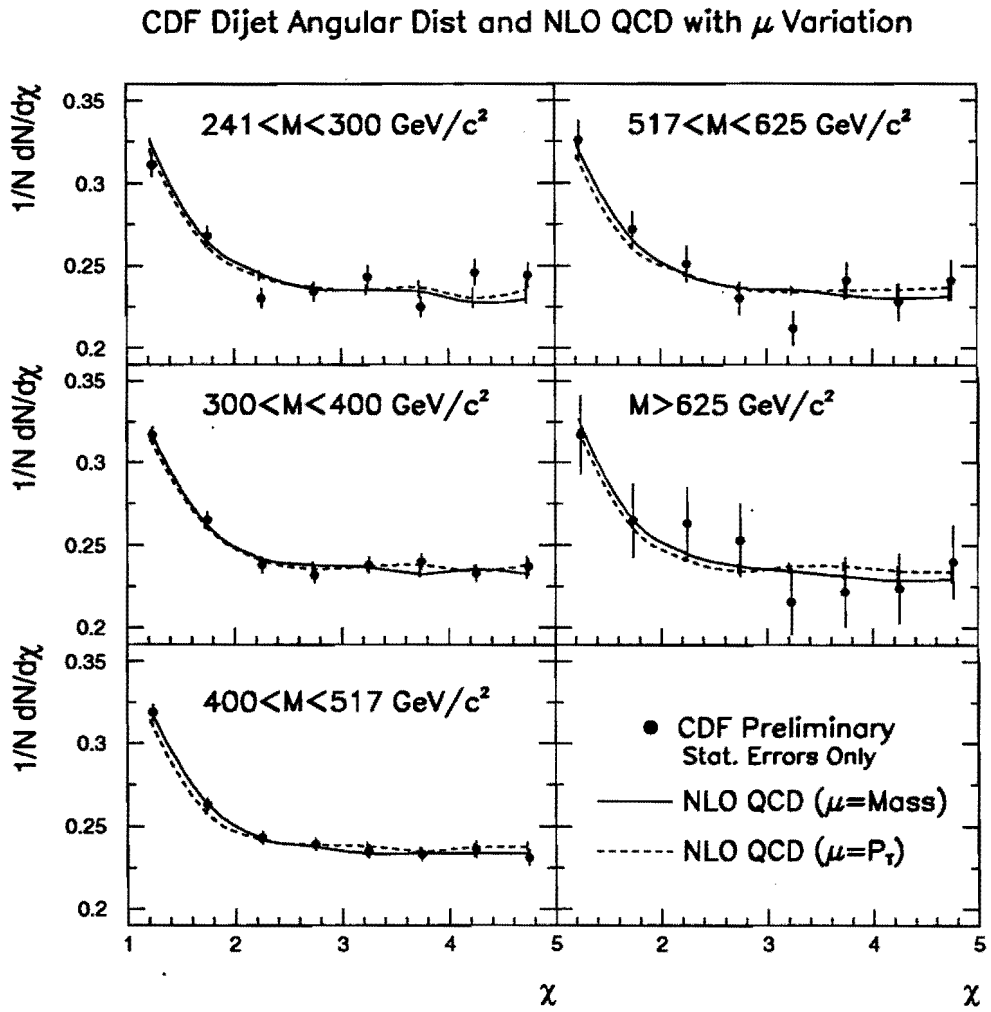

Figure 6.12: The dijet angular distribution (points), after acceptance corrections, is compared to parton level NLO QCD (from JETRAD) with renormalization scale $\mu = \sqrt{\hat{s}}$ (solid) and $\mu = P_t$ (dashed).

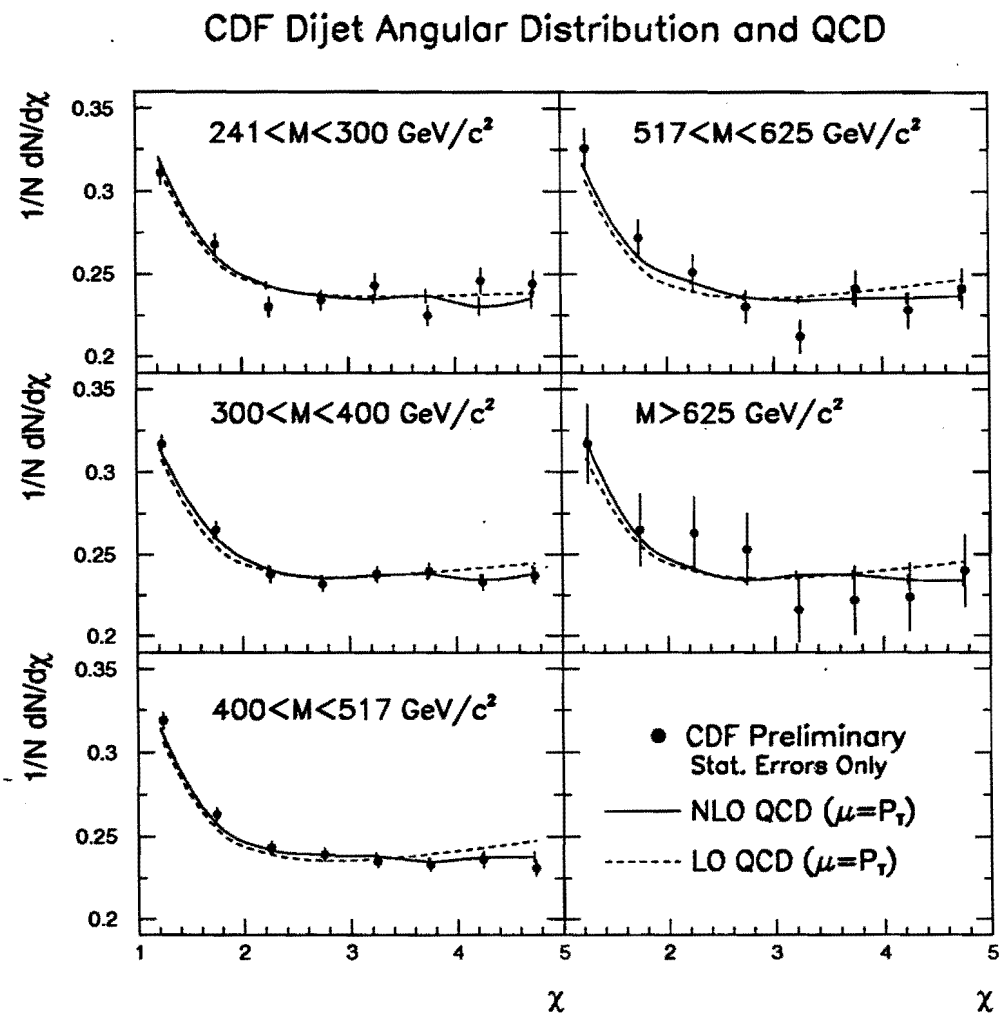

Figure 6.13: The dijet angular distribution (points), after acceptance corrections, is compared to parton level NLO QCD (solid) and LO QCD (dashed), both with a renormalization scale $\mu = P_t$.

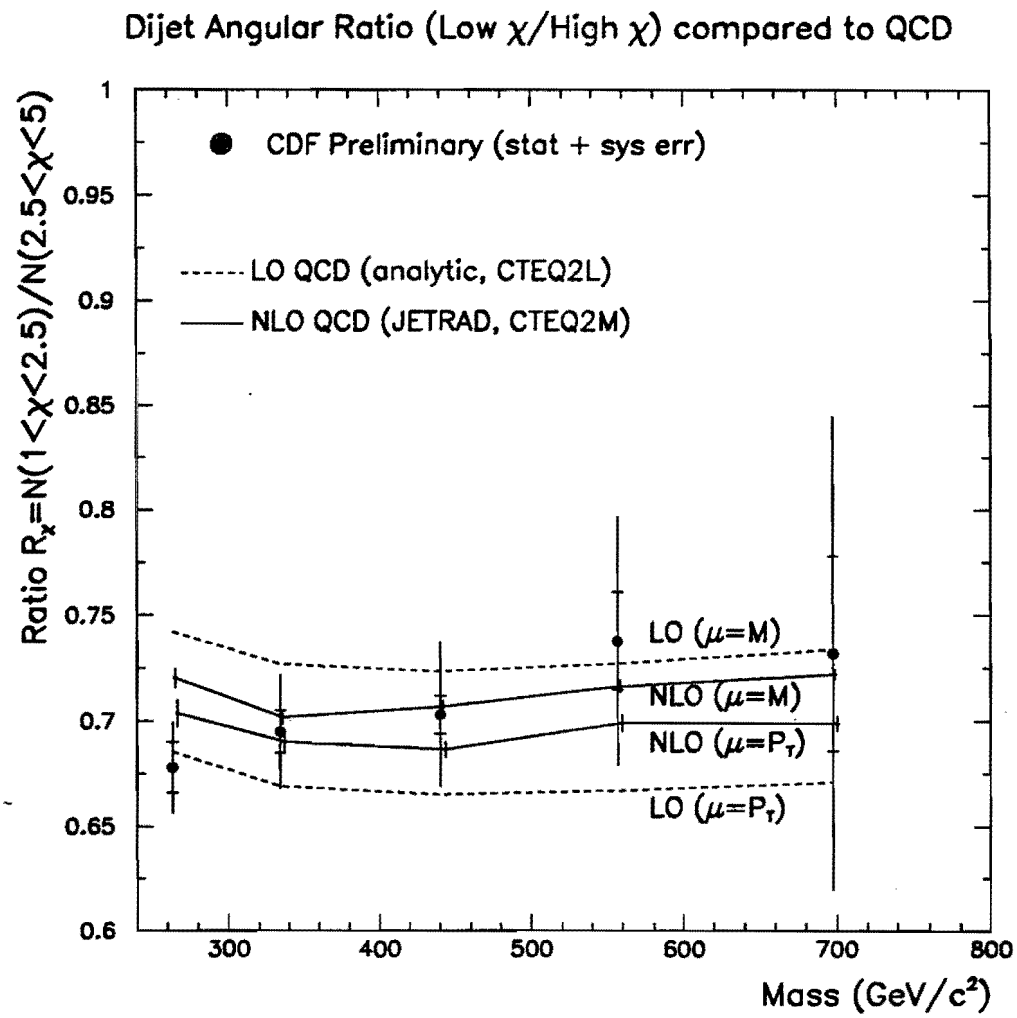

Figure 6.14: The dijet angular ratio (points), after acceptance corrections, is compared to parton level QCD calculations at LO (dashed) at NLO (solid). The inner error bars are statistical, the outer error bars are systematic and statistical errors added in quadrature, and the small errors on the NLO theory are statistical.

Mass	χ	Events	Uncorr. $\frac{dN}{d\chi}$	Trigger Eff	Acceptance	$\frac{dN}{d\chi}$	Stat. Err.
241-300	1.239	2379	0.317	1.000	1.042	0.311	0.007
	1.752	2027	0.270	1.000	1.030	0.268	0.006
	2.247	1752	0.233	1.000	1.036	0.230	0.006
	2.748	1770	0.236	1.000	1.030	0.234	0.006
	3.249	1807	0.241	0.988	1.023	0.243	0.007
	3.750	1712	0.228	1.000	1.033	0.225	0.006
	4.250	1764	0.235	0.967	1.010	0.246	0.008
	4.748	1812	0.241	0.975	1.037	0.244	0.008
300-400	1.239	3795	0.327	0.995	1.077	0.317	0.005
	1.747	3108	0.268	0.990	1.063	0.265	0.005
	2.252	2776	0.239	0.989	1.057	0.238	0.005
	2.747	2717	0.234	0.991	1.057	0.232	0.005
	3.254	2749	0.237	0.986	1.049	0.238	0.005
	3.750	2723	0.234	0.979	1.038	0.240	0.005
	4.253	2685	0.231	0.983	1.049	0.233	0.005
	4.752	2674	0.230	0.974	1.040	0.237	0.005
400-517	1.235	4662	0.331	1.000	1.119	0.319	0.005
	1.743	3811	0.270	1.000	1.109	0.263	0.004
	2.250	3473	0.246	0.998	1.096	0.243	0.004
	2.751	3416	0.242	0.995	1.100	0.239	0.004
	3.248	3288	0.233	0.990	1.080	0.235	0.004
	3.747	3226	0.229	0.993	1.068	0.233	0.004
	4.252	3227	0.229	0.970	1.078	0.236	0.005
	4.753	3099	0.220	0.961	1.070	0.231	0.005
517-625	1.234	752	0.340	1.000	1.161	0.326	0.012
	1.743	622	0.281	1.000	1.149	0.272	0.011
	2.249	566	0.256	1.000	1.135	0.251	0.011
	2.743	508	0.230	1.000	1.112	0.230	0.010
	3.249	464	0.210	1.000	1.103	0.212	0.010
	3.754	530	0.240	1.000	1.108	0.241	0.011
	4.253	483	0.218	0.987	1.080	0.228	0.011
	4.747	500	0.226	0.968	1.080	0.241	0.012
> 625	1.250	176	0.333	1.000	1.218	0.317	0.024
	1.741	145	0.275	1.000	1.196	0.265	0.022
	2.249	142	0.269	1.000	1.181	0.263	0.022
	2.744	134	0.254	1.000	1.158	0.253	0.022
	3.220	112	0.212	1.000	1.135	0.216	0.020
	3.733	113	0.214	1.000	1.116	0.222	0.021
	4.253	114	0.216	1.000	1.116	0.224	0.021
	4.760	120	0.227	1.000	1.097	0.240	0.022

Table 6.4: The mean JTC96 corrected dijet mass, mean χ, number of events, raw $dn/d\chi$, trigger efficiency, detector acceptance, corrected $dn/d\chi$ and statistical uncertainty. The statistical uncertainty is dominated by the statistical uncertainty in the data, but also contains point to point statistical uncertainties in the measured trigger efficiency and the Monte Carlo acceptance.

distribution is smaller at NLO, and the agreement between the data and QCD is good. In Fig. 6.13 we compare the experimental results to both LO and NLO QCD in one plot.

Mass (GeV/c^2)	Events	Raw R_χ	R_χ Trigger Efficiency	R_χ Acceptance	Corr. R_χ	Stat. Error	Sys. Error
263.448	15023	0.695	1.015	1.010	0.678	0.012	0.018
334.080	23227	0.714	1.009	1.019	0.695	0.010	0.025
440.448	28202	0.735	1.017	1.027	0.703	0.009	0.033
556.965	4425	0.781	1.009	1.048	0.738	0.023	0.054
697.674	1056	0.781	1.000	1.067	0.732	0.046	0.103

Table 6.5: The mean JTC96 corrected dijet mass, number of events, raw value of dijet angular ratio R_χ, trigger efficiency for R_χ, acceptance for R_χ, corrected value of R_χ, its statistical and systematic uncertainty. The trigger efficiency and acceptance are the effective values for the ratio R_χ, so that corrected R_χ is raw R_χ divided by efficiency and acceptance.

The shape sensitive variable, R_χ, is tabulated in Table 6.5 and shown in Fig. 6.14 compared to LO and NLO QCD calculations. The experimental data is in good agreement with QCD within the statistical and systematic uncertainties.

6.4.1 Cross Check using Central Only

The acceptance correction is very sensitive to the jet energy response and resolution as demonstrated in the previous sections. Although the corresponding systematic uncertainties have been estimated, it is important to check our results using only the central detector where the jet response and resolution are better understood. However, the geometrical effect of the η cuts for central jets dramatically distorts the shape of the χ distribution. In order to compare

with our default angular distribution, the acceptance needs to be evaluated for the central region alone. This acceptance is calculated from the ratio of the angular distribution of jets in the events in which both leading jets are in the detector pseudorapidity region $0.1 < |\eta_d| < 1.0$ to the angular distribution of the partons in the events if both the two partons were in the region of $|\eta| < 2$. This acceptance will correct the central-only χ distribution back to the χ distribution in our default region ($|\eta| < 2$).

In Fig. 6.15 the measured χ distribution in the region $0.1 < |\eta_d| < 1.0$ after correcting for acceptance is compared to our default angular distribution. The two are in good agreement with each other and with NLO QCD. Fig. 6.16 shows that R_χ for $0.1 < |\eta_d| < 1.0$ agrees with our default cut $|\eta_d| < 2.0$ within statistical and systematic uncertainties. Although the two agree within errors, the mean value of the central only R_χ is lower at high mass than our default cut R_χ, increasing the likelihood that the default acceptance corrections are not artificially removing a signal of new physics.

6.5 Dijet Angular Distribution for Compositeness

6.5.1 Quark Compositeness

In the quark composite models, quarks are considered to be bound states of more fundamental constituents. These constituents are bound together in quarks by a new, very strong, metacolour forces leading to an effective four-fermion interaction between the quarks of the strength g^2/Λ, where Λ is the energy scale of compositeness. The effective coupling constant g is unknown, but by convention Λ is defined such that $g^2/4\pi = 1$. The dijet angular distribu-

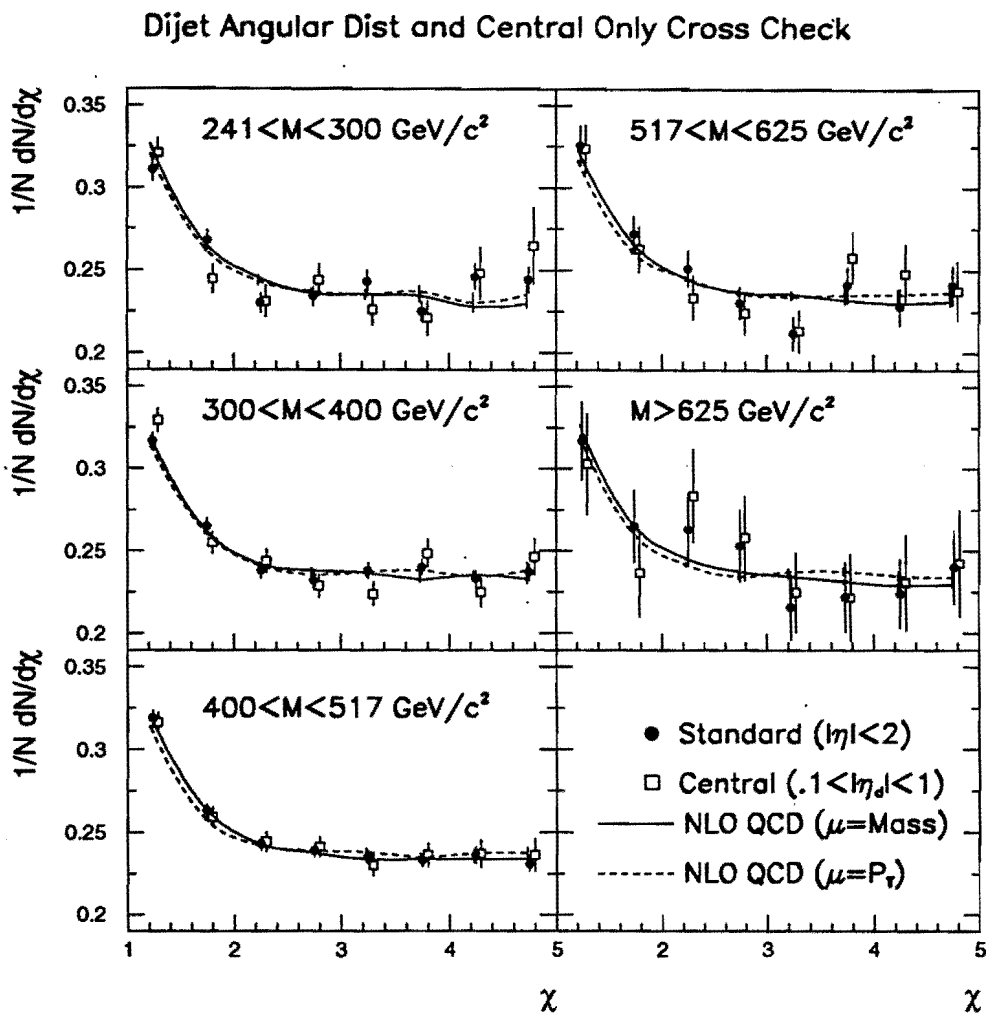

Figure 6.15: The dijet angular distribution with our default cuts (solid points), is compared to the dijet angular distribution with the more restrictive cuts $0.1 < |\eta_d| < 1.0$ (open points), after correcting each distribution for acceptance. Both distributions are compared to parton level NLO QCD (from JETRAD) with renormalization scale $\mu = \sqrt{\hat{s}}$ (solid) and $\mu = P_t$ (dashed).

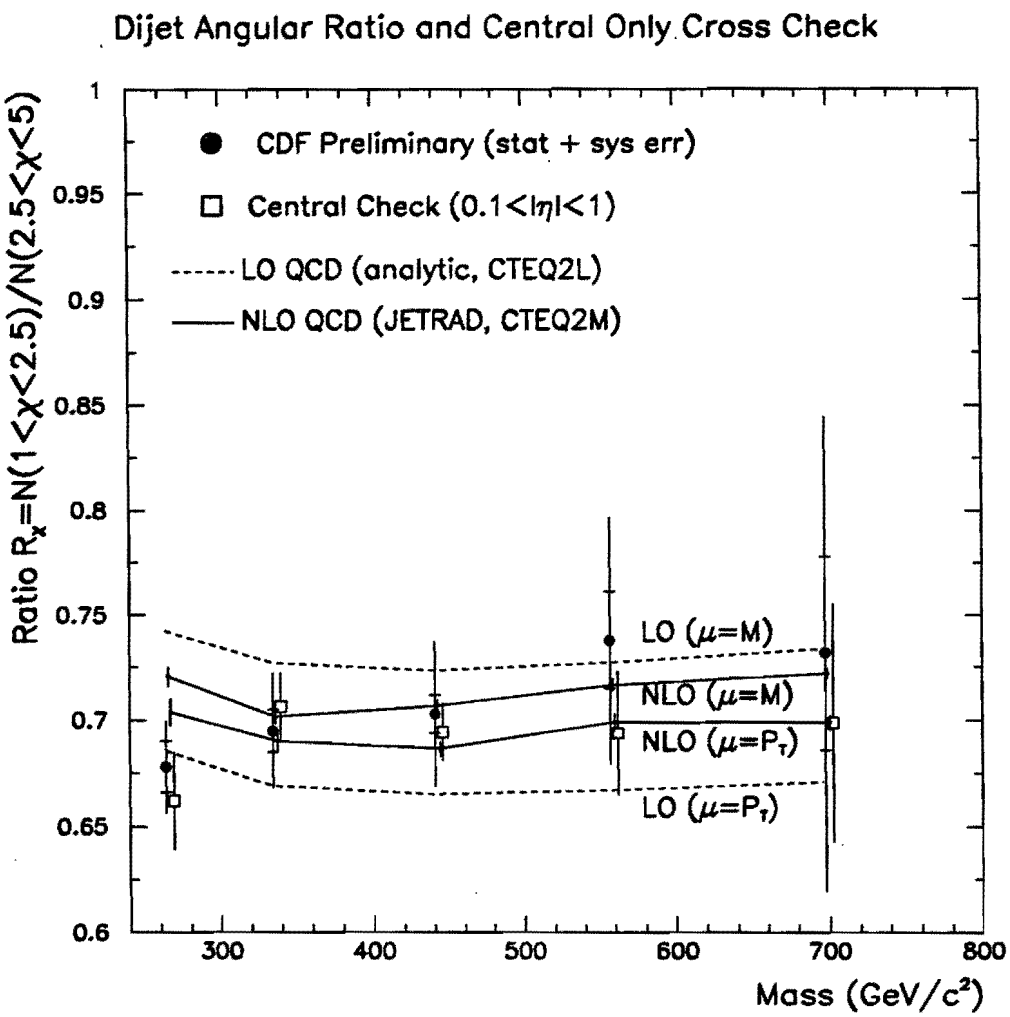

Figure 6.16: The dijet angular ratio with our default cuts (solid points) is compared to the dijet angular ratio with the more restrictive cuts $0.1 < |\eta_d| < 1.0$ (open points), after correcting each distribution for acceptance. Only statistical error bars are shown for $0.1 < |\eta_d| < 1.0$, while for the default cuts the inner error bars are statistical and the outer error bars are systematic and statistical errors added in quadrature. Both samples are compared to LO and NLO QCD (curves).

tion for contact interactions is known at lowest order for an effective Lagrangian for a flavor diagonal left-handed current [65] in the form

$$\mathcal{L} = \pm\frac{g^2}{2\Lambda^2}(\bar{q}_L\gamma^\mu q_L)(\bar{q}_L\gamma_\mu q_L). \tag{6.9}$$

Although a left-handed current is not the only possible contact interaction, it is the only one that has been investigated in the literature. Different contact interactions may produce different angular distributions, and work is currently underway to analyze these other contact interaction terms. The subprocess cross sections, modified for the above contact interaction, are available [65] for all the relevant processes. For the $q_i\bar{q}_i \to q_i\bar{q}_i$ subprocess, for example, the cross section is given to leading order in α_s by

$$\begin{aligned}\frac{d\hat{\sigma}(q_i\bar{q}_i \to q_i\bar{q}_i)}{d\hat{t}} &= \frac{4\pi}{9\hat{s}^2}\alpha_S^2\left[\frac{\hat{u}^2+\hat{s}^2}{\hat{t}^2}+\frac{\hat{u}^2+\hat{t}^2}{\hat{s}^2}-\frac{2}{3}\frac{\hat{u}^2}{\hat{s}\hat{t}}\right] \\ &+ \frac{8\pi}{9\hat{s}^2}\alpha_S^2\frac{\eta}{\Lambda^2}\left[\frac{\hat{u}^2}{\hat{t}}+\frac{\hat{u}^2}{\hat{s}}\right]+\frac{8\pi}{3\hat{s}^2}\frac{\hat{u}^2}{\Lambda^4}\end{aligned} \tag{6.10}$$

In Eq. 6.10 the first term represents the normal QCD interaction, the last term represents the direct effect of the contact interaction, and the middle term represents the interference.

The magnitude of the effect of the contact interaction will depend on the number of flavors involved. All the compositeness scales quoted in previous CDF papers assumed that only u and d quarks were composite. It has been pointed out by Ken Lane, Estia Eichten and others, that it is better to use a flavor symmetric contact interaction in which all quarks are composite. Otherwise the contact interactions produce significant flavor changing neutral decays which are excluded by measurements in the kaon system for compositeness

scales approaching 100 TeV. We have also tested a contact interaction that is flavor symmetric: all quarks are assumed composite, but only the production of the five lightest flavors produce dijets. If a flavor symmetric interaction is used, then since $q_i\bar{q}_i \rightarrow q\bar{q}$ is the largest subprocess at high mass, the size of the contact interaction is enhanced by 5/2 (five flavors in final state instead of 2), and limits on the contact scale are enhanced by roughly $(5/2)^{1/4} = 1.26$ (the rate is proportional to the Λ^4). A flavor symmetric contact interaction will be employed throughout this second analysis.

6.5.2 Comparison of Dijet angular ratio between data and Quark Compositeness

In Fig. 6.17, the right figure shows the comparison of the dijet angular ratio R_χ determined experimentally and the predictions of a compositeness model using a flavor symmetric left-handed contact interaction, and the left figure shows the same comparison with a contact interaction including only to composite u and d quarks. The prediction is at LO, but has been normalized to equal NLO QCD with $\mu = P_t$ when the compositeness scale Λ is infinite. The data are in good agreement with QCD, and there is no reason to invoke the contact interaction hypothesis. The inclusive jet PRL [66] quoted a best fit contact interaction of $\Lambda_{ud} = 1.6$ TeV.

6.5.3 Limits on the Energy Scale of Quark Compositeness

To obtain limits on a contact interaction, the traditional χ^2 method was used. The χ^2 is defined by the matrix equation

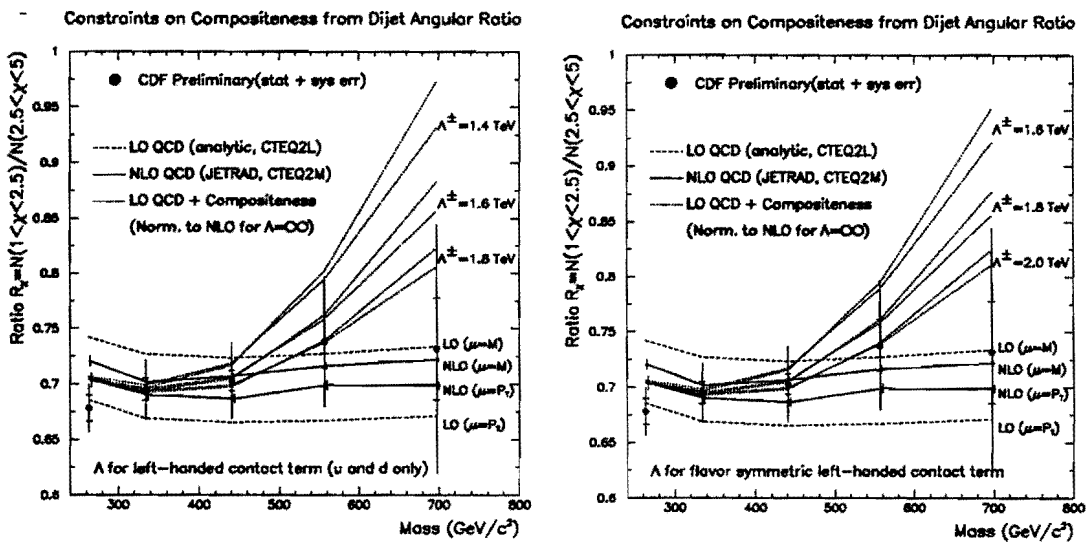

Figure 6.17: The dijet angular ratio (solid points) is compared to LO QCD (dashed), NLO QCD (solid), and LO QCD + a quark contact interaction normalized to NLO QCD for $\Lambda = \infty$ (dots). Curves are shown for 3 different compositeness scales Λ of a contact interaction for u and d quarks only (Left), and a flavor symmetric contact interaction (Right) for both positive (upper dots) and negative (lower dots) interference between QCD and compositeness.

$$\chi^2 = \Delta V^{-1} \Delta, \quad \Delta = \begin{pmatrix} \Delta_1 \\ \Delta_2 \\ \Delta_3 \\ \Delta_4 \\ \Delta_5 \end{pmatrix} \tag{6.11}$$

where Δ is a column vector of the difference between R_χ in CDF data and theory in each of the five mass bins. V^{-1} is the inverse of the symmetric variance matrix V

$$V = \begin{pmatrix} \sigma_{11}^2 & \sigma_{12}^2 & \sigma_{13}^2 & \sigma_{14}^2 & \sigma_{15}^2 \\ \sigma_{12}^2 & \sigma_{22}^2 & \sigma_{23}^2 & \sigma_{24}^2 & \sigma_{25}^2 \\ \sigma_{13}^2 & \sigma_{23}^2 & \sigma_{33}^2 & \sigma_{34}^2 & \sigma_{35}^2 \\ \sigma_{14}^2 & \sigma_{24}^2 & \sigma_{34}^2 & \sigma_{44}^2 & \sigma_{45}^2 \\ \sigma_{15}^2 & \sigma_{25}^2 & \sigma_{35}^2 & \sigma_{45}^2 & \sigma_{55}^2 \end{pmatrix} \tag{6.12}$$

where $\sigma_{ij}^2 = \rho_{ij}\sigma_i\sigma_j$, and ρ_{ij} is the correlation coefficient between ith and jth components. Since the systematic uncertainties are completely correlated as a function of mass (i.e. $\rho_{ij}(sys) = 1$), and the statistical uncertainties are completely uncorrelated as a function of mass (i.e., $\rho_{ij}(stat) = 0$), the σ_{ij}^2 were given by

$$\sigma_{ii}^2 = \sigma_i^2(stat) + \sigma_i^2(sys) \quad (i = j) \tag{6.13}$$

$$\sigma_{ij}^2 = \sigma_i(sys)\sigma_j(sys) \quad (i \neq j) \tag{6.14}$$

The covariance matrix V evaluates to

$$V = \begin{pmatrix} 4.7 & 4.5 & 5.9 & 9.7 & 18.5 \\ 4.5 & 7.3 & 8.3 & 13.5 & 25.8 \\ 5.9 & 8.3 & 11.7 & 17.8 & 34.0 \\ 9.7 & 13.5 & 17.8 & 34.5 & 55.6 \\ 18.5 & 25.7 & 34.0 & 55.6 & 127 \end{pmatrix} \times 10^{-4} \tag{6.15}$$

Fig. 6.18 shows the χ^2 between data and compositeness modes versus $1/\Lambda^4$. The χ^2 corresponding to 95% C.L. lower limit on Λ for five degree of freedom is 11.07, which defines the the 95% CL horizontal dashed line in Fig. 6.18. All hypotheses above this dashed line are excluded to at least 95% CL. The limits can be read directly off this figure. For a left-handed contact interaction between u and quarks only, the limit on the compositeness scale is $\Lambda_{ud}^+ > 1.60$ TeV and $\Lambda_{ud}^- > 1.40$ TeV at 95% CL. For a flavor symmetric left-handed model the limits are $\Lambda^+ > 1.80$ TeV, and $\Lambda^- > 1.70$ TeV.

Thus, the best fit value of $\Lambda_{ud} = 1.6$ TeV in the inclusive jet PRL [?] is unlikely, but can just barely be accomodate by this dijet angular distribution study.

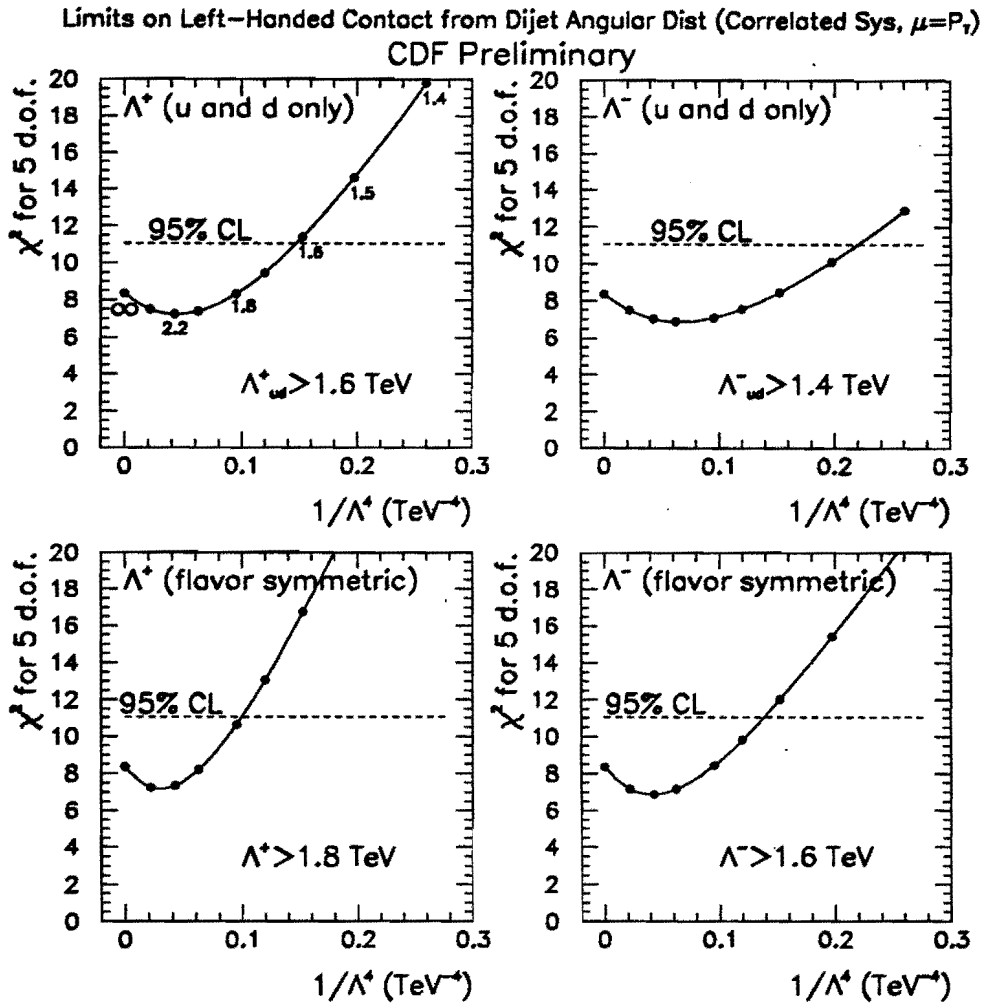

Figure 6.18: The χ^2 (points) of the comparison between data and a left-handed contact interaction vs. the inverse fourth power of the compositeness scale Λ. NLO QCD with renormalization scale $\mu = P_t$ is the leftmost point ($\Lambda = \infty$). The horizontal dashed line is 11.07, it defines the 95% CL lower bounds on the compositeness scales. The four plots are: only u and d quarks composite with positive interference (upper left) and negative interference (upper right), and the same for a flavor symmetric interaction (lower plots). The upper left plot corresponds to the model used for a fit to the inclusive jet cross section of $\Lambda = 1.6$ TeV.

Chapter 7

Conclusions

Dijet events, produced in proton-antiproton collisions, provide an excellent environment to test the Standard Model and to search for new particles.

In this analysis, we have used about 106 pb^{-1} data from CDF run 1A and run 1B to study the dijet invariant mass spectrum extending from 180 to 1035 GeV/c^2. The mass distribution is significantly above a QCD and CDF detector simulation at high mass. The fit of a smooth four-parameter curve to the distribution indicates that 90% of experiments should yield a lower χ^2 if the only variances were due to statistical errors.

We have determined the 95% confidence level limits for new particles decaying to dijets by fitting the data to this smooth parameterization of the background plus a dijet mass peak. This search excludes at 95% confidence level a model of axigluons for $200 < M_A < 980$ GeV/c^2, a model of excited quarks for $210 < M^* < 520$ GeV/c^2 and $600 < M^* < 760$ GeV/c^2, a model of technirhos for $260 < M_{\rho_T} < 470$ GeV/c^2, a model of new gauge boson W′ for $300 < M_{W'} < 420$ GeV/c^2, and a model of E_6 diquarks for $290 < M_{E6} < 420$ GeV/c^2.

Using a method which is fully corrected for systematic errors, we have also made a measurement of the dijet angular distribution using the same data sample. The data is in good agreement with NLO QCD within our statistical and systematic uncertainties. We have compared the data to various models

that include the left-handed contact interaction associated with a composite quark model, and for a model in which all quarks are composite the excluded regions are $\Lambda^+ \leq 1.80$ TeV and $\Lambda^- \leq 1.60$ TeV. When tested against the model where only u and d quarks are composite, we exclude the hypothesis that the excess in the observed inclusive jet Et spectrum can be attributed to a contact interaction with $\Lambda^+_{ud} \leq 1.6$ TeV.

Appendix A

The CDF Author List

F. Abe,[14] H. Akimoto,[32] A. Akopian,[27] M. G. Albrow,[7] S. R. Amendolia,[23] D. Amidei,[17] J. Antos,[29] C. Anway-Wiese,[4] S. Aota,[32] G. Apollinari,[27] T. Asakawa,[32] W. Ashmanskas,[15] M. Atac,[7] P. Auchincloss,[26] F. Azfar,[22] P. Azzi-Bacchetta,[21] N. Bacchetta,[21] W. Badgett,[17] S. Bagdasarov,[27] M. W. Bailey,[19] J. Bao,[35] P. de Barbaro,[26] A. Barbaro-Galtieri,[15] V. E. Barnes,[25] B. A. Barnett,[13] G. Bauer,[16] T. Baumann,[9] F. Bedeschi,[23] S. Behrends,[3] S. Belforte,[23] G. Bellettini,[23] J. Bellinger,[34] D. Benjamin,[31] J. Benlloch,[16] J. Bensinger,[3] D. Benton,[22] A. Beretvas,[7] J. P. Berge,[7] S. Bertolucci,[8] A. Bhatti,[27] K. Biery,[12] M. Binkley,[7] D. Bisello,[21] R. E. Blair,[1] C. Blocker,[3] A. Bodek,[26] W. Bokhari,[16] V. Bolognesi,[7] D. Bortoletto,[25] J. Boudreau,[24] L. Breccia,[2] C. Bromberg,[18] E. Buckley-Geer,[7] H. S. Budd,[26] K. Burkett,[17] G. Busetto,[21] A. Byon-Wagner,[7] K. L. Byrum,[1] J. Cammerata,[13] C. Campagnari,[7] M. Campbell,[17] A. Caner,[7] W. Carithers,[15] D. Carlsmith,[34] A. Castro,[21] D. Cauz,[23] Y. Cen,[26] F. Cervelli,[23] H. Y. Chao,[29] J. Chapman,[17] M.-T. Cheng,[29] G. Chiarelli,[23] T. Chikamatsu,[32] C. N. Chiou,[29] L. Christofek,[11] S. Cihangir,[7] A. G. Clark,[23] M. Cobal,[23] M. Contreras,[5] J. Conway,[28] J. Cooper,[7] M. Cordelli,[8] C. Couyoumtzelis,[23] D. Crane,[1] D. Cronin-Hennessy,[6] R. Culbertson,[5] J. D. Cunningham,[3] T. Daniels,[16] F. DeJongh,[7] S. Delchamps,[7] S. Dell'Agnello,[23] M. Dell'Orso,[23] L. Demortier,[27] B. Denby,[23] M. Deninno,[2] P. F. Derwent,[17] T. Devlin,[28] M. Dickson,[26] J. R. Dittmann,[6]

S. Donati,[23] J. Done,[30] A. Dunn,[17] N. Eddy,[17] K. Einsweiler,[15] J. E. Elias,[7] R. Ely,[15] E. Engels, Jr.,[24] D. Errede,[11] S. Errede,[11] Q. Fan,[26] I. Fiori,[2] B. Flaugher,[7] G. W. Foster,[7] M. Franklin,[9] M. Frautschi,[31] J. Freeman,[7] J. Friedman,[16] H. Frisch,[5] T. A. Fuess,[1] Y. Fukui,[14] S. Funaki,[32] G. Gagliardi,[23] S. Galeotti,[23] M. Gallinaro,[21] M. Garcia-Sciveres,[15] A. F. Garfinkel,[25] C. Gay,[9] S. Geer,[7] D. W. Gerdes,[17] P. Giannetti,[23] N. Giokaris,[27] P. Giromini,[8] L. Gladney,[22] D. Glenzinski,[13] M. Gold,[19] J. Gonzalez,[22] A. Gordon,[9] A. T. Goshaw,[6] K. Goulianos,[27] H. Grassmann,[23] L. Groer,[28] C. Grosso-Pilcher,[5] G. Guillian,[17] R. S. Guo,[29] C. Haber,[15] E. Hafen,[16] S. R. Hahn,[7] R. Hamilton,[9] R. Handler,[34] R. M. Hans,[35] K. Hara,[32] A. D. Hardman,[25] B. Harral,[22] R. M. Harris,[7] S. A. Hauger,[6] J. Hauser,[4] C. Hawk,[28] E. Hayashi,[32] J. Heinrich,[22] K. D. Hoffman,[25] M. Hohlmann,[1,5] C. Holck,[22] R. Hollebeek,[22] L. Holloway,[11] A. Hölscher,[12] S. Hong,[17] G. Houk,[22] P. Hu,[24] B. T. Huffman,[24] R. Hughes,[26] J. Huston,[18] J. Huth,[9] J. Hylen,[7] H. Ikeda,[32] M. Incagli,[23] J. Incandela,[7] G. Introzzi,[23] J. Iwai,[32] Y. Iwata,[10] H. Jensen,[7] U. Joshi,[7] R. W. Kadel,[15] E. Kajfasz,[7a] T. Kamon,[30] T. Kaneko,[32] K. Karr,[33] H. Kasha,[35] Y. Kato,[20] L. Keeble,[8] K. Kelley,[16] R. D. Kennedy,[28] R. Kephart,[7] P. Kesten,[15] D. Kestenbaum,[9] R. M. Keup,[11] H. Keutelian,[7] F. Keyvan,[4] B. Kharadia,[11] B. J. Kim,[26] D. H. Kim,[7a] H. S. Kim,[12] S. B. Kim,[17] S. H. Kim,[32] Y. K. Kim,[15] L. Kirsch,[3] P. Koehn,[26] K. Kondo,[32] J. Konigsberg,[9] S. Kopp,[5] K. Kordas,[12] W. Koska,[7] E. Kovacs,[7a] W. Kowald,[6] M. Krasberg,[17] J. Kroll,[7] M. Kruse,[25] T. Kuwabara,[32] S. E. Kuhlmann,[1] E. Kuns,[28] A. T. Laasanen,[25] N. Labanca,[23] S. Lammel,[7] J. I. Lamoureux,[3] T. LeCompte,[11] S. Leone,[23] J. D. Lewis,[7] P. Limon,[7] M. Lindgren,[4] T. M. Liss,[11] N. Lockyer,[22] O. Long,[22] C. Loomis,[28] M. Loreti,[21] J. Lu,[30] D. Lucchesi,[23] P. Lukens,[7] S. Lusin,[34] J. Lys,[15] K. Maeshima,[7] A. Maghakian,[27] P. Maksimovic,[16]

M. Mangano,[23] J. Mansour,[18] M. Mariotti,[21] J. P. Marriner,[7] A. Martin,[11] J. A. J. Matthews,[19] R. Mattingly,[16] P. McIntyre,[30] P. Melese,[27] A. Menzione,[23] E. Meschi,[23] S. Metzler,[22] C. Miao,[17] G. Michail,[9] R. Miller,[18] H. Minato,[32] S. Miscetti,[8] M. Mishina,[14] H. Mitsushio,[32] T. Miyamoto,[32] S. Miyashita,[32] Y. Morita,[14] J. Mueller,[24] A. Mukherjee,[7] T. Muller,[4] P. Murat,[23] H. Nakada,[32] I. Nakano,[32] C. Nelson,[7] D. Neuberger,[4] C. Newman-Holmes,[7] M. Ninomiya,[32] L. Nodulman,[1] S. H. Oh,[6] K. E. Ohl,[35] T. Ohmoto,[10] T. Ohsugi,[10] R. Oishi,[32] M. Okabe,[32] T. Okusawa,[20] R. Oliver,[22] J. Olsen,[34] C. Pagliarone,[2] R. Paoletti,[23] V. Papadimitriou,[31] S. P. Pappas,[35] S. Park,[7] A. Parri,[8] J. Patrick,[7] G. Pauletta,[23] M. Paulini,[15] A. Perazzo,[23] L. Pescara,[21] M. D. Peters,[15] T. J. Phillips,[6] G. Piacentino,[2] M. Pillai,[26] K. T. Pitts,[7] R. Plunkett,[7] L. Pondrom,[34] J. Proudfoot,[1] F. Ptohos,[9] G. Punzi,[23] K. Ragan,[12] A. Ribon,[21] F. Rimondi,[2] L. Ristori,[23] W. J. Robertson,[6] T. Rodrigo,[7a] J. Romano,[5] L. Rosenson,[16] R. Roser,[11] W. K. Sakumoto,[26] D. Saltzberg,[5] A. Sansoni,[8] L. Santi,[23] H. Sato,[32] V. Scarpine,[30] P. Schlabach,[9] E. E. Schmidt,[7] M. P. Schmidt,[35] A. Scribano,[23] S. Segler,[7] S. Seidel,[19] Y. Seiya,[32] G. Sganos,[12] A. Sgolacchia,[2] M. D. Shapiro,[15] N. M. Shaw,[25] Q. Shen,[25] P. F. Shepard,[24] M. Shimojima,[32] M. Shochet,[5] J. Siegrist,[15] A. Sill,[31] P. Sinervo,[12] P. Singh,[24] J. Skarha,[13] K. Sliwa,[33] F. D. Snider,[13] T. Song,[17] J. Spalding,[7] P. Sphicas,[16] F. Spinella,[23] M. Spiropulu,[9] L. Spiegel,[7] L. Stanco,[21] J. Steele,[34] A. Stefanini,[23] K. Strahl,[12] J. Strait,[7] R. Ströhmer,[9] D. Stuart,[7] G. Sullivan,[5] A. Soumarokov,[29] K. Sumorok,[16] J. Suzuki,[32] T. Takada,[32] T. Takahashi,[20] T. Takano,[32] K. Takikawa,[32] N. Tamura,[10] F. Tartarelli,[23] W. Taylor,[12] P. K. Teng,[29] Y. Teramoto,[20] S. Tether,[16] D. Theriot,[7] T. L. Thomas,[19] R. Thun,[17] M. Timko,[33] P. Tipton,[26] A. Titov,[27] S. Tkaczyk,[7] D. Toback,[5] K. Tollefson,[26] A. Tollestrup,[7] J. Tonnison,[25]

J. F. de Troconiz,[9] S. Truitt,[17] J. Tseng,[13] N. Turini,[23] T. Uchida,[32] N. Uemura,[32] F. Ukegawa,[22] G. Unal,[22] S. C. van den Brink,[24] S. Vejcik, III,[17] G. Velev,[23] R. Vidal,[7] M. Vondracek,[11] D. Vucinic,[16] R. G. Wagner,[1] R. L. Wagner,[7] J. Wahl,[5] C. Wang,[6] C. H. Wang,[29] G. Wang,[23] J. Wang,[5] M. J. Wang,[29] Q. F. Wang,[27] A. Warburton,[12] G. Watts,[26] T. Watts,[28] R. Webb,[30] C. Wei,[6] C. Wendt,[34] H. Wenzel,[15] W. C. Wester, III,[7] A. B. Wicklund,[1] E. Wicklund,[7] R. Wilkinson,[22] H. H. Williams,[22] P. Wilson,[5] B. L. Winer,[26] D. Wolinski,[17] J. Wolinski,[30] X. Wu,[23] J. Wyss,[21] A. Yagil,[7] W. Yao,[15] K. Yasuoka,[32] Y. Ye,[12] G. P. Yeh,[7] P. Yeh,[29] M. Yin,[6] J. Yoh,[7] C. Yosef,[18] T. Yoshida,[20] D. Yovanovitch,[7] I. Yu,[35] J. C. Yun,[7] A. Zanetti,[23] F. Zetti,[23] L. Zhang,[34] W. Zhang,[22] and S. Zucchelli[2]

(CDF Collaboration)

[1] *Argonne National Laboratory, Argonne, Illinois 60439*

[2] *Istituto Nazionale di Fisica Nucleare, University of Bologna, I-40126 Bologna, Italy*

[3] *Brandeis University, Waltham, Massachusetts 02254*

[4] *University of California at Los Angeles, Los Angeles, California 90024*

[5] *University of Chicago, Chicago, Illinois 60637*

[6] *Duke University, Durham, North Carolina 27708*

[7] *Fermi National Accelerator Laboratory, Batavia, Illinois 60510*

[8] *Laboratori Nazionali di Frascati, Istituto Nazionale di Fisica Nucleare, I-00044 Frascati, Italy*

[9] *Harvard University, Cambridge, Massachusetts 02138*

[10] *Hiroshima University, Higashi-Hiroshima 724, Japan*

[11] *University of Illinois, Urbana, Illinois 61801*

[12] *Institute of Particle Physics, McGill University, Montreal H3A 2T8, and University of Toronto,*

Toronto M5S 1A7, Canada

[13] *The Johns Hopkins University, Baltimore, Maryland 21218*

[14] *National Laboratory for High Energy Physics (KEK), Tsukuba, Ibaraki 305, Japan*

[15] *Lawrence Berkeley Laboratory, Berkeley, California 94720*

[16] *Massachusetts Institute of Technology, Cambridge, Massachusetts 02139*

[17] *University of Michigan, Ann Arbor, Michigan 48109*

[18] *Michigan State University, East Lansing, Michigan 48824*

[19] *University of New Mexico, Albuquerque, New Mexico 87131*

[20] *Osaka City University, Osaka 588, Japan*

[21] *Universita di Padova, Istituto Nazionale di Fisica Nucleare, Sezione di Padova, I-35131 Padova, Italy*

[22] *University of Pennsylvania, Philadelphia, Pennsylvania 19104*

[23] *Istituto Nazionale di Fisica Nucleare, University and Scuola Normale Superiore of Pisa, I-56100 Pisa, Italy*

[24] *University of Pittsburgh, Pittsburgh, Pennsylvania 15260*

[25] *Purdue University, West Lafayette, Indiana 47907*

[26] *University of Rochester, Rochester, New York 14627*

[27] *Rockefeller University, New York, New York 10021*

[28] *Rutgers University, Piscataway, New Jersey 08854*

[29] *Academia Sinica, Taipei, Taiwan 11529, Republic of China*

[30] *Texas A&M University, College Station, Texas 77843*

[31] *Texas Tech University, Lubbock, Texas 79409*

[32] *University of Tsukuba, Tsukuba, Ibaraki 305, Japan*

[33] *Tufts University, Medford, Massachusetts 02155*

[34] *University of Wisconsin, Madison, Wisconsin 53706*

[35] *Yale University, New Haven, Connecticut 06511*

Bibliography

[1] S.L. Glashow, *Nucl. Phys.* **22**, 579 (1961); S. Weinberg, *Phys. Rev. Lett.* **19**, 1264 (1967).

[2] E. Eichten et al., *Rev. Mod. Phys.* **56**, 579 (1984).

[3] J.F. Owens, E. Reya, and M. Gluck, *Phys. Rev.* **D18**, 1501(1978)

[4] G. Altarelli and G. Parisi, *Nucl. Phys.* **B126**, 298 (1977)

[5] R.D. Field and R.P. Feynman, *Nucl. Phys.* **B136**, 1 (1978).

[6] B. Andersson et al., *Phys. Rep.* **97**, 31 (1983).

[7] J. Botts et al., *Phys. Lett.* **B 304**, 159 (1993).

[8] P. Frampton and S. Glashow, *Phys. Lett.* **B 190**, 157 (1987).

[9] J. Bagger, C. Schmidt and S. King, *Phys. Rev.* **D 37**, 1188 (1988).

[10] G. Katsilieris, O. Korakiantitis and S. Vlassopulos, Glashow, *Phys. Lett.* **B 288**, 221 (1992).

[11] U. Baur, I. Hinchliffe and D. Zeppenfeld, *International Journal of Modern Physics* **A 2**, 1285 (1987); U. Baur, M. Spira and P. M. Zerwas, *Phys. Rev.* **D42**, 815 (1990).

[12] J. Bardeen, L.N. Cooper, and J.R. Schrieffer, *Phys. Rev.* **106**, 162 (1957); **108**, 1175 (1957).

[13] Kenneth Lane and M. V. Ramana, *Phys. Rev.* **D 44**, 2678 (1991).

[14] Estia Eichten and Kenneth Lane, *Phys. Lett.* **B 327**, 129 (1994).

[15] G. Altarelli, B. Mele and M.Ruiz-Altaba, *Z. Phys.* **C45**, 109 (1989).

[16] D. Cocolicchio et al., *Phys. Lett.* **B 255**, 599 (1991).

[17] Collider Physics, Barger and Phillips, page 248.

[18] J. Hewett and T.G. Rizzo, *Phys. Rep.* **183**, 193 (1989); V. Angelopoulos et al., *Nucl. Phys.* **B 292**, 59 (1987).

[19] T.G. Rizzo, *Phys. Rev.* **D 48**, 4470 (1993).

[20] F. Abe et al., *Nucl. Instr. Meth.* **A 271**, 387 (1988).

[21] D. Amidei et al., *Nucl. Instr. Meth.* **A 350**, 73 (1994).

[22] F. Snider et al., *Nucl. Instr. Meth.* **A 268**, 75 (1988).

[23] F. Bedeschi and et al., *Nucl. Instr. Meth.* **A268**, 50 (1988).

[24] L. Balka et al., *Nucl. Instr. Meth.* **A 267**, 272 (1988).

[25] S. Bertolucci et al., *Nucl. Instr. Meth.* **A 267**, 301 (1988).

[26] Y. Fukui et al., *Nucl. Instr. Meth.* **A267**, 280 (1988).

[27] M.E.B. Franklin et al., in the proceedings of the 7th Topical Workshop on Proton-Antiproton Collider Physics, p. 420, edited by R. Raja, A. Tollestrup and J. Yoh, World Scientific, Singapore (1988).

[28] G. Brandenburg et al., *Nucl. Instr. Meth.* **A267**, 257 (1988).

[29] S. Cihangir et al., *Nucl. Instr. Meth.* **A 267**, 249 (1988).

[30] D.Amidei et al., *Nucl. Instr. Meth.* **A269**, 51 (1988).

[31] P. Bagnaia et al., *Phys. Lett.* **B 144**, 283 (1984).

[32] G. Foster et al., *Nucl. Instr. Meth.* **A267**, 280 (1988).

[33] F.Abe et al., *Phys. Rev.* **D 45**, 1448 (1992).

[34] F.Abe et al., *Phys. Rev. Lett.* **68**, 1104 (1992).

[35] R.Field and R.Feynman, *Nucl. Phys.* **B136**, 1 (1978).

[36] Paul Derwent and Brenna Flaugher. Comparison of Dielectron Mass, Run 0, Run 1A, and Run 1B. CDF Internal Note 2880 (1994).

[37] S. Kopp, Good Run List for 1992-1993 CDF Run, CDF Internal Note (1992).

[38] N. Eddy, New Relative Jet Corrections for Run 1A and Run 1B Data, CDF Internal Note 3534 (1996).

[39] Chao Wei and Robert M. Harris, Dijet Angular Distribution from Run 1A + 1B, CDF Internal Note 3637 (1996).

[40] Robert M. Harris et al., Search for New Particles Decaying to Dijet, CDF Internal Note 2636 (1994).

[41] PYTHIA *V*5.6 by T. Sjostrand, CERN-TH-6488/92 (1992).

[42] J. Botts et al., *Phys. Lett.* **B304**, 159 (1993).

[43] B. Andersson, G. Gustafson, G. Ingelman and T. Sjostrand, *Phys. Rep.* **97**, 31 (1983).

[44] M. Shapiro et al., A user's guide to QFL. CDF Internal Note 1810 (1992).

[45] A. Bhatti, Inclusive Jet Cross Section from 1993-93 Data Set, CDF Internal Note 2457.

[46] Robert M. Harris et al., Search for New Particles Decaying to Dijet, CDF Internal Note 2636 (1994).

[47] F. Abe et al., *Phys. Rev. Lett.* **74**, 3538 (1995).

[48] F. Abe et al., *Phys. Rev. Lett.* **72**, 3004 (1994).

[49] Robert M. Harris, Search for Excited Quarks in Photon + Jet Events, CDF Internal Note 1960 (1993); Bob Drucker, Search for Excited Quarks in W + Jet Events, CDF Internal Note 2087 (1993); Bob Drucker and

Robert M. Harris, Limits on Excited Quarks from W + Jet and γ + Jet events, CDF Internal Note 2120 (1993).

[50] F. Abe et al., Comparison of Jet Production in $\bar{p}p$ Collisions at $\sqrt{s} = 546$ and 1800 GeV, *Phys. Rev. Lett.* **70**, 1376 (1993).

[51] Brenna Flaugher et al., Calibration Stability and the Jet Energy Scale: Run 0 and Run 1A Comparison, CDF Internal Note 2902.

[52] Chao Wei and Robert M. Harris, Search for New Particles Decaying to Dijet, CDF Internal Note 3081 (1995).

[53] S. Behrends, Xt Scaling (Updated): Comparison of Jet Production at $\sqrt{s} = 546$ GeV and 1800 GeV, CDF Internal Note 1650 (1992).

[54] James Tonnison, A Pre-release of Jet Corrections For 6.1 Data, CDF Internal Note 2189 (1993); QDJSCO Corrections For 6.01 Data, CDF Internal Note 2053 (1993); Louis Keeble, New Jet Correction Function QDJSCO Version 2.0, CDF Internal Note 1513 (1991).

[55] Robert M. Harris et al., Search for New Particles Decaying to Dijet, CDF Internal Note 2636 (1994).

[56] D. Decamp et al. Search for new particles in Z decays using the Aleph detector, *Phys. Rep.* **216**, 253 (1992).

[57] J. Alitti et al., A Search for New Intermediate Vector Bosons and Excited Quarks Decaying to Two-Jets at the CERN $\bar{p}p$ Collider, CERN-PPE/93-66 (1993).

[58] F. Abe et al., *Phys. Rev. Lett.* **74**, 2900 (1995).

[59] B.L. Combridge et al., *Nucl. Phys.* **B 239**, 429 (1984).

[60] Brenna Flaugher and Jim Mueller, CDF Internal Note 1520.

[61] Marjorie Shapiro and Dave Brown, Papgen: An Analysis Control Interface for Papageno, CDF Internal Note 1221.

[62] Bob Drucker, QDJTMC: A Very Fast Detector Simulation for Partons, CDF Internal Note 2523.

[63] P. Bagnaia et al., *Phys. Lett.* **B 144**, 283 (1984).

[64] Jim Mueller, Brenna Flaugher and Carol Hawk, Acceptance Corrections and Associated Systematic Errors for the Dijet Angular Distribution Analysis, CDF Internal Note 1179.

[65] Ken Lane, Electroweak and Flavor Dynamics at Hadron Colliders, BUHEP-96-8 (1996).

[66] F. Abe, et al., *Phys. Rev. Lett.* **77**, 438 (1996).

Biography

Chao Wei was born November 28 1962 in Jinan, Shandong Province, China.

He began his undergraduate studies at Shandong University in 1980, and earned his Bachelor of Science in physics there in 1984. In the fall of 1984 he began his graduate school at the same university, and started his high energy physics studies on a cosmic-ray experiment. He was awarded the Master of Science degree in physics in 1987 from Shandong University. From 1989-1992 he worked in a fixed target experiment at Fermilab on an exchange program.

In the fall of 1992 he entered graduate school at Duke University. He worked as a research assistant in high energy physics group on a collider experiment at Fermilab. He completed his Doctor of Philosophy at Duke in 1996.